学位論文

Collider Phenomenology of Metastable Particles with Sub-Millimeter Displaced Vertices

（１ミリ以下の崩壊長をもつ準安定粒子に関する加速器現象論）

平成 29 年１２月博士（理学）申請

東京大学大学院理学系研究科

物理学専攻

伊藤　隼人

Ph.D thesis

Collider Phenomenology of Metastable Particles with Sub-Millimeter Displaced Vertices

Hayato Ito

Department of Physics, University of Tokyo, Tokyo 113-0033, Japan

Abstract

Among various candidates of new physics, supersymmetry (SUSY) has been considered to provide answers to problems which have not been explained in the standard model (SM). In this thesis we first review SUSY extension of the SM (SSM). However, besides null results of searches for supersymmetric particles at the LHC, it has been pointed out that the SSM with light sfermions has several phenomenological difficulties. After reviewing such difficulties, we see that the Minimal Supersymmetric SM (MSSM) with sfermions as heavy as $\sim 10^3$ TeV may evade such difficulties without elaborate model buildings. One of the characteristic features of the MSSM with heavy sfermions is that gluinos become metastable. We see that if the mass scale of squarks is about $\sim 10^3$ TeV, the decay length of the gluino (*i.e.*, the product of the mean lifetime $\tau_{\tilde{g}}$ and the speed of light c) can be $c\tau_{\tilde{g}} \sim \mathcal{O}(100)$ μm. Although our main concern in this thesis is metastable gluinos, particles with a sub-millimeter decay length also appear in many models of physics beyond the SM. After reviewing theoretical motivations for metastable gluinos, we review existing LHC searches for metastable particles. We see that longevity of metastable particles with sub-millimeter decay length has been often ignored in the LHC searches and they have been regarded as promptly-decaying particles. In this thesis, we show that, by requiring displaced vertices on top of the event selection criteria used in the ordinary search strategies for promptly-decaying particles, we can considerably extend the LHC reach for metastable particles with a decay length of $\gtrsim 100$ μm. We discuss a way of reconstructing sub-millimeter displaced vertices by exploiting the same technique used for the primary vertex reconstruction on the assumption that the metastable particles are always pair-produced and their decay products contain high-p_{T} jets. We show that, by applying a cut based on displaced vertices on top of standard kinematical cuts for the search of new particles, the LHC reach can be significantly extended if the decay length is $\gtrsim 100$ μm. In addition, we may measure the lifetime of the target particle through the reconstruction of displaced vertices, which plays an important role in understanding the new physics behind the metastable particles. We also study the prospects of searches for metastable particles at a future 100 TeV pp collider.

Contents

Chapter 1

Introduction

1.1 Overview

Almost a decade has passed since the LHC started to run. At the LHC, the Higgs boson [1–6], which is the long-awaited last piece of the Standard Model (SM) [7–10], has finally been discovered [11, 12]. Completing the missing piece of the SM, the LHC has embarked on searches for new physics beyond the SM. Nevertheless, after the discovery of the Higgs boson, array of reports of null results have come. Even though signals of new physics have not appeared yet, still, there is a need to quest for physics which extends the SM; no candidates for the Dark Matter (DM), no unified explanation of forces between elementary particles, an enormous hierarchy between the weak scale and the Planck scale, and so on.

Among various candidates of new physics, supersymmetric (SUSY) [13] extension of the SM (SSM) [14–16] has been considered to provide answers to these problems. Introduction of supersymmetric partners for every field content in the SM tames quadratic divergence appearing in the Higgs potential. Gauge coupling constants seem to be unified around $M_X \sim 10^{16}$ GeV and a natural candidate of the DM exists in the SSM.

However, besides null results of searches for supersymmetric particles, it has been pointed out that the SSM with light sfermions has several phenomenological difficulties. To realize the observed Higgs mass in the Minimal Supersymmetric SM (MSSM), large radiative corrections to the Higgs potential are needed. Sfermions need to be as heavy as 10 (10^4) TeV for $\tan\beta = 10$ (1) to provide such large radiative corrections, which causes tension with the naturalness argument. Another difficulty comes from various sources of flavour and CP violation intrinsically included in the SSM. These flavour and CP violation sources easily cause conflict with severe experimental constraints. To evade this difficulty without elaborate model buildings [17], sfermions seem to be required to be heavier than $\sim 10^3$ TeV. In addition, heavy sfermions suppress proton decay rate, hence revive the minimal $SU(5)$ SUSY grand unified theory.

Although all these situations imply sfermions with mass of $\gtrsim \mathcal{O}(10 - 10^3)$ TeV, it is still possible that gauginos, which are protected by chiral symmetry, remain around the weak scale. Therefore even if sfermions are too heavy to be probed at colliders directly,

gauginos might be accessible at the LHC or a future 100 TeV pp collider. One of the characteristic features of such scenarios, in which sfermions are as heavy as $\sim 10^3$ TeV and, on the other hand, gauginos are light enough to be produced at colliders, is that decays of gluinos are suppressed, hence gluinos might be metastable. Here the decay length of the gluino $c\tau_{\tilde{g}}$ (*i.e.*, the product of the mean lifetime $\tau_{\tilde{g}}$ and the speed of light c) is given by [18–20]

$$c\tau_{\tilde{g}} \simeq 200\ \mu\text{m} \times \left(\frac{m_{\tilde{q}}}{10^3\ \text{TeV}}\right)^4 \left(\frac{2\ \text{TeV}}{m_{\tilde{g}}}\right)^5 . \tag{1.1}$$

Eq. (1.1) shows that if the squark masses are as heavy as the PeV scale, which has a motivation as we already see, the decay length of the gluino may be as long as $c\tau_{\tilde{g}} \sim \mathcal{O}(100)\ \mu$m.

From the point of view of physics beyond the SM, there are a variety of well-motivated new particles with $c\tau \sim$ sub-millimeter besides the above case. Metastable SUSY particles are also found in the gauge-mediation models [21, 22], where the decay length of the next-to-lightest SUSY particle decaying into gravitino can be order sub-millimeter, as well as in R-parity violating SUSY models [23, 24]. In addition, theories of Neutral Naturalness [25, 26], hidden-valley models [27], composite Higgs models [28], dark matter models [29], and models with sterile neutrinos [30] predict metastable particles with an $\mathcal{O}(100)\ \mu$m decay length.

If metastable particles have a decay length of $\mathcal{O}(1)$ m or shorter, then their decay can occur within tracking detectors and thus it is in principle possible to directly observe their decay points, which are away from the production point. In fact, such attempts have been made in the LHC experiments. For example, the ATLAS collaboration has searched for displaced vertices (DVs) that originate from decay of long-lived particles by investigating charged tracks with a transverse impact parameter, d_0, of 2 mm $< |d_0| <$ 300 mm, requiring that the transverse distance between DVs and any of the primary vertices be longer than 4 mm [31, 32]. This search is therefore sensitive to metastable particles whose decay length is $c\tau \sim \mathcal{O}(1-1000)$ mm. The disappearing-track searches [33] can also probe a long-lived charged particle when it decays into a neutral particle which is degenerate with the charged particle in mass [34–37]; the target of these searches is $c\tau \gtrsim 10$ cm.

On the contrary, particles with a sub-millimeter decay length have been beyond the reach of these searches. Such rather short-lived particles have been often regarded as promptly-decaying particles and probed without relying on their longevity. Exceptionally, Ref. [38] considered R-parity violating supersymmetric (SUSY) model to which "ordinary" search strategies does not apply, and showed that DV-based cuts may be useful for the LHC study of such a model if the decay length of the lightest SUSY particle is longer than $\mathcal{O}(100)\ \mu$m.

Although LHC constraints on some of those metastable particles have been already stringent even with the analysis assuming that they decay promptly, inclusion of DV-based cuts upon it significantly extends the reach of those [39]. In this thesis, we study how far we

can extend the reach for new metastable particles with sub-millimeter displaced vertices by utilizing signatures coming from their longevity. We try to reconstruct displaced vertices with tracking information. We also study the prospect of lifetime measurement of metastable particles. Although we study searches for metastable gluinos in this thesis, the analysis can also be applied to searches for other new metastable particles if they are pair-produced and decay into coloured particles.

The results presented in this thesis are original in the following points;

- We, for the first time, apply DV based selection cuts in searches for metastable particles which have been treated as promptly decaying ones.
- We, for the first time, study the prospect of searches for metastable particles with sub-millimeter DVs at a future 100 TeV pp collider.

1.2 Outline

In Chapter 2 we review supersymmetric extension of the SM and its phenomenological difficulties. We also review properties of metastable gluinos. In Chapter 3 we review existing collider searches for massive metastable particles. In Chapter 4 we discuss how far we can extend the reach for metastable particles with DVs at the LHC. In Chapter 5 we discuss the prospect of searches for metastable particles at a future 100 TeV pp collider. In Chapter 6 the summary of the conclusions and discussions are presented.

Chapter 2

Supersymmetry

2.1 MSSM

The Standard Model (SM) of elementary particle physics has triumphed over past decades and it has succeeded to describe experimental results. In spite of great success of the SM, there are still many reasons driving physicists to quest for a new theory which encompasses the SM. Among these reasons are no candidates for Dark Matter, no unified explanation of forces between elementary particles, an enormous hierarchy between the weak scale and the Planck scale, and so on. Here we take a look on the so-called hierarchy problem [40–44] due to the enormous difference between the weak scale and the Planck scale and a solution to this problem.

In the SM, the Higgs field has a unique property that it is a spinless scalar field. Since there is no symmetry that preserves the smallness of the Higgs mass against the radiative correction, on the contrary to the fermionic fields and gauge fields, the Higgs field is very sensitive to the unknown physics of high mass scale. This can be seen by considering radiative corrections to the quadratic term of the Higgs field in the SM Lagrangian. A fermionic field (f) which has a Yukawa interaction of the form $-\lambda_f H f \bar{f}$ with the Higgs field (H) induces a radiative correction to the quadratic term of the Higgs field of

$$\Delta m_H^2 = -\frac{|\lambda_f|^2}{8\pi^2}\Lambda_{UV}^2 + \dots, \tag{2.1}$$

with Λ_{UV} being the cut off scale where new physics appears. Without elaborate fine tuning of the coefficients of the quadratic term of the Higgs field (m_H^2) at the scale Λ_{UV}, it is natural to expect that this coefficient evaluated at the weak scale is the same order as the cut off scale of Λ_{UV}. However we already know from experiments that m_H^2 should be of the order of 100 GeV in the SM. Therefore if Λ_{UV} is much larger than the weak scale, there exists an enormous fine tuning at the scale of Λ_{UV}.

We can find one of the solutions to this hierarchy problem by studying radiative corrections induced by a scalar field (ϕ) that couples to the Higgs field as $\lambda_\phi |H|^2|\phi|^2$. In this case the radiative correction to the quadratic term of the Higgs field can be written

as

$$\Delta m_H^2 = +\frac{|\lambda_\phi|^2}{16\pi^2}\Lambda_{UV}^2 + \dots . \tag{2.2}$$

Note that if there are exactly two scalar fields which has the same size of coupling ($|\lambda_f| = |\lambda_\phi|$) as that of each fermionic field, then the contributions proportional to Λ_{UV}^2 from these fermionic and scalar fields are cancelled and the dependence on the cut off scale is mitigated to $\ln(\Lambda_{UV})$. That is if there is a symmetry which gives a connection between fermionic and scalar fields in a theory, quadratic terms of scalar fields can be stable against radiative corrections.

An extended SM which is invariant under a transformation generated by supersymmetry generators $Q_a\,(a = \pm 1/2)$ is called the Supersymmetric SM (SSM). Here the supersymmetry generators are fermionic and realized in spin 1/2 representation and satisfy the anticommutation relations

$$\{Q_a, Q_b^*\} = 2\sigma_{ab}^\mu P_\mu \,, \tag{2.3}$$
$$\{Q_a, Q_b\} = 0 \,, \tag{2.4}$$

with P_μ being a momentum operator and

$$\sigma_1 = \begin{pmatrix} 0 & 1 \\ 1 & 0 \end{pmatrix} \,,\ \sigma_2 = \begin{pmatrix} 0 & -i \\ i & 0 \end{pmatrix} \,,\ \sigma_3 = \begin{pmatrix} 1 & 0 \\ 0 & -1 \end{pmatrix} \,,\ \sigma_0 = \begin{pmatrix} 1 & 0 \\ 0 & 1 \end{pmatrix} \,. \tag{2.5}$$

Since the supersymmetry generators Q_a are fermionic and carry spin 1/2, a bosonic state can be converted to a fermionic one by operating Q_a and vice versa, which is represented mnemonically as

$$Q\,|\text{Boson}\rangle = |\text{Fermion}\rangle \,, \tag{2.6}$$
$$Q\,|\text{Fermion}\rangle = |\text{Boson}\rangle \,. \tag{2.7}$$

Since supersymmetry connects fermionic and bosonic fields, quadratic terms of scalar fields are stable against radiative corrections in the SSM. Therefore extending the SM to a supersymmetric one can be a solution to the hierarchy problem.

The minimal supersymmetric extension of the SM is called the Minimal Supersymmetric Standard Model (MSSM). In the MSSM, all fermionic and gauge field components of the SM are extended to corresponding super fields. In contrast to the SM, at least two Higgs doublets are required in the SSM. There are two reasons for this. First if there were only one Higgs doublet superfields, their component of chiral fermion fields would spoil anomaly cancelation realized in the SM. This problem can be avoided if there are two Higgs doublet super fields whose $U(1)$ charges are opposite in sign. Second reason is that with only one Higgs doublet, we cannot give mass to both up-type quarks and down-type quarks (charged leptons) simultaneously by constructing yukawa interaction terms. Higgs doublet superfields and its complex conjugate cannot be included in the superpotential

at the same time since it should be holomorphic in the chiral superfields. From these reasons, we need at least two Higgs doublet superfields in the SSM. In the MSSM, two Higgs doublet super fields are contained. In Table 2.1, we present all superfields introduced in the MSSM, their component fields, and gauge quantum numbers. The SUSY invariant part of the MSSM Lagrangian is given by

$$\begin{aligned}
\mathcal{L}_{\rm kin} =& -\sum_n (D_\mu\phi)^*_n (D^\mu\phi)_n - \frac{1}{2}\sum_n \left(\overline{\psi_{nL}}\gamma^\mu (D_\mu\psi_L)_n\right) + (\text{h.c.}) \\
& - \frac{1}{2}\sum_{nm}\frac{\partial^2 f(\phi)}{\partial\phi_n\partial\phi_m}(\psi^{\rm T}_{nL}\epsilon\psi_{mL}) + (\text{h.c.}) - \sum_n \left|\frac{\partial f(\phi)}{\partial\phi_n}\right|^2 \\
& + i\sqrt{2}\sum_{Anm}\left(\overline{\psi_{nL}}(t_A)_{nm}\lambda_A\right)\phi_m + (\text{h.c.}) - \frac{1}{2}\sum_A\left(\sum_{nm}\phi^*_n(t_A)_{nm}\phi_m\right)^2 \\
& - \frac{1}{4}\sum_A f_{A\mu\nu}f^{\mu\nu}_A - \frac{1}{2}\sum_A\left(\overline{\lambda_A}(\not{D}\lambda)_A\right) ,
\end{aligned} \tag{2.8}$$

where the superpotential $f(\phi)$ is given by

$$\begin{aligned}
f(\phi) =& \sum_{i,j} h^D_{ij}\left[\left(D_i H^0_1 - U_i H^-_1\right)\bar{D}_j\right] + \sum_{i,j} h^E_{ij}\left[\left(E_i H^0_1 - N_i H^-_1\right)\bar{E}_j\right] \\
& + \sum_{i,j} h^U_{ij}\left[\left(D_i H^+_2 - U_i H^0_2\right)\bar{U}_j\right] + \mu\left[H^+_2 H^-_1 - H^0_2 H^0_1\right] .
\end{aligned} \tag{2.9}$$

One drawback of the MSSM compared to the SM is that there is no principle that forbids the renormalizable interactions violating lepton or baryon number (L, B) in the Lagrangian. Without violating $SU(3)\times SU(2)\times U(1)$ gauge symmetries, we can add to the superpotential Eq. (2.9) terms such as,

$$(D_i N_j - U_i E_j)\,\bar{D}_k \ , \tag{2.10}$$
$$(E_i N_j - N_i E_j)\,\bar{E}_k \ , \tag{2.11}$$
$$\bar{D}_i\bar{D}_j\bar{U}_k \ . \tag{2.12}$$

For example, $\tilde{d}_R$ exchange between Eq. (2.10) and Eq. (2.12) gives rise to the process of proton decay $p\to\pi^0+e^+$, whose rate is highly constrained by Super-Kamiokande experiment, $1/\Gamma(p\to\pi^0+e^+) > 1.6\times10^{34}$ years [45]. To forbid these L and B violating interactions, it is usually assumed that "matter-parity" [46–49] is conserved in the MSSM Lagrangian. Here the matter-parity is defined as,

$$P_M = (-1)^{3(B-L)} , \tag{2.13}$$

where all component fields in a supermultiplet are assigned the same value of B and L. It can be seen that conservation of the matter-parity forbids all of the L and B breaking interaction in Eqs. (2.10)–(2.12) while terms in the superpotential Eq. (2.9) are

superfields	spin–0	spin–$\frac{1}{2}$	spin–1	$SU(3)$	$SU(2)$	Y	B
$Q_i = \begin{pmatrix} U_i \\ D_i \end{pmatrix}$	$\tilde{Q}_i = \begin{pmatrix} \tilde{u}_{L,i} \\ \tilde{d}_{L,i} \end{pmatrix}$	$Q_i = \begin{pmatrix} u_i \\ d_i \end{pmatrix}_L$		$\mathbf{3}$	$\mathbf{2}$	$\frac{1}{6}$	$\frac{1}{3}$
$\bar{U}_i$	$\tilde{u}^*_{R,i}$	$(u^c_i)_L$		$\mathbf{3}^*$	$\mathbf{1}$	$-\frac{2}{3}$	$-\frac{1}{3}$
$\bar{D}_i$	$\tilde{d}^*_{R,i}$	$(d^c_i)_L$		$\mathbf{3}^*$	$\mathbf{1}$	$\frac{1}{3}$	$-\frac{1}{3}$
$L_i = \begin{pmatrix} N_i \\ E_i \end{pmatrix}$	$\tilde{L}_i = \begin{pmatrix} \tilde{\nu}_i \\ \tilde{e}_{L,i} \end{pmatrix}$	$L_i = \begin{pmatrix} \nu_i \\ e_i \end{pmatrix}_L$		$\mathbf{1}$	$\mathbf{2}$	$-\frac{1}{2}$	0
$\bar{E}_i$	$\tilde{e}^*_{R,i}$	$(e^c_i)_L$		$\mathbf{1}$	$\mathbf{1}$	1	0
		$\tilde{g}$	g	$\mathbf{8}$	$\mathbf{1}$	0	0
		$\tilde{W}^{\pm,0}$	$W^{\pm,0}$	$\mathbf{1}$	$\mathbf{3}$	0	0
		$\tilde{B}$	B	$\mathbf{1}$	$\mathbf{1}$	0	0
$H_1 = \begin{pmatrix} H^0_1 \\ H^-_1 \end{pmatrix}$	$H_1 = \begin{pmatrix} H^0_1 \\ H^-_1 \end{pmatrix}$	$\tilde{H}_1 = \begin{pmatrix} \tilde{H}^0_1 \\ \tilde{H}^-_1 \end{pmatrix}$		$\mathbf{1}$	$\mathbf{2}$	$-\frac{1}{2}$	0
$H_2 = \begin{pmatrix} H^+_2 \\ H^0_2 \end{pmatrix}$	$H_2 = \begin{pmatrix} H^+_2 \\ H^0_2 \end{pmatrix}$	$\tilde{H}_2 = \begin{pmatrix} \tilde{H}^+_2 \\ \tilde{H}^0_2 \end{pmatrix}$		$\mathbf{1}$	$\mathbf{2}$	$\frac{1}{2}$	0

Table 2.1: The component fields of the superfields in the MSSM and their gauge quantum numbers.

all invariant under the matter-parity. If the matter-parity is conserved, the conservation of R-parity [16],

$$P_R = (-1)^{3(B-L)+2s}\,, \tag{2.14}$$

with s being the spin of the component field, is also guaranteed automatically. With this definition, all particles contained in the SM are assigned $P_R = +1$ and all supersymmetric particles are assigned a negative parity $P_R = -1$. Therefore in the R-parity conserving MSSM, the number of created supersymmetric particles are always even and the lightest supersymmetric particle (LSP) is stable.

The MSSM has been receiving much attention due to several appealing points besides the cancellation of radiative corrections to the Higgs quadratic terms. First we mention the dark matter (DM) candidate particles contained in the MSSM. It is now widely believed that the cold dark matter exists in the universe with the density of $\Omega_{\rm DM}h^2 \approx 0.119$ [50, 51]. As already mentioned, the LSP in models with R-parity conservation is stable and therefore is thought to be a well-motivated DM candidate in many such models. There are

strong constraints on electrically charged and colored stable particles, since such particles would be bound to normal matter and form anomalously heavy isotopes [52]. Therefore among supersymmetric particles, electrically neutral and non-colored stable ones can be a DM candidate. In the R-parity conserving MSSM, neutralino and gravitino as the LSP satisfy the above-mentioned condition, hence can be a DM candidate. [#1]

If the LSP is neutralino and stable, its thermal relic can contribute to today's DM density. It is well known that if the dark matter is a thermal relic of a stable neutral particle χ, its today's abundance Ω_χ is approximately given by [57, 58],

$$\Omega_\chi \sim \frac{10^{-10}\,\mathrm{GeV}^{-2}}{\langle \sigma_A v \rangle}, \tag{2.15}$$

with $\langle \sigma_A v \rangle$ being the thermally averaged annihilation cross section of χ's. For weakly interacting massive particles (WIMP) with mass of about the weak scale, thermally averaged annihilation cross section is estimated as

$$\langle \sigma_A v \rangle \sim \frac{\alpha^2}{M_{\mathrm{weak}}^2} \sim 10^{-9}\,\mathrm{GeV}^{-2}\,. \tag{2.16}$$

Therefore weakly interacting particles with mass of about $\mathcal{O}$(100–1000) GeV may realize the observed dark matter density of $\Omega_{\mathrm{DM}}h^2 \approx 0.119$ [50, 51]. This is the so-called "WIMP miracle". Since neutralinos are weakly interacting massive particles (WIMP), neutralino DM is one of the WIMP DM. Note that in addition to thermal production, decays of heavier supersymmetric particles after the freeze out of neutralinos can also contribute to today's neutralino abundance.

For gravitino DM cases, if gravitinos are produced thermally and they are not diluted by inflation, their today's thermal relic density constrains the mass of gravitino $m_{\tilde{G}}$ as [59],

$$m_{\tilde{G}} \lesssim 1\ \mathrm{keV}\ . \tag{2.17}$$

Such light gravitinos appear in the SUSY models with low SUSY breaking scales, like gauge-mediation supersymmetry breaking (GMSB) models [60, 61]. Gravitino DM can also be produced from decay of heavier supersymmetric particles. For example, existence of gravitino LSP does not affect thermal relic abundance of the NLSP at the time of freeze out since the interaction of gravitino is highly suppressed. Therefore gravitino DM abundance $\Omega_{\tilde{G}}$ can be expressed as,

$$\Omega_{\tilde{G}} = \frac{m_{\tilde{G}}}{m_{\mathrm{NLSP}}}\Omega_{\mathrm{NLSP}}\ , \tag{2.18}$$

with Ω_{NLSP} being the thermal relic abundance which would be realized if the NLSP were stable. Therefore if the next lightest supersymmetric particle (NLSP) is WIMP and $m_{\tilde{G}} \sim \mathcal{O}(m_{\mathrm{NLSP}})$, the observed DM density can be realized naturally [62]. In addition to

[#1] Although the sneutrino LSP is also electrically neutral and non-colored, the sneutrino DM [53, 54] in the MSSM has been excluded [55, 56].

these production processes, gravitinos may also be produced by the inelastic scattering processes during reheating era [63–67]. The gravitino abundance produced by this mechanism is approximately proportional to the reheating temperature [68, 69]. Therefore the reheating temperature is constrained from the abundance of gravitino DM in this kind of scenarios.

Another appealing point of the MSSM is that it might realize the unification of gauge coupling constants. It is expected that if the SM gauge groups $SU(3)_C \times SU(2)_L \times U(1)_Y$ are unified to a single gauge group above a scale M_X, three gauge coupling constants $g_1 = \sqrt{5/3}\, g'$, $g_2 = g$, $g_3 = g_s$ are all equal at and above M_X. With the SM particle contents, it is widely known that these gauge couplings do not meet at any scale. The MSSM introduces new matter particles and hence changes the renormalization group behaviour of these gauge couplings at high energy scales. Surprisingly the degree of unification of gauge couplings are improved drastically when we go to the MSSM from the SM. In Fig. 2.1, 1-loop renormalization group evolutions of $\alpha_i^{-1} \equiv (g_i^2/4\pi)^{-1}$ $(i = 1, 2, 3)$ are presented for both the SM and the MSSM. Here masses of all SUSY particles are assumed to be 2 TeV and above this scale the renormalization group equations of gauge couplings are modified in the MSSM case. It is clear that gauge couplings seem to be unified at the scale of $M_X \sim 10^{16}$ GeV in the MSSM case on the contrary to the SM case [70, 71]. This apparent unification suggests supersymmetric grand unified theory (SUSY GUT) [46, 72–74].

2.2 Split SUSY

2.2.1 Motivation

From the point of view of the original motivation of supersymmetry, which is to remove the fine-tuning in the Higgs potential, the mass scales of SUSY particles are expected not to be apart so much from the weak scale. That is if we adopt the naturalness argument as a guiding principle, it is reasonable to expect that supersymmetric particles will be discovered at the LHC. However array of reports of null results of searches for supersymmetry has been arising doubts whether we should rely on the naturalness argument as a guiding principle. For example gluinos with mass of about 1.8 – 2 TeV are now excluded in simplified models [75, 76]. For a stop, which gives the largest radiative corrections to the Higgs potential due to its large Yukawa coupling, exclusion limits are now pushed up to about 1 TeV [77, 78]. [#2]

Faced with such doubts and the Higgs discovery, the split SUSY scenario, which has been discussed before the LHC era [79–83], has been attracting attention again [84–91]. In the split SUSY scenario, all scalar particles except the lightest Higgs are assumed to be heavy and only fermionic superparticles live around the weak scale. In this sense, the naturalness argument has lost its privilege as a guiding principle in the split SUSY

[#2] In both cases, these limits are relaxed significantly if gluino and LSP are degenerate.

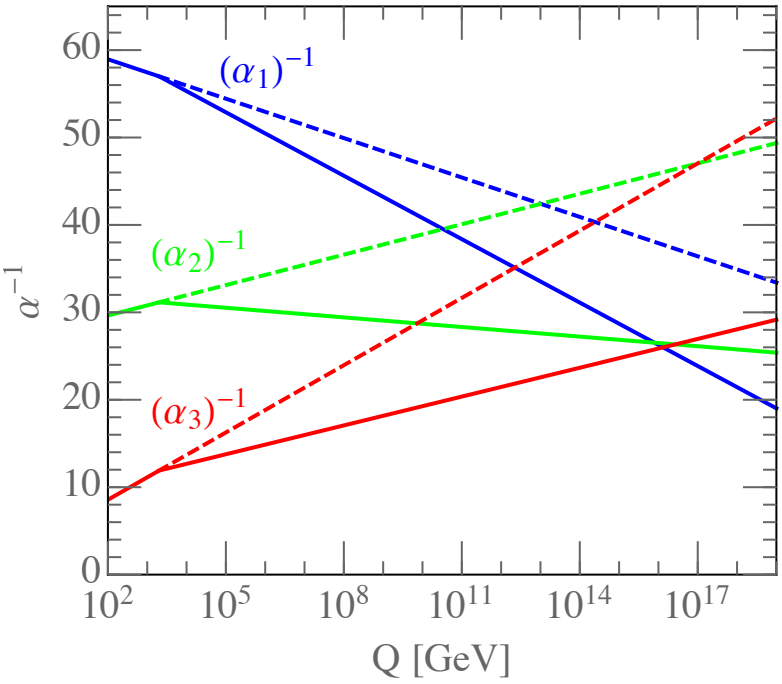

Figure 2.1: 1-loop renormalization group evolutions of the inverse SM gauge couplings in the SM (dashed) and the MSSM (solid) cases. Here the masses of all SUSY particles are assumed to be 2 TeV. $\alpha_1^{-1}(m_z) = 59.01$, $\alpha_2^{-1}(m_z) = 29.59$, and $\alpha_3^{-1}(m_z) = 8.46$ [50] are used.

scenario. Instead of the naturalness argument, unification of the gauge couplings and an explanation for the dark matter are adopted as guiding principles. Although the supersymmetry guided by naturalness argument can solve the hierarchy problem, it has several phenomenological difficulties at the same time. As we will see below, the split SUSY can solve such difficulties with simple setups by giving up solving the hierarchy problem.

One of such difficulties is that observed Higgs mass of 125 GeV [92] is "high" for the MSSM. As is well known, the mass of the lightest Higgs is not a free parameter in the MSSM and its size cannot exceed that of Z boson at tree level. Therefore radiative corrections are crucial to push up the Higgs mass to the observed value [93]. To realize the Higgs mass of 125 GeV in the MSSM, rather large radiative corrections are needed. For example, mass scales of squarks are required to be about 10 (10^4) TeV for $\tan\beta = 10\,(1)$ [94]. [#3] Hence the observed mass of the Higgs implies that squarks are much heavier

[#3] If left-right stop mixing is significant due to the large value of A_t parameter, which is the coefficient of SUSY breaking scalar trilinear coupling of $\tilde{t}_{L,R}$ and the Higgs, light stop can yield enough amount of radiative corrections to the Higgs mass. This can be seen from the 1-loop approximate formula for the Higgs mass given by [22],

$$m_h^2 = m_z^2 \cos^2 2\beta + \frac{3m_t^4}{4\pi^2 v^2}\left(\log\left(\frac{M_S^2}{m_t^2}\right) + \frac{X_t^2}{M_S^2}\left(1 - \frac{X_t^2}{12M_S^2}\right)\right) , \tag{2.19}$$

than the weak scale.

Another difficulties come from the fact that there are many sources of flavour and CP violation in the MSSM Lagrangian. Since no supersymmetric particles have been discovered yet, the supersymmetry must be broken. Reflecting a lack of our knowledge of breaking mechanism of the supersymmetry, we simply add various terms that violate the supersymmetry explicitly to the effective Lagrangian Eq. (2.8) and Eq. (2.9). In the MSSM, only superrenormalizable terms are added. The supersymmetry breaking contributions to dimension less coupling constants are negligible in the low energy effective Lagrangian since they are suppressed by some powers of small coupling constant of the interaction which connects the hidden sector with the observed sector. For example, if supersymmetry breaking effects are communicated by gravitational interaction, their contributions are suppressed by some powers of $1/M_{\rm Pl}$ with $M_{\rm Pl}$ being the reduced Planck scale defined as $M_{\rm Pl} \equiv \left(\sqrt{8\pi G_N}\right)^{-1} \sim 2.4 \times 10^{18}\,{\rm GeV}$. On the other hand, on the dimensional analysis ground, the supersymmetry breaking contributions to coefficients of superrenormalizable (soft) terms can be sizable when the supersymmetry breaking scale is quite large compared to mass scales of known particles. Therefore in the MSSM, effects of supersymmetry breaking at low energy scales are approximated by simply adding soft supersymmetry breaking terms to the effective Lagrangian Eq. (2.8) and Eq. (2.9). The most general form of soft supersymmetry breaking terms which conserve R-parity and $SU(3) \times SU(2) \times U(1)$ gauge symmetries is given by,

$$
\begin{aligned}
\mathcal{L}_{\rm soft} = & -\sum_{i,j} \left(m_Q^2\right)_{i,j} \tilde{Q}_i^* \tilde{Q}_j - \sum_{i,j} \left(m_{\bar{U}}^2\right)_{i,j} \tilde{u}_{R,i} \tilde{u}_{R,j}^* - \sum_{i,j} \left(m_{\bar{D}}^2\right)_{i,j} \tilde{d}_{R,i} \tilde{d}_{R,j}^* \\
& - \sum_{i,j} \left(m_L^2\right)_{i,j} \tilde{L}_i^* \tilde{L}_j - \sum_{i,j} \left(m_{\bar{E}}^2\right)_{i,j} \tilde{e}_{R,i} \tilde{e}_{R,j}^* \\
& - \left(\frac{1}{2} M_1 \tilde{B}\tilde{B} + \frac{1}{2} M_2 \tilde{W}\tilde{W} + \frac{1}{2} M_3 \tilde{g}\tilde{g} + {\rm h.c.} \right) \\
& - \left(\sum_{i,j} A_{i,j}^D h_{i,j}^D \left(\tilde{Q}_i^{\rm T} \epsilon H_1 \right) \tilde{d}_{R,j}^* + \sum_{i,j} A_{i,j}^E h_{i,j}^E \left(\tilde{L}_i^{\rm T} \epsilon H_1 \right) \tilde{e}_{R,j}^* \right. \\
& \left. + \sum_{i,j} A_{i,j}^U h_{i,j}^U \left(\tilde{Q}_i^{\rm T} \epsilon H_2 \right) \tilde{u}_{R,j}^* + {\rm h.c.} \right) \\
& - m_{H_1}^2 H_1^* H_1 - m_{H_2}^2 H_2^* H_2 - \left(B\mu \left(H_2^{\rm T} \epsilon H_1 \right) + {\rm h.c.} \right) ,
\end{aligned}
\tag{2.20}
$$

with $M_S \equiv \left(m_{\tilde{t}_1} m_{\tilde{t}_1}\right)^{1/2}$ and $X_t \equiv A_t - \mu \cot\beta$. Note that radiative corrections to the Higgs mass given in Eq. (2.19) are maximized in the cases where $X_t/M_S \approx \pm\sqrt{6}$, called "maximal mixing scenario" [95]. In the "maximal mixing scenario", a light stop with the mass of about 500 GeV can yield enough amount of radiative corrections to the Higgs mass [22].

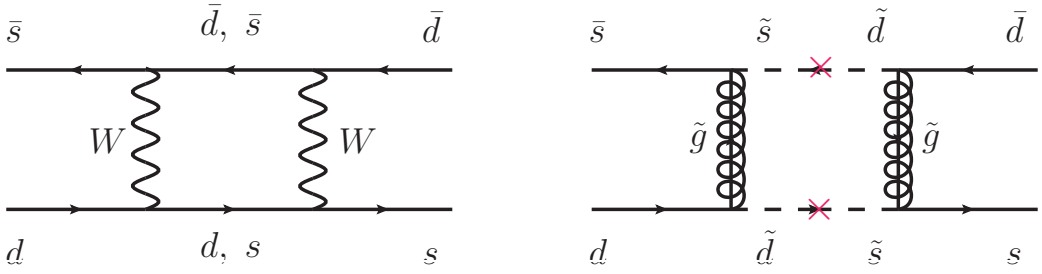

Figure 2.2: Some of the diagrams which contribute to K^0-$\bar{K}^0$ mixing. Left is contribution from the SM. Right is an additional contribution from supersymmetric particles. Sources of flavour violation in the soft supersymmetry breaking squared mass matrices are indicated by $\times$.

and,

$$\mathcal{L}_{\text{maybe soft}} = -\left(\sum_{i,j} C^D_{i,j} h^D_{i,j} \left(\tilde{Q}_i^{\mathrm{T}} H_2^*\right) \tilde{d}^*_{R,j} + \sum_{i,j} C^E_{i,j} h^E_{i,j} \left(\tilde{L}_i^{\mathrm{T}} H_2^*\right) \tilde{e}^*_{R,j} + \sum_{i,j} C^U_{i,j} h^U_{i,j} \left(\tilde{Q}_i^{\mathrm{T}} H_1^*\right) \tilde{u}^*_{R,j} + \text{h.c.}\right) , \tag{2.21}$$

where

$$\epsilon \equiv i\sigma_2 = \begin{pmatrix} 0 & 1 \\ -1 & 0 \end{pmatrix} , \tag{2.22}$$

with i, j denoting flavour indices. Summation over $SU(2)$ and $SU(3)$ indices is assumed implicitly. Soft terms in $\mathcal{L}_{\text{maybe soft}}$ Eq. (2.21), which are not holomorphic in scalar component of chiral superfields, are usually omitted in the MSSM since building UV models which generates non-negligible $\mathcal{L}_{\text{maybe soft}}$ is difficult. It is these soft supersymmetry breaking terms that introduce various sources of flavour and CP violation. For example, soft squared masses $(m^2_\phi)_{i,j}$ ($\phi = Q, \bar{D}, \bar{U}, L, \bar{E}$) are not necessarily diagonal in the basis where SM quarks or leptons are in their mass eigenstate. They may also contain various CP violating phases. Therefore they may induce flavour and CP violating processes. Since there are various stringent experimental constraints on flavour and CP violating processes, the existence of these flavour and CP violating sources is an obstacle to building a viable supersymmetric model [96]. Constraints from electric dipole moment (EDM), meson oscillation, and lepton flavor violation (LFV) have been discussed in the context of supersymmetry models with heavy sfermions [17, 97–100]. Among them, the constraint from K^0-$\bar{K}^0$ mixing tends to be the most stringent one [17]. In Fig. 2.2, some of the diagrams which contribute to K^0-$\bar{K}^0$ mixing are presented. Squarks lighter than about 10^3 TeV may be constrained from the K^0-$\bar{K}^0$ mixing [17], if sizable flavour violation in the squared mass matrices of squarks exist. As another example, consider a lepton flavour violating process of $\mu^- \to e^-\gamma$, which is forbidden in the SM. In Fig. 2.3, some of the diagrams which contribute to this process are shown. Here sources of lepton flavour violation are

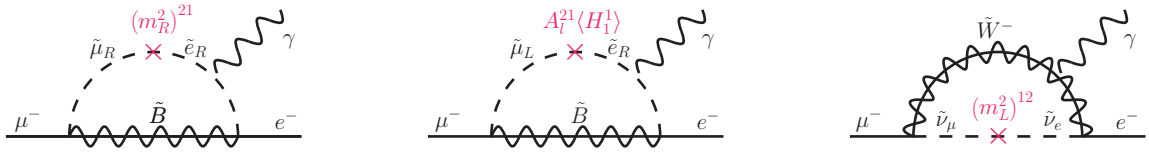

Figure 2.3: Some of the diagrams which contributes to the lepton flavour violating process of $\mu^- \to e^-\gamma$. Sources of lepton flavour violation are indicated by $\times$.

indicated by a cross. If only $(m^2_{\bar{E}})_{i,j}$ has off diagonal elements, its contribution to the decay width is estimated as [101],

$$BR(\mu^- \to e^-\gamma) = 1.5 \times 10^{-5} \times \left(\frac{|(m^2_{\bar{E}})_{21}|}{m^2_{\tilde{\mu}}}\right)^2 \times \left(\frac{100\,\mathrm{GeV}}{m_{\tilde{\mu}}}\right)^4 . \tag{2.23}$$

Here a massless Bino and degeneracy between $\tilde{\mu}_R$ and $\tilde{e}_R$ are assumed and off diagonal elements of $(m^2_{\bar{E}})_{i,j}$ are treated as a perturbation. The size of branching ratio of this lepton flavour violating radiative muon decay is constrained severely by the MEG experiment to be lower than 4.2×10^{-13} [102]. Without sophisticated structures keeping soft squared mass terms diagonal, this limit can be evaded easily if the mass of $\tilde{e}$ and $\tilde{\mu}$ is larger than about 10 TeV.

In general, as we have seen, constraints relevant to the flavour and CP violating terms in the Lagrangian Eq. (2.20) can be evaded if squarks and sleptons are much heavier than the weak scale. These facts also imply that supersymmetric models with heavy scalar particles might be preferred.

There is another difficulty in the supersymmetry models with light sfermions when we extend it to supersymmetric grand unified theory (SUSY GUT). In SUSY GUT, exchange of colored Higgs fermions induces the dimension five proton decay operators [47, 48]. In Fig. 2.4, one of the diagrams which contribute to the proton decay process of $p \to K^+\bar{\nu}_\tau$, which is the dominant decay mode of proton in the supersymmetric $SU(5)$ theories [103–107], is presented. Since proton decay amplitudes with dimension five operators are suppressed by only an inverse power of the colored Higgs mass $M_C \sim M_X$, the colored Higgs mass and the GUT scale are more severely constrained from results of searches for proton decays. From results of the proton decay search at the SuperKamiokande [108], the minimal supersymmetric $SU(5)$ GUT [46, 74] with light sfermions has been excluded [104, 109]. Nevertheless, with heavy sfermions, these constraints can be evaded and sfermions as heavy as $\sim \mathcal{O}(100)$ TeV can revive the minimal SUSY $SU(5)$ GUT [110–114].

So far, we have seen the difficulties in the MSSM which can be evaded in supersymmetric models with heavy scalars. In contrast to scalar fields, smallness of mass of fermionic particles is preserved by chiral symmetry. Therefore it is natural to expect that fermionic supersymmetric particles remain light even if supersymmetric scalar particles are heavy. In addition, there are several arguments that imply the existence of light fermionic su-

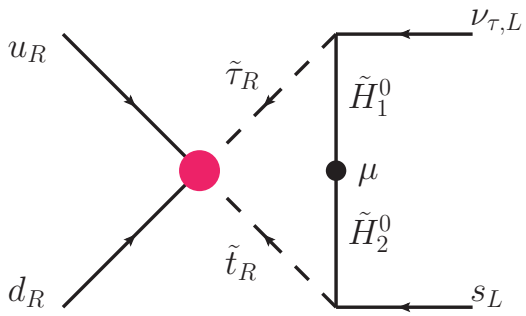

Figure 2.4: One of the diagrams which contributes to the proton decay process of $p \to K^+ \bar{\nu}_\tau$. Dimension five operator is indicated by a red circle. The figure is taken from [104].

persymmetric particles, especially gauginos. Now we are going to give such arguments in the following.

The first reason for our expectation comes from gauge coupling unification. As we already mentioned in Sec. 2.1, the MSSM with supersymmetric particles around the weak scale exhibits nice properties of gauge coupling unification: all the SM gauge groups seem to be unified around $M_X \sim 10^{16}$ GeV. If we adopt the gauge coupling unification as guiding principles, we can find a hint by asking a question: which part of the supersymmetric particles can be pushed up to high scales while preserving the gauge coupling unification property. Of course if we make all supersymmetric particles heavy, renormalization group equations of the gauge couplings are just the SM ones and then the unification will be spoiled. However we can make all of the squarks and sleptons heavy without spoiling the gauge coupling unification. This is because they can be embedded into complete multiplets of $SU(5)$. We can also make one of the scalar Higgs doublets heavy without affecting the behaviour of renormalization group equations significantly since their contribution is small. Contributions to the beta function $\beta_i \equiv \partial g_i / \partial \ln \mu$ from the gauginos are given by,

$$\Delta_{\tilde{W}} \beta_2 = \frac{g_2^3}{16\pi^2} \times \left(\frac{4}{3} \right) , \tag{2.24}$$

$$\Delta_{\tilde{g}} \beta_3 = \frac{g_3^3}{16\pi^2} \times (+2) . \tag{2.25}$$

On the other hand, the contributions from one Higgs doublet scalar field are given by,

$$\Delta_H \beta_{1,2} = \frac{g_{1,2}^3}{16\pi^2} \times \left(\frac{1}{6} \right) , \tag{2.26}$$

which is significantly smaller than the gaugino contributions. [#4] Now we have made all of the scalar supersymmetric particles heavy and find that this modification of the mass spectrum will not spoil the gauge coupling unification so much. Note that this mass

[#4] Here g_1 denotes g' for brevity. When discussing the gauge coupling unification, $\Delta_H \beta_1$ should be multiplied by 3/5.

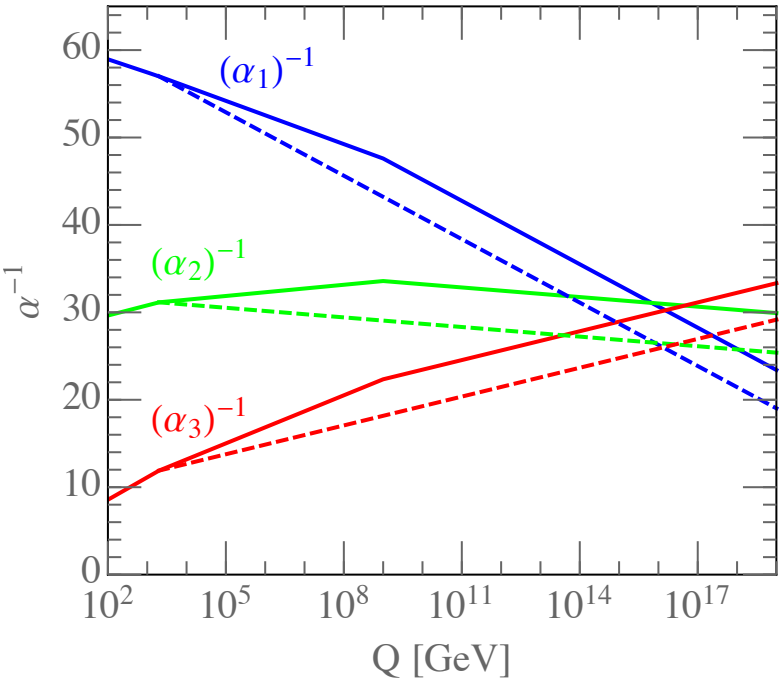

Figure 2.5: 1-loop renormalization group evolutions of the inverse SM gauge couplings in the split SUSY scenario (solid) and the traditional supersymmetric scenario (dashed). Here the masses of the gauginos and higgsinos are set to be 2 TeV in both scenarios. The masses of scalar supersymmetric particles are all set to be 10^9 (2×10^3) GeV in the split SUSY (traditional supersymmetric) scenario. $\alpha_1^{-1}(m_z) = 59.01$, $\alpha_2^{-1}(m_z) = 29.59$, and $\alpha_3^{-1}(m_z) = 8.46$ [50] are used.

spectrum is just the one assumed in the split SUSY scenario. In Fig. 2.5 we present the renormalization group behaviour of the SM gauge couplings assuming both the split SUSY scenario (solid) and the traditional supersymmetric scenario (dashed). Here the masses of the gauginos and higgsinos are set to be 2 TeV in both scenarios. The masses of scalar supersymmetric particles are all set to be 10^9 (2×10^3) GeV in the split SUSY (traditional supersymmetric) scenario. It can be seen that pushing up all supersymmetric scalar particles heavy does not spoil the gauge coupling unification property indeed. From these observations, we can expect that the gauginos still remain light even in the cases where supersymmetric scalars are all made heavy, once we adopt the gauge coupling unification as guiding principles.

The second reason why we expect that fermionic supersymmetric particles remain light is related to the dark matter. As we already mentioned in Sec. 2.1, if a neutralino with mass of about $\mathcal{O}$(100–1000) GeV is the LSP, it can be a suitable candidate of the dark matter. For example, thermal relic of a pure wino with mass of about 3.1 TeV can compose all of the observed dark matter density [115] if non-perturbative effect is considered [116].

For thermal relic of the pure higgsino case, the observed dark matter density is fulfilled if its mass is about 1.1 TeV [117]. For a pure bino, its thermal abundance exceeds the observed dark matter density. Therefore the bino should be mixed with the wino or higgsino to reduce its thermal abundance [118].

From these arguments it can be seen that the neutralino LSP with mass of $\mathcal{O}(1)$ TeV is well motivated as a dark matter candidate. However it should also be mentioned here that these arguments are based on the assumption that the dark matter is thermal relic. Therefore the mass of the neutralino LSP should not necessarily satisfy these conditions. Rather these conditions should be regarded as just a motivation for models with $\mathcal{O}(1)$ TeV neutralinos.

From these arguments, we can say that it is still possible to assume the existence of light supersymmetric fermionic particles on the basis of the gauge coupling unification and an explanation of the dark matter density even in the cases where supersymmetric scalar particles are heavy.

2.2.2 UV Model (AMSB)

In this subsection, we are going to review briefly one of the SUSY breaking models known as Anomaly-Mediated Supersymmetry Breaking (AMSB) [119, 120], which can realize the split SUSY spectrum.

As we already mentioned, supersymmetry must be broken since no supersymmetric particles have been observed yet. Consider cases in which supersymmetry is broken in a hidden sector and its supersymmetry breaking effect is communicated to the observed sector via gravitational interaction. Other unknown interactions which connect the observed sector with the hidden sector might exist at the Planck scale. Such interactions manifest themselves in the effective Lagrangian as interaction terms suppressed by some powers of $1/M_{\rm Pl}$ with $M_{\rm Pl}$ being the reduced Planck scale defined as $M_{\rm Pl} \equiv \left(\sqrt{8\pi G_N}\right)^{-1} \sim 2.4 \times 10^{18}\,\text{GeV}$. If superfield Z whose auxiliary component of F-term acquires a vacuum expectation value is charged under a symmetry of the hidden sector, then interaction terms with the SM gauge superfield W suppressed by a power of $1/M_{\rm Pl}$ such as,

$$\mathcal{L}_{\rm int} \propto \int d^2\theta \, \frac{Z}{M_{\rm Pl}} WW \tag{2.27}$$

are forbidden. It was pointed out [119, 120] that in this case, the effect of supersymmetry breaking in the hidden sector is communicated to the SM gaugino masses dominantly via 1-loop suppressed quantum effect rather than interaction terms suppressed by two powers of $1/M_{\rm Pl}$. Since the quantum effect which communicates the supersymmetry breaking in the hidden sector is related to the anomalous violation of a local superconformal invariance, this mechanism is called Anomaly-Mediated Supersymmetry Breaking (AMSB).

Striking feature of the AMSB is that its effect is always present if we only assume supergravity (and of course supersymmetry breaking in the hidden sector). In this sense, the AMSB is a rather general consequence of supersymmetric theory with gravity. Although the effect of anomaly mediation always exists, it is loop-suppressed. Therefore it plays an important role when contributions of tree-level are absent; for example, when there are no singlet superfields in the hidden sector responsible for supersymmetry breaking.

Contributions of anomaly-mediated supersymmetry breaking effect to the gaugino mass parameters M_a are given by [119, 120],

$$M_a = m_{3/2} \times \left(\frac{\beta_a(g)}{g} \right) = m_{3/2} \times \left(\frac{g_a^2}{16\pi^2} b_a \right) , \tag{2.28}$$

with $\beta_a(g) = g_a^3/16\pi^2 \times b_a$ and $m_{3/2}$ being the beta function of the gauge couplings and gravitino mass, respectively. Here in the MSSM, $b_a = (11,\ 1,\ -3)$. To obtain the masses of gauginos, we should also consider threshold corrections due to the Higgs–Higgsino loop, which might affect the gaugino masses significantly [120, 121]. Contributions of the AMSB and Higgs-Higgsino loop to the gaugino masses are given by [36, 120, 121],

$$M_1 = \frac{g_1^2}{16\pi^2} \left(11 m_{3/2} + L \right) , \tag{2.29}$$

$$M_2 = \frac{g_2^2}{16\pi^2} \left(m_{3/2} + L \right) , \tag{2.30}$$

$$M_3 = \frac{g_3^2}{16\pi^2} \left(-3 m_{3/2} \right) , \tag{2.31}$$

with L denoting the contribution due to the Higgs-HIggsino loop,

$$L \equiv \mu \sin 2\beta \, \frac{m_A^2}{|\mu|^2 - m_A^2} \, \ln \frac{|\mu|^2}{m_A^2} . \tag{2.32}$$

When the contribution L can be neglected, the gaugino mass relations are reduced to [83],

$$M_1 \simeq m_{3/2} \,/\, 120 , \tag{2.33}$$

$$M_2 \simeq m_{3/2} \,/\, 360 , \tag{2.34}$$

$$M_3 \simeq m_{3/2} \,/\, 40 . \tag{2.35}$$

Note that in this case where the gaugino mass are derived purely from the AMSB contribution, M_2 is the smallest and the wino becomes the LSP. Although the situation can be changed when L is not negligible, the wino remains the LSP as long as $|L| \,/\, m_{3/2}$ is less than a few, which is the case for example, when both $|\mu|$ and m_A are nearly equal to the gravitino mass $m_{3/2}$ [35].

In contrast to the gauge superfields, we can write down interaction terms between chiral superfields Φ of matter in the observed sector and chiral superfields Z in the hidden sector such as,

$$\mathcal{L}_{\rm int} \propto \int d^4\theta \, \frac{Z^\dagger Z}{M_{\rm Pl}^2} \, \Phi^\dagger \Phi \tag{2.36}$$

even if Z is not singlet. Therefore it is natural that we expect squared mass of scalar supersymmetric particles m_ϕ^2 to be

$$m_\phi^2 \sim \mathcal{O}(m_{3/2}^2)\,. \tag{2.37}$$

Note that it is possible that supersymmetry breaking in the hidden sector is mediated to the observed sector via not only gravitational effect. In this case, M denoting the scale at which supersymmetry breaking effect is mediated, the masses of scalar supersymmetric particles are expected to be $\sim \mathcal{O}((M_{\rm Pl}/M) \times m_{3/2})$. Essentially, the masses of the scalar particles can be considered as a free parameter even in the AMSB scenario.

From Eqs. (2.29)–(2.31) and Eq. (2.37), it can be seen that the gaugino masses are one-loop suppressed compared to that of gravitino and supersymmetric scalars. That is the split SUSY spectrum may be realized in the AMSB scenario.

One of the striking features of the AMSB scenario is that the gravitino is much heavier than the gauginos, as can be seen from Eqs. (2.29)–(2.31). The heaviness of the gravitino has a impact on the cosmology and ameliorates the so-called gravitino problem [66, 122].

Since decays of the gravitino are suppressed by the Planck scale, primordial unstable gravitinos can be long-lived enough to decay after big-bang nucleosynthesis (BBN) starts. Decay products of such primordial gravitino decays during or after BBN strongly affect the BBN process or spectrum of the cosmic microwave background (CMB). Therefore constraints on the gravitino are imposed in order not to spoil the success of the standard BBN scenario and distort spectrum of the CMB. That is gravitinos should decay fast enough or the abundance of primordial gravitinos should be low enough. If the gravitino mass $m_{3/2}$ is larger than about 50–80 TeV, its lifetime, which is about 10^{-1}–10^{-2} sec, is short enough that all constraints from effects of gravitinos on the BBN can be circumvented [123]. In the AMSB scenario, the gravitino is heavier than about 80 TeV since gluinos lighter than about 2 TeV are now excluded. Therefore the cosmological gravitino problem related to the BBN is easily circumvented in the AMSB scenario. This is one of the appealing points of the AMSB scenario.

Note that there is another problem related to overproduction of the gravitino even if its lifetime is short enough. Since gravitinos are likely to decay much after the freeze-out time of the LSP annihilation process, one LSP is created from one primordial gravitino. Therefore overproduction of the primordial gravitino leads to excess of the LSP abundance. The abundance of the gravitino thermally produced after inflation is approximately proportional to the reheating temperature T_R [68, 69] and the density parameter of the LSP from gravitino decay is given by [123],

$$\Delta\Omega_{\rm LSP}h^2 \simeq 0.054 \times \left(\frac{m_{\tilde{\chi}_1^0}}{100\,{\rm GeV}}\right)\left(\frac{T_R}{10^{10}\,{\rm GeV}}\right)\,. \tag{2.38}$$

By requiring that $\Delta\Omega_{\rm LSP}h^2$ should not exceed the observed dark matter density $\Omega_{\rm DM}h^2 \approx 0.119$ [50, 51], constraint on the reheating temperature $T_R \lesssim \mathcal{O}(10^9)\,{\rm GeV}$ is obtained if we assume the LSP mass of about ~ 1 TeV. The reheating temperature as high as $\mathcal{O}(10^9)$

GeV can open up another intriguing possibility that the leptogenesis [124], which requires the reheating temperature to be $T_R \gtrsim 2\times10^9$ GeV [125–127], works in the AMSB scenario.

As we have discussed cosmological aspects of the AMSB scenario so far, next we are going to discuss collider phenomenology of the AMSB scenario. If the LSP is composed of wino, the LSP and the lightest chargino are nearly mass degenerate. In this case, the LSP is the neutralino and the chargino is slightly heavier due to the EW interaction effect [34, 121, 128]. Because of this small mass difference, decay of the lightest chargino is suppressed and it becomes long lived. In the pure wino limit, the mass difference between the chargino and the neutralino $\Delta m_{\tilde{\chi}_1^\pm - \tilde{\chi}_1^0}$ is calculated to be about 160 MeV at the two-loop level [129] and lifetime of the LSP is about 0.2 ns ($c\tau_{\tilde{\chi}_1^\pm} \sim 6$ cm) [130]. These values are almost insensitive to the LSP mass if $m_{\tilde{\chi}_1^0} \gtrsim 1$ TeV [129]. Since visible decay product of the lightest chargino, which is mainly a pion, is too soft to be detected in a busy environment of hadron colliders, the lightest chargino decaying into the LSP inside the detector is searched for as a disappearing track. Therefore the signal topology of the pure wino LSP scenario is characterized by such high-p_T disappearing tracks besides high-p_T jets and the large missing energy. The ATLAS collaboration sets exclusion limits at 95% confidence level on the mass of charginos. For a pure wino with a lifetime of about 0.2 ns, charginos with mass up to 430 GeV are already excluded with $\sqrt{s} = 13$ TeV and $\mathcal{L} = 36.1\,\text{fb}^{-1}$ data [131].

Prospects of future searches for neutralinos and charginos at 100 TeV pp colliders are presented in Ref. [132]. For nearly mass degenerate wino-like neutralino and chargino case, they study two analyses: monojet search and disappearing track search. They observe that limits set by the monojet analysis is expected to be much weaker than by the disappearing track analysis: assuming the integrated luminosity of $\mathcal{L} = 3000\,\text{fb}^{-1}$, charginos with mass of 1000 – 1400 GeV are expected to be excluded at the 95% confidence level and 300 – 600 GeV are expected to be discovered by the monojet analysis. On the other hand, they claim that charginos with mass of 2200 – 3600 GeV are expected to be excluded and 1700 – 3000 GeV are expected to be discovered by the disappearing track analysis with the mass difference between chargino and neutralino of about 160 MeV being assumed. Note that difficulties in estimation of background contribution to disappearing tracks probably require data based estimation. Therefore these results obtained by disappearing tracks analysis essentially contain large uncertainty. Nevertheless the disappearing track analysis is still promising since it might be able to probe a wino-like chargino with mass of about 3.1 TeV, which can account for all of the dark matter density if thermal production is assumed.

2.3 Metastable Gluino

2.3.1 Phenomenology

One of the features of R-parity conserving supersymmetric theories with heavy scalars is prediction of a metastable gluino [79, 80]. In this section we discuss its phenomenology.

In Fig. 2.6, we present the NLL+NLO gluino pair production cross section [133] as a function of its mass obtained by using PDF sets of CTEQ6.6 [134] with $\sqrt{s} = 13$ (100) TeV in Fig. 2.6a (Fig. 2.6b). Here all squarks are decoupled in the calculation. From these figures, we can expect that gluinos with mass of up to $\sim 3\,(15)$ TeV will be probed at the LHC (future 100 TeV pp colliders) with sufficient amount of data, for example $\mathcal{L} = 3000\,\mathrm{fb}^{-1}$.

Next we are going to discuss gluino decay. When squarks are heavier than the gluino, gluinos decay into two quarks and the neutralino (or chargino);

$$\tilde{g} \to q\,\bar{q}\,\tilde{\chi}^0\,,\; q\,\bar{q'}\,\tilde{\chi}^{\pm}\;(\text{3-body decay})\,, \tag{2.39}$$

or radiatively decay into gluon and the neutralino;

$$\tilde{g} \to g\,\tilde{\chi}^0\;(\text{radiative 2-body decay})\,. \tag{2.40}$$

In Figs. 2.7 and 2.8, some of the Feynman diagrams of amplitudes that contribute to the 3- and radiative 2-body decay are presented respectively. For relatively heavy gluinos, which satisfy $m_{\tilde{g}} \gtrsim 2$ TeV, the 3-body decay dominates over the radiative 2-body decay even if the decay into the Higgsino is allowed [18, 19]. [#5] Therefore we assume that the radiative 2-body decay is negligible in the following.

Note that these amplitudes are suppressed by an inverse power of squared squark mass scale $m_{\tilde{q}}^2$. Therefore if squark mass scales are much higher than the gluino mass, which is the case in the split SUSY scenarios, then decays of gluinos are suppressed significantly and gluinos become long-lived. A long-lived gluino is one of the features of the phenomenology of the split SUSY scenario.

The decay length of gluino $c\tau_{\tilde{g}}$, which is defined as the product of the light speed c and the mean lifetime of the gluino $\tau_{\tilde{g}}$, strongly depends on the masses of the squarks exchanged in the tree-level 3-body decay processes. Assuming that the first-generation

[#5] This can be seen by noting that the ratio ($R_{2/3}$) of the radiative 2-body decay width to that of the 3-body decay is given by [18],

$$R_{2/3} \equiv \frac{\Gamma\left(\tilde{g} \to g\,\tilde{\chi}^0\right)}{\Gamma\left(\tilde{g} \to q\,\bar{q}\,\tilde{\chi}^0\,,\,q\,\bar{q'}\,\tilde{\chi}^{\pm}\right)} \propto \left(\frac{\alpha_s}{4\pi}\right) \times \frac{m_t^2\left|1 - \log\frac{m_{\tilde{t}}^2}{m_t^2}\right|}{m_{\tilde{g}}^2}\,, \tag{2.41}$$

if the Higgsino is lighter than the gluino. On the other hand, if the decay into the Higgsino is forbidden, this large log enhancement is absent and the ratio $R_{2/3}$ is just proportional to $\alpha_s/4\pi$. This is because mass insertion in the quark line is necessary when the neutralino is the Higgsino as shown in Fig. 2.8.

squarks are sufficiently lighter than the second- and third-generation ones, the decay length of the gluino is approximately given by [18–20]

$$c\tau_{\tilde{g}} \simeq 200\ \mu\text{m} \times \left(\frac{m_{\tilde{q}}}{10^3\ \text{TeV}}\right)^4 \left(\frac{2\ \text{TeV}}{m_{\tilde{g}}}\right)^5 , \tag{2.42}$$

where $m_{\tilde{g}}$ is the gluino mass, $m_{\tilde{q}}$ is the masses of all the first-generation squarks (which are assume to be degenerate). In addition, the masses of bino and wino are assumed to be much smaller than the gluino mass, while the higgsino mass is assumed to be larger than the gluino mass. Note that the above expression should be multiplied by a factor of $\simeq 1/3$ if squarks in all generations are degenerate in mass. In Fig. 2.9, we present a contour plot of the gluino decay length $c\tau_{\tilde{g}}$ as a function of gluino mass $m_{\tilde{g}}$ and squark mass $m_{\tilde{q}}$ derived from Eq. (2.42). Eq. (2.42) and Fig. 2.9 indicate that the gluino decay length can be as long as $\gtrsim 100\ \mu$m for the PeV-scale squarks. As we already see in Sec. 2.2.1, such heavy squarks, especially heavy stops, are in fact motivated by the measured value of the mass of the SM-like Higgs boson, $m_h \simeq 125$ GeV [135].

In Sec. 2.2.2, we discuss the AMSB scenario as one of the UV-models which realize the split SUSY spectrum. To see the gluino decay length in the AMSB scenario, we also present a plot of the gluino decay length $c\tau_{\tilde{g}}$ as a function of the gluino mass $m_{\tilde{g}}$, in Fig. 2.10. In the AMSB scenario, the gluino mass is related to the gravitino mass $m_{3/2}$ using Eq. (2.35) and we also assume the relation between the squark mass scale and the gravitino mass of $m_{\tilde{q}} = (1\text{–}20) \times m_{3/2}$. From Fig. 2.10, it can be seen that to observe the longevity of metastable gluinos at collider experiments, the squark mass scales should be heavier than about $(5\text{–}10) \times m_{3/2}$, though a naive expectation implies that $m_{\tilde{q}} \sim m_{3/2}$. Nevertheless, as we mentioned in Sec. 2.2.2, the squark mass scale is not necessarily equal to the gravitino mass. Therefore gluinos can be long-lived enough to be observed as a long-lived particle even in the AMSB scenario.

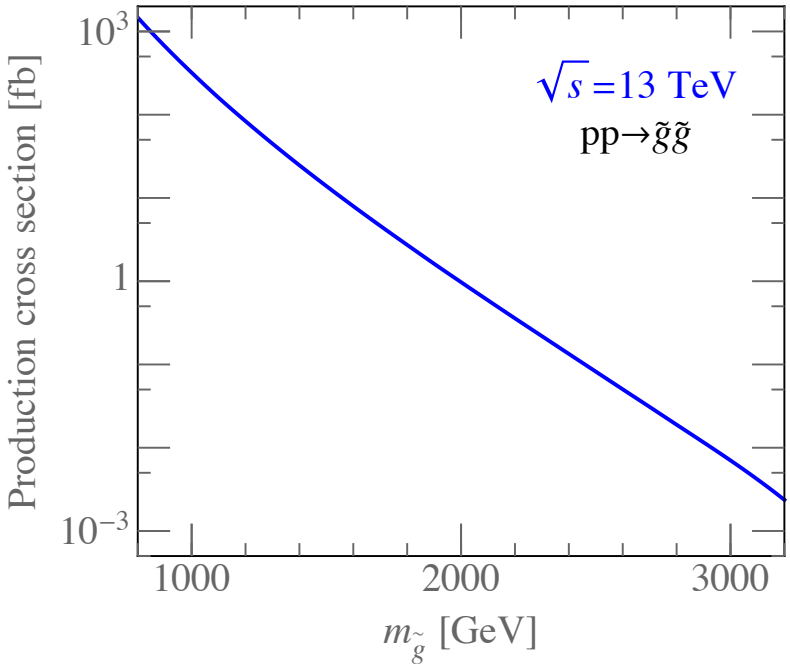

(a) $\sqrt{s} = 13$ TeV

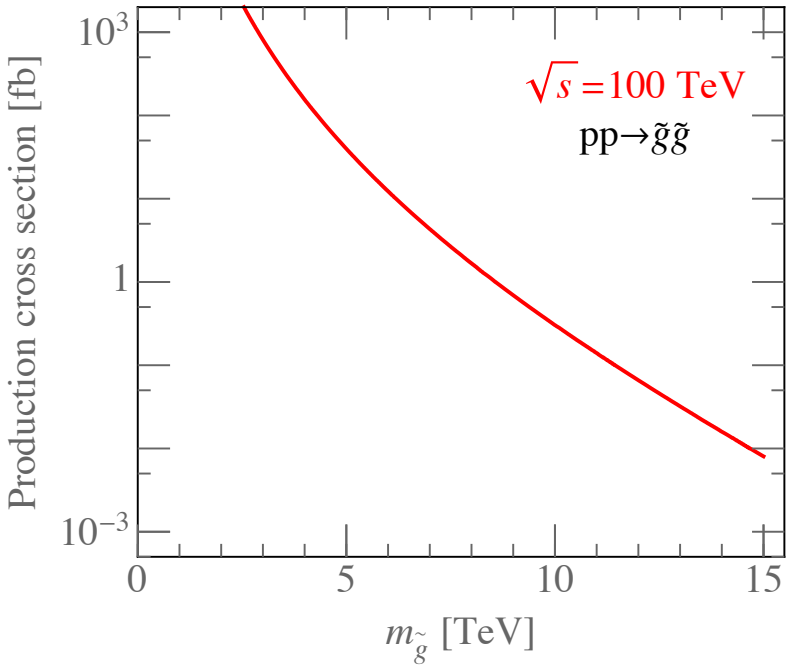

(b) $\sqrt{s} = 100$ TeV

Figure 2.6: The NLL+NLO gluino pair production cross section [133] as a function of its mass obtained by using the PDF sets of CTEQ6.6 [134]. All squarks are decoupled in the calculation. $\sqrt{s} = 13$ (100) TeV in Fig. 2.6a (Fig. 2.6b).

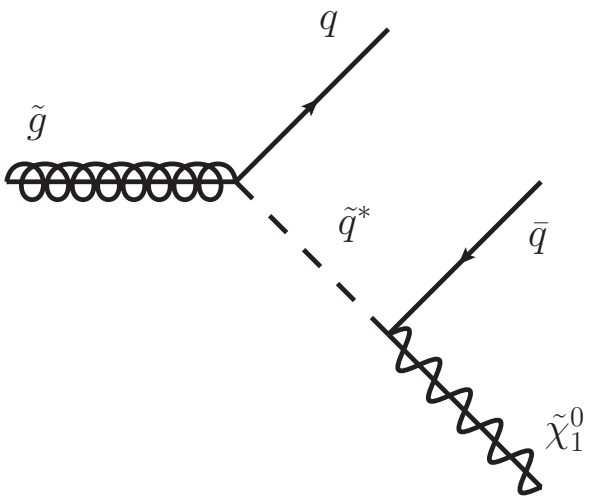

Figure 2.7: A Feynman diagram of amplitude that contributes to the gluino 3-body decay $\tilde{g} \to q\,\bar{q}\,\tilde{\chi}_1^0$.

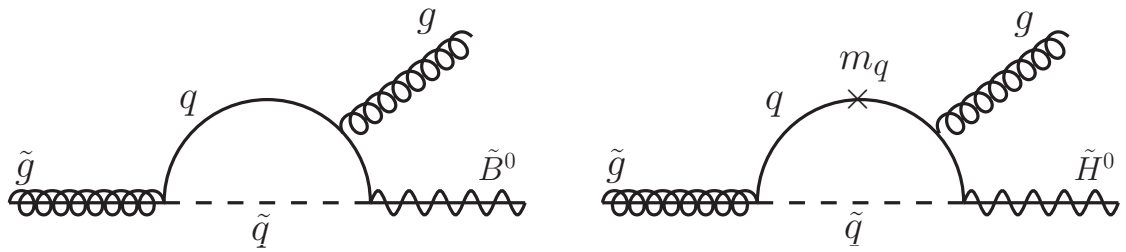

Figure 2.8: Some of the Feynman diagrams of amplitude that contributes to the gluino radiative 2-body decay $\tilde{g} \to g\,\tilde{\chi}^0$. In the left (right) figure, the neutralino is bino (Higgsino).

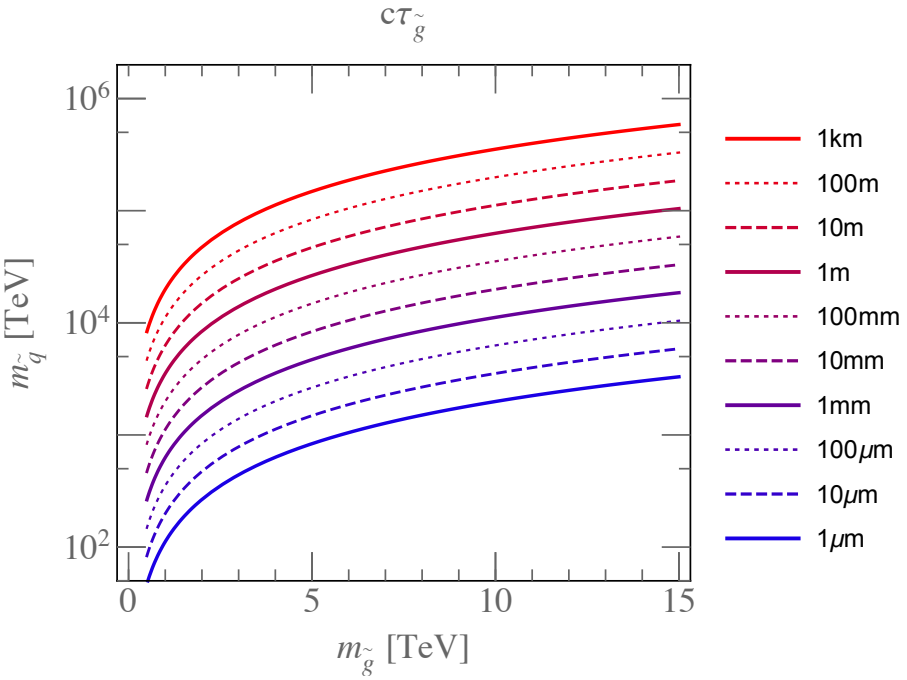

Figure 2.9: A contour plot of the gluino decay length $c\tau_{\tilde{g}}$ as a function of gluino mass $m_{\tilde{g}}$ and squark mass $m_{\tilde{q}}$ derived from Eq. (2.42).

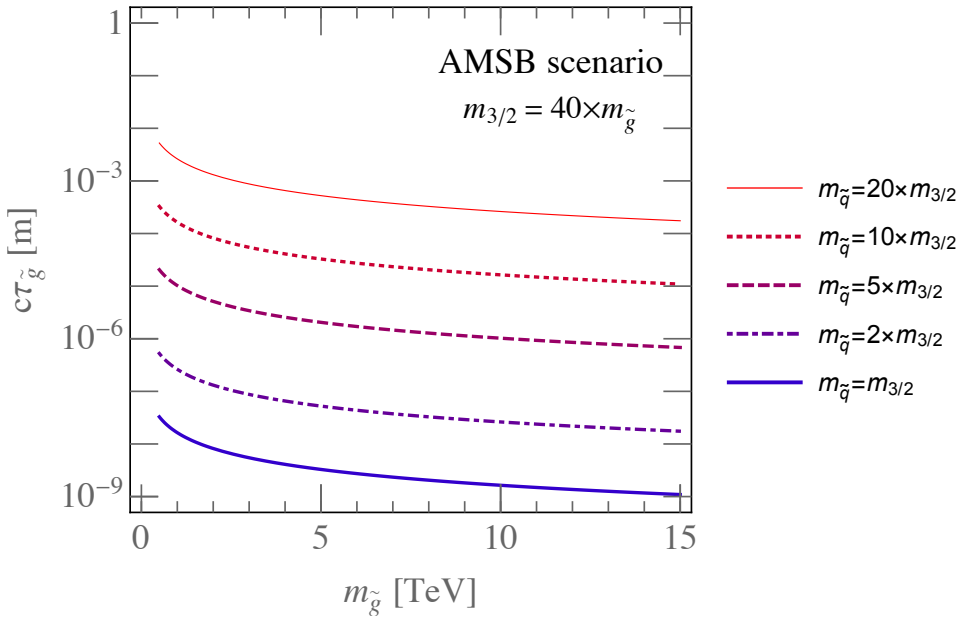

Figure 2.10: A plot of the gluino decay length $c\tau_{\tilde{g}}$ as a function of the gluino mass $m_{\tilde{g}}$. Here we assume the AMSB relation between the gluino mass and the gravitino mass given by Eq. (2.35). The squark mass scale is assumed to be (1–20) $\times$ $m_{3/2}$.

Chapter 3

Review of Searches for Metastable Particles

In Chapter 2, we have seen theoretical motivation for metastable gluinos and its properties. There already exist various searches for metastable gluinos at colliders. In this chapter, we review searches for metastable particles, not restricting ourselves to searches for metastable gluinos.

In general, searches for metastable particles are classified according to the decay length $c\tau$ of target particle. For metastable particles with $c\tau \lesssim \mathcal{O}(10)$ cm, their decay products are the object to be reconstructed. For example, searches for promptly decaying gluinos [75, 136] and displaced vertices searches [32, 38] fall into this category. On the other hand, for $c\tau \gtrsim \mathcal{O}(10)$ cm cases, metastable particles themselves are the object to be reconstructed. Searches utilizing measurement of ionization energy loss [137], time-of-flight [138], and out-of-time decay [139] fall into this category. As can be seen from Fig. 3.1, each search has different sensitivity in the different range of decay length of metastable particles. In this chapter, we review searches belonging to the first category.

In addition to these cases, there is another interesting case; $c\tau \sim 10$ cm. In this case, metastable particles may decay just inside the inner detector, which can provide precise measurement of a charged particle's track. If such charged metastable particles decay into neutral particle and very soft particles inside the inner detector, then such decay may be observed as a disappearing track. We also review this kind of searches in this chapter.

3.1 Detectors

Before seeing searches for metastable particles, we briefly summarize the properties of the detectors. Among various parts of the detector, the inner part, which is designed to provide precise measurement of charged tracks, is most relevant to searches for metastable particles with short decay length. Here, we take the ATLAS detector as an example.

In this thesis, we will adopt the coordinate system adopted by the ATLAS [141]. The origin of the coordinate is placed at the center of the detector. The z-axis is taken in the direction of the beam. The x-axis is directed to the center of the LHC ring and the

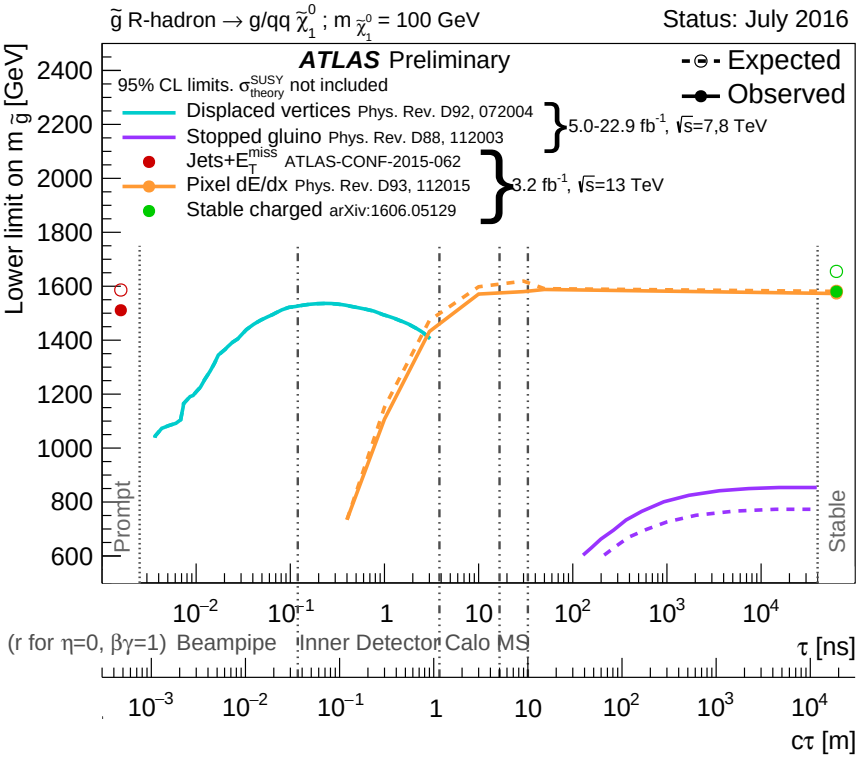

Figure 3.1: Results of various searches for metastable gluinos performed by the ATLAS. The figure is taken from the ATLAS web page [140].

y-axis is directed upwards. The azimuthal angle ϕ is measured around the beam axis and the polar angle θ is measured from the beam direction. The pseudorapidity η, which is defined as $\eta \equiv -\ln(\tan(\theta/2))$, is often used to denote the polar angle. The distance ΔR in the pseudorapidity-azimuthal angle space is defined as $\Delta R \equiv \sqrt{\Delta^2\eta + \Delta^2\phi}$.

3.1.1 Inner Detector

The main purpose of the Inner Detector (ID) is to provide precision measurements of charged particle's momentum and perform precise vertex reconstruction. These are achieved by the ID's full tracking coverage over $|\eta| \leq 2.5$. To measure momentum, the ID is immersed in a magnetic field of 2 T. The ID consists of three parts; from inside, a silicon pixel detector, semiconductor tracker (SCT), and transition radiation tracker (TRT). A quarter-section of the ATLAS inner detector is presented in Fig. 3.3.

The silicon pixel detector [144] consists of four pixel layers in the barrel region, whose radial position is 33.3, 50.5, 88.5, and 122.5 mm. It is designed to achieve high-granularity measurement of charged tracks near the vertices. It can provide at least four precision measurements for charged tracks with $|\eta| < 2.5$. The size of pixel is about 50 μm $\times$ 400 μm and the intrinsic accuracy is about $\sim$ 10 μm in the r-ϕ direction ($r \equiv \sqrt{x^2 + y^2}$) and $\sim$ 100 μm in the z direction [143]. Note that the intrinsic accuracy is better than the size

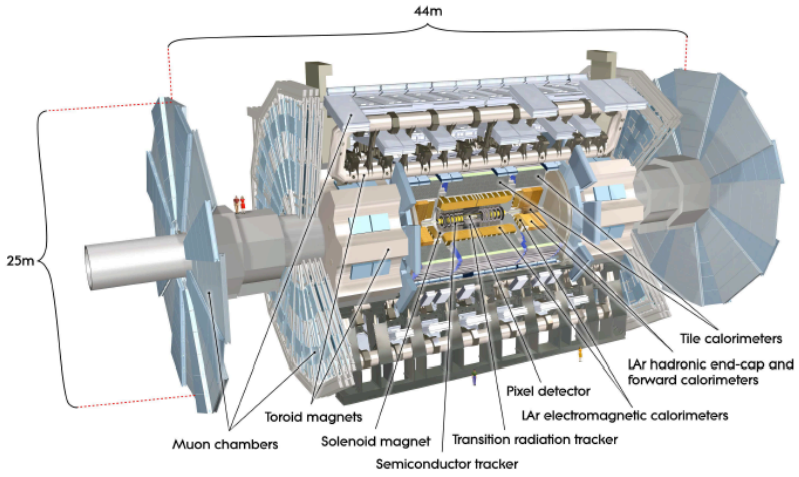

Figure 3.2: Cut away view of the ATLAS detector. The figure is taken from [142].

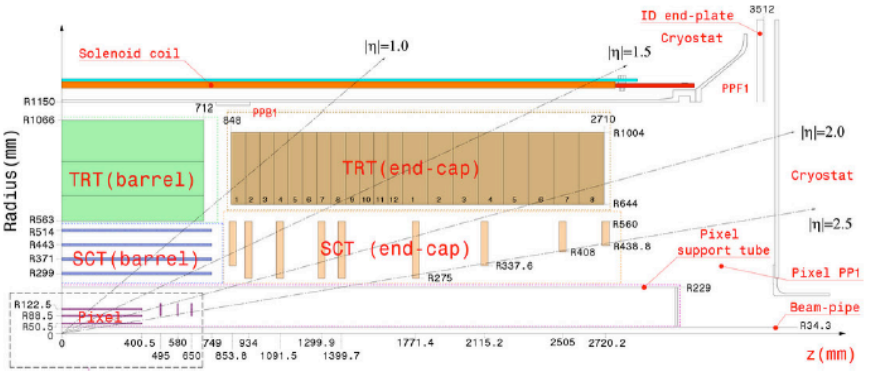

Figure 3.3: A quarter-section of the ATLAS inner detector. The figure is taken from [143].

of pixels. The passage of a single charged particle usually deposits charges also in adjacent pixel cells. By analyzing spatial distribution of released charges, intrinsic accuracy better than the size of pixels is achieved.

The SCT is designed to provide eight precision measurements per track. The barrel SCT consists of eight slices (four layers) of silicon microstrip detectors, whose radial position is 30.0, 37.3, 44.7, and 52.0 cm [141]. [#1] Its intrinsic accuracy is about ~ 20 μm in the r-ϕ direction and ~ 600 μm in the z direction [143].

The TRT [141, 143] consists of straw detectors and is located at the outermost part of the ID. Single track is typically expected to cause 30 hits on the TRT. The straw detectors are parallel to the beam in the barrel region. Hence the TRT does not provide z information in the barrel region. Nevertheless, the TRT can provide precise measurement

[#1] Two detectors pairs are combined back-to-back to form one layer. Therefore there are four layers, not eight, in the barrel region.

of momentum thanks to its position with the large radius. The TRT also provides electron identification by detecting transition-radiation photons created by electrons.

3.1.2 Calorimeter

Outer part of the ID is the calorimeter. The calorimeter consists of an electroweak (EW) calorimeter, which mainly measure the energy of photons, and a hadronic calorimeter, which mainly measure the energy of neutral hadrons. Barrel (end-caps) part of the EW calorimeter covers the range of $|\eta| < 1.475$ ($1.375 < |\eta| < 3.2$). For the hadronic calorimeter, barrel part covers $|\eta| < 1.7$, end-cap part $1.5 < |\eta| < 3.2$, and forward part $3.1 < |\eta| < 4.9$ [141].

At this point we mention the characteristic of energy measurement of charged particles at the tracker and the calorimeter. The energy of charged particles, for example charged pions, can be measured both by the tracker and the (hadronic) calorimeter. However the tracker and the calorimeter differ in energy resolution behaviour. Energy resolution for single charged pion in the centre part of the detector is characterized as, for the calorimeter [145],

$$\frac{\sigma(E)}{E} = \frac{50\%}{\sqrt{E}} \oplus 3.4\% \oplus \frac{1\%}{E} \ , \tag{3.1}$$

and for the tracker,

$$\sigma\left(\frac{1}{p_{\mathrm{T}}}\right) \cdot p_{\mathrm{T}} = 0.036\% \cdot p_{\mathrm{T}} \oplus 1.3\% \ , \tag{3.2}$$

where E and p_{T} are represented in a unit of GeV. From these expressions, it can be seen that energy measurement with better resolution is achieved at the tracker for soft charged particles. On the other hand, for charged particles with high-p_{T}, measurement by the calorimeter seems to be better. For high-p_{T} tracks, their curvature becomes small and this deteriorates momentum measurement in the tracker. Information from the tracker can also be used to subtract contributions from pile-up interactions by rejecting tracks originated from pile-up vertices. [#2] In general, incorporating information from the tracker and the calorimeters leads to better performance [145].

3.1.3 Muon Spectrometer

At the outermost of the detector, muon spectrometer [142] is installed. It measures tracks of charged particles which penetrate through the inner calorimeters. To measure momentum, tracks are deflected by the magnetic field generated by the large superconducting toroid magnets.

[#2] At the ATLAS, a vertex with the largest $\sum_{\mathrm{tracks}\in\mathrm{vertex}} p_{\mathrm{T}}^2$ is reconstructed as a primary vertex and other vertices are reconstructed as pile-up vertices.

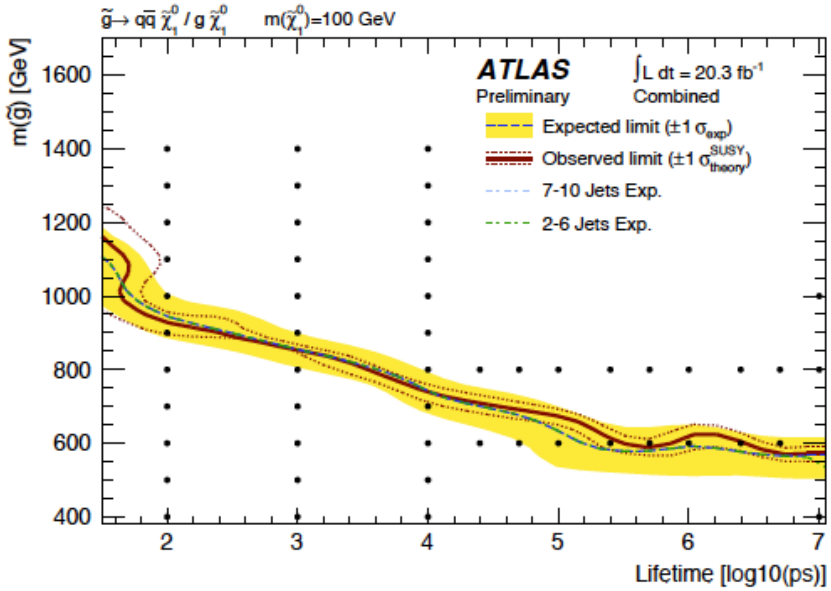

Figure 3.4: 95% CL exclusion limits on gluino mass $m_{\tilde{g}}$ as a function of lifetime. The figure is taken from [146].

3.2 Searches for Metastable Particles

3.2.1 Prompt Searches

Ordinary searches for promptly decaying particles also have sensitivity to metastable particles if their decay length $c\tau$ is small compared to the detector size. In Ref. [146], the ATLAS reinterprets ATLAS SUSY searches for promptly decaying particles [147, 148], which look for promptly decaying new particles in final states with significant hadronic activity ("2-6 jets" [147], "7-10 jets" [148]), large missing energy, and no isolated leptons. In Ref. [146], they study the yield of long-lived gluinos with various decay length by imposing the selection cuts adopted in [147, 148] on simulated samples. With these yields, they reinterpret the exclusion limits set by searches for promptly decaying particles. In Fig. 3.4, their results are presented. It seems that the sensitivity begins to decrease for $c\tau \gtrsim \mathcal{O}(1)$ mm.

3.2.2 Displaced Vertices

In Ref. [32], the ATLAS performs a search for metastable particles with DV reconstruction. They reconstruct DVs from charged tracks measured by the tracker. Their strategy to reduce the SM BG is to require reconstructed DVs to be well separated from the interaction point. With this strategy, they use only tracks satisfying $|d_0| > 2$ mm in their vertex reconstruction procedure. Here, d_0 denotes the transverse impact parameter of tracks with respect to the primary vertex. They also require the vertex to be separated

by at least 4 mm in the transverse plane from all reconstructed PVs. With these requirements, a dominant source of the background is accidental mis-reconstruction of DVs rather than the resolution of tracking. As the background, they consider hadronic interaction, merged vertices, and accidental crossing of vertices and tracks. Here, hadronic interaction means that charged particles emitted from the hadronic interaction with detector materials or gas molecules inside the detector are mis-reconstructed as DVs. Merged vertices means that decays of two short-lived SM particles are combined to be mis-reconstructed as a DV with large track multiplicities. Accidental crossing means that vertices from hadronic interaction or merged vertices are accidentally crossed by other irrelevant tracks to be mis-reconstructed as a DV with high invariant mass $m_{\rm DV}$. Among them, to reduce hadronic interaction, they reject vertices whose reconstructed position is inside the detector material-rich regions. Other background processes are reduced by selecting only candidate DVs with high $m_{\rm DV}$ and large track multiplicities. Reflecting their requirements on tracks and candidate DVs position, the sensitivity of the search begins to decrease for $c\tau \lesssim \mathcal{O}(10)$ mm and seems to be completely vanish for $c\tau < 1$ mm.

In Ref. [38], the CMS performs a search for R-parity violating supersymmetry with DV reconstruction. They search for signal events with large jet multiplicities. However large missing energy does not exist since they consider R-parity violating supersymmetry. Therefore it is difficult to discriminate signal events from multi jet and $t\bar{t}$ production processes by applying selection cuts based on kinematical observables. With this situation, they solely rely on selection cuts based on DV reconstruction to reduce background. They reconstruct DVs using tracks measured by the tracker. As the background, they consider vertices due to the poorly measured tracks. They use only tracks satisfying $|d_0| > 100$ μm in their vertex reconstruction procedure. Here, d_0 denotes the transverse impact parameter of tracks with respect to the beam axis. They intend to reduce the SM background processes with this requirement. Among various their requirements on tracks and candidate vertices, this requirement seems to characterize the sensitivity of their search. Reflecting this requirement, the sensitivity is completely lost for $c\tau \lesssim \mathcal{O}(300)$ μm.

3.2.3 Disappearing Track

In the search based on a disappearing-track signature [131], the special track reconstruction is performed, since the standard track reconstruction [149] is not efficient for tracks of decaying chargino. In the special track reconstruction, only hits not associated with standard tracks are used. (Tracks which are reconstructed in the special procedure are called "tracklet" in Ref. [131] and we will adopt the same notation in the following.) Several requirements are applied to these tracklets in order to reduce contributions from "fake" tracklets [131]. Among them, the tracklet is required to have hits on all four pixel layers, whose radial position is 33.3, 50.5, 88.5, and 122.5 mm respectively, in order to guarantee quality of the tracklet, and the number of hits associated to the tracklet on the strip semiconductor tracker (SCT), whose innermost layer is installed at the radius of 300 mm, is required to be zero, reflecting the disappearing signature of the tracklet. As a

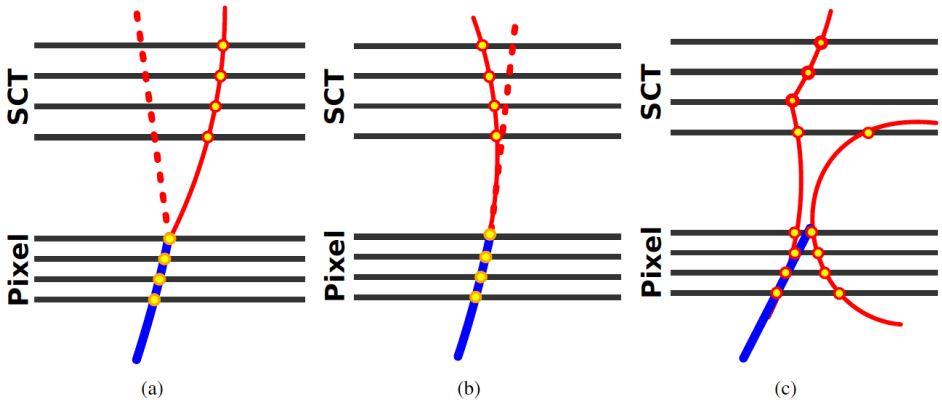

Figure 3.5: Pictures representing possible situations in which hadrons or leptons are mis-reconstructed as a disappearing track. Blue solid lines represent a reconstructed tracklet and red solid (dashed) lines represent track of charged (neutral) particles, and dots indicate the position of hits on the detectors, respectively. In Fig. 3.5a (b), track of a hadron (lepton) is deflected due to a hard scattering (bremsstrahlung) respectively. In Fig. 3.5c, hits from another tracks are associated as a single track and mis-reconstructed as a tracklet. The figure is taken from Ref. [131].

result of these requirements, chargino reconstruction becomes efficient if its decay point radius lies in the region between the pixel layers ($r = 122.5$ mm) and the SCT ($r = 300$ mm).

A track of a hadron or lepton is mis-reconstructed as a tracklet when its hits on the SCT are not associated to the track reconstructed from its hits on the pixel layers. In Fig. 3.5, which is taken from Ref. [131], we present possible situations in which hadrons or leptons are mis-reconstructed as a disappearing track. In Fig. 3.5, blue solid lines represent a reconstructed tracklet and red solid (dashed) lines represent track of charged (neutral) particles, and dots indicate the position of hits on the detectors, respectively. In Fig. 3.5a (b), track of a hadron (lepton) is deflected due to a hard scattering (bremsstrahlung) respectively. If hits of the track after interaction with the detector material all fails to be associated with hits on the pixel layers, these tracks are mis-reconstructed as a tracklet from a decaying chargino. In the case presented in Fig. 3.5c, hits from another tracks are associated as a single track and mis-reconstructed as a tracklet.

In Fig. 3.6, we present the lower limit on the mass of chargino as a function of its proper lifetime set by various ATLAS searches [140]. Note that compared with the results obtained from 8 TeV data [33], it can be seen that the 13 TeV search [131] is more sensitive to charginos with shorter proper lifetime around $\tau \sim 0.2$ ns, which is the predicted lifetime for the pure wino LSP case. This improvement mainly results from installation of the innermost layer pixel detector, the insertable B-layer [152, 153], during the first long shutdown. With this installation, the number of pixel layers is increased to 4 and the radius of the innermost pixel layer is decreased to 33.3 mm. Reflecting these upgrade,

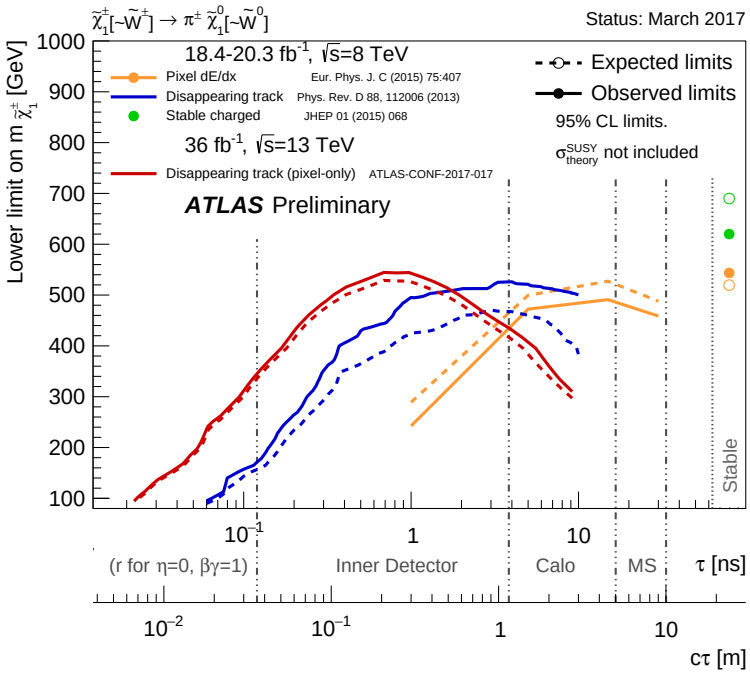

Figure 3.6: The lower limit on the mass of chargino as a function of its proper lifetime set by various ATLAS searches. Pair production of the wino-like chargino and its subsequent decay to the wino-like neutralino and a very soft pion are assumed. Limits presented in red (blue) lines are obtained by the disappearing track based 13 (8) TeV search [33, 131]. Limits presented in yellow lines and dots are obtained by the pixel dE/dx based search [150]. Green dots represent the limit obtained by search for stable charged particles [151]. The solid lines indicate the observed limits, while the dashed lines indicate the expected limits. The figure is taken from the ATLAS web page [140].

hits on the SCT are not required in the 13 TeV search while at least two hits on the SCT are necessary in the 8 TeV search. Therefore the reconstruction efficiency for a chargino which decays in the region between the outermost pixel layer ($r \sim 100$ mm) and the innermost SCT ($r \sim 300$ mm) is much higher than that of in the 8 TeV search. This leads to the improvement of the sensitivity mentioned above.

Chapter 4

Sub-Millimeter Displaced Vertices at the LHC

So far we have discussed theoretical and experimental motivation for metastable particles in the beyond SM physics. In this section, we are going to discuss how such metastable particles can be probed at the LHC. We try to extend the LHC reach for such metastable particles by reconstructing position of their decay point, which is called displaced vertex (DV). We also see how precisely its lifetime can be measured when such metastable particles are discovered. In this thesis, we assume that new metastable particles are pair-produced and its decay products consist of colored particles. Therefore the signal signature is characterized by two reconstructed DVs from which a large number of charged particles are emitted. A typical event topology we are considering is presented in Fig. 4.1. We try to reconstruct the position of DVs by using the position of reconstructed tracks of these charged particles. To make discussion clear, we take search for metastable gluinos as an example. In the following we first mention the procedure of DV reconstruction and treatment of the effect coming from resolution of reconstruction. In the present analysis, we use MC simulation to estimate the efficiency for selecting signal events and the expected number of background events. We also discuss our MC simulation in this section. After these discussion, we present our results showing how far the LHC reach for new metastable particles can be extended by looking at its DV signature.

4.1 Vertex Reconstruction

First, let us briefly summarize how vertices are reconstructed at the LHC experiment. In order to make the argument clear, we use the performance of the ATLAS detector. In this thesis, we concentrate on the case where a large number of charged particles are emitted from vertices, which is the case when the production and the decay of metastable colored particles, like gluino, occurs. Then, with the precise tracking of the charged particles by inner tracking detectors, the decay vertex of the parent particle may be reconstructed.

A similar analysis, *i.e.*, track-based reconstruction of primary vertex in proton-proton collision, has been already performed by the ATLAS [154, 155] and CMS [156] collabora-

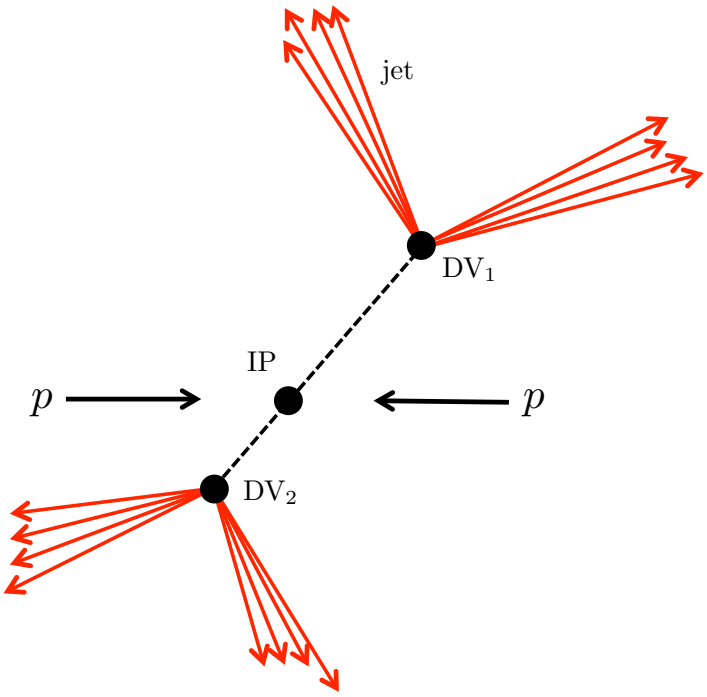

Figure 4.1: A typical event topology we are considering. A pair of new metastable particles are produced at the interaction point (IP). Then they fly over macroscopic length before decaying at points called displaced vertex (DV$_{1,2}$). We assume the metastable particles decay into colored particles. Therefore a large number of particles are emitted from the DV's. Note that two DV's exist in events we are considering.

tions from which we can estimate the accuracy of the determination of the vertex position at the LHC. In Ref. [154], charged tracks with $p_{\rm T} > 400$ MeV were used to reconstruct the primary vertex. In Fig. 4.2, we show the vertex resolution to x- and z-directions (corresponding to the directions perpendicular and parallel to the beam axis) provided by the ATLAS collaboration [154]; the green (dot-dashed) and black (dotted) lines show the data and Monte Carlo (MC) results. Thus, if a sizable number of charged tracks are associated with the vertex, we expect that the vertex position is reconstructed with the accuracy of $\mathcal{O}(10)$ μm. This fact indicates that, if the distance between two decay vertices is longer than $\mathcal{O}(10)$ μm in the pair production process of metastable particles, it may be possible to distinguish two vertices [39]. Existence of two distinct DVs can be used to reduce SM backgrounds, as we discuss below.

In the following, we quantitatively study how well we can improve the discovery reach for the new particles with the reconstruction of DVs. For this purpose, in our MC analysis, we implement an algorithm to reconstruct DVs using charged tracks [39]. Our strategy to reconstruct DVs relies on tracking performance of charged particle tracks in the inner

detector. In this subsection, we are going to see how tracking performance of charged particle tracks is taken into account and then discuss an algorithm used in reconstruction of DVs.

4.1.1 Tracking

The tracking performance of the ATLAS inner detector for $\sqrt{s} = 13$ TeV is given in Ref. [149, 157]. [#1] In our MC analysis, to take account of the performance of track reconstruction, we shift each track obtained from the MC-truth information in parallel by impact parameters; the shifted track is regarded as reconstructed one. We neglect the effect of the curvature of the tracks in this procedure since we focus on DVs which are very close to the interaction point. We also neglect the track parameter resolution regarding its direction, *i.e.*, the azimuthal angle ϕ and the polar angle θ, as their resolution is sufficiently small: $\sigma_\phi \sim 100\,\mu$rad and $\sigma_{\cot\theta} \sim 10^{-3}$ [143]. Thus, we only consider the resolution of the transverse and longitudinal impact parameters, d_0 and $z_0 \sin\theta$, respectively. In this thesis, d_0 means the distance of closest approach between the track and the beam axis and z_0 is the z-coordinate of the closest point of the track to the beam pipe. Here the beam pipe is taken as the z-axis. Effects of these impact parameter resolutions are taken into account by random parallel shift of each track. The resolution of the impact parameters depends on the transverse momentum $p_{\rm T}$ and the pseudorapidity η of the track. In the processes we consider in this thesis, jets have relatively high $p_{\rm T}$ and do not have any preference for the small polar angle regions. In addition, it is found that the η dependences of the resolution of the impact parameters become sufficiently small for $p_{\rm T} \gtrsim$ a few GeV [143, 158]. For these reasons, we neglect the η dependences of the resolution in this analysis. Following Ref. [143], we parametrize the $p_{\rm T}$ dependence of the track impact parameter resolutions as

$$\sigma_X\left(p_{\rm T}\right) = \sigma_X\left(\infty\right)\left(1 \oplus p_X/p_{\rm T}\right) \ , \tag{4.1}$$

(with $X = d_0$ and $z_0 \sin\theta$) where $\sigma_X(\infty)$ and p_X are track-resolution parameters. We determine the values of $\sigma_X(\infty)$ and p_X by fitting this expression onto the $p_{\rm T}$ dependence of the track impact parameter resolution measured by the ATLAS collaboration [157].

4.1.2 Vertxing Algorithm

Next, let us describe the procedure of the vertex reconstruction used in our analysis, which gives the best-fit point of the vertex for a given set of charged tracks. We follow the prescription given in Refs. [155]. In this prescription, the adaptive vertex fitting algorithm [159] is exploited to determine the vertex position. In Fig. 4.3, we present a flow chart of the vertex reconstruction procedure which reconstructs a vertex from a given set of charged tracks. At the outset of this algorithm, crossing points are determined from

[#1] Before the LHC Run-II started, the insertable B-layer (IBL) [152] was installed, which improves the performance of track and vertex reconstruction.

X	$\sigma_X(\infty)$	p_X
d_0	$30\,\mu$m	2.1 GeV
$z_0 \sin\theta$	$90\,\mu$m	1.0 GeV

Table 4.1: Track-resolution parameters appeared in Eq. (4.1). These values are obtained by fitting the expression Eq. (4.1) onto the p_{T} dependence of the track impact parameter resolution measured by the ATLAS collaboration [157]. Here the measured impact parameter resolution for tracks satisfying $p_{\mathrm{T}} > 0.4$ GeV and $|\eta| < 0.2$ are used for fitting. These values are used in our validation procedure.

a pair of two reconstructed tracks (Fig. 4.3 (a)). Then, a vertex seed $\boldsymbol{v}$ is found from the crossing points (Fig. 4.3 (b)) by means of a method called the fraction of sample mode with weights (FSMW) [160] , which we review in Appendix. A. Once the vertex seed is fixed, we determine the position of reconstructed vertex iteratively (Fig. 4.3 (c)–(d)). In the iteration, we first assign a weight w_i, which is given by

$$w_i(\chi_i^2) \equiv \frac{\exp\left(-\chi_i^2/2T\right)}{\exp\left(-\chi_i^2/2T\right) + \exp\left(-\chi_c^2/2T\right)} \ , \tag{4.2}$$

to each track i. Here we use $\chi_c = 3$ [159] and T is a parameter that we choose in the following. For the vertex position $\boldsymbol{v}$ determined above, χ_i^2 is defined as

$$\chi_i^2(\boldsymbol{v}) \equiv \frac{d_i^2(\boldsymbol{v})}{\sigma_{d_0}^2 + \sigma_{z_0 \sin\theta}^2} \ , \tag{4.3}$$

for each track i, where $d_i(\boldsymbol{v})$ denotes its distance from the vertex $\boldsymbol{v}$. A plot of $w_i(\chi^2)$ as a function χ is presented in Fig. 4.4 with varying the value of the parameter T. As can be seen from these expressions and figure, if a track is far away from the vertex $\boldsymbol{v}$, a fairly small weight is assigned to the track. Roughly speaking, a track whose $\chi_i(\boldsymbol{v})$ is larger than χ_c is abandoned; the parameter χ_c plays a role of a cut-off parameter. Note that the parameter T controls the rigorousness of this separation across χ_c. Smaller T means more stringent selection of tracks. Then, we determine a new vertex position by solving

$$\sum_i w_i\left(\chi_i^2(\boldsymbol{v})\right) \chi_i(\boldsymbol{v}_{\mathrm{new}}) \frac{\partial \chi_i(\boldsymbol{v}_{\mathrm{new}})}{\partial \boldsymbol{v}} = 0 \ , \tag{4.4}$$

with respect to $\boldsymbol{v}_{\mathrm{new}}$ (Fig. 4.3 (c)). This new vertex position ($\boldsymbol{v}_{\mathrm{new}}$) is then used as an initial vertex position to repeat this process (Fig. 4.3 (d)). We iterate the above process with varying the parameter T as $T = 256 \to 64 \to 16 \to 4 \to 1 \to 1 \to \ldots$ until $T = 1$ and the vertex position converges within 1 μm. With such variation of the parameter T during the iteration, we can gradually reduce the scope of search for vertex position. This helps the algorithm to avoid choosing a vertex position corresponding to a local minimum

of weighted sum of track χ^2 ($\sum_i w_i \chi_i^2(\boldsymbol{v})$). Note that the parameters in this algorithm are set to be the default values given in Ref. [159] and references therein, though the results are rather insensitive to these parameters.

To validate our modeling of impact-parameter resolution and the vertex reconstruction, we reconstruct the position of primary vertices in minimum-bias events using our procedure [39]. We generate 47,000 minimum-bias event MC samples with `PYTHIA v8.2` [161]. Here, we use only tracks with $p_{\mathrm{T}} > 400$ MeV and $|\eta| < 2.5$ in accordance with the ATLAS study [154]. (For this choice of minimal p_{T}, the best-fit values of $\sigma_{d_0}(\infty)$ ($\sigma_{z_0 \sin\theta}(\infty)$) and p_{d_0} ($p_{z_0 \sin\theta}$) in Eq. (4.1) are presented in Table 4.1.) We then evaluate the resolution of primary vertices as a function of the number of tracks. The results are also shown in Fig. 4.2 [39]. As can be seen from this figure, our result is in good agreement with the ATLAS results [154].

In the following analysis, we will use the procedure explained in this section to determine the best-fit points of the decay vertices of pair-produced new particles.

4.2 Gluino Search with DV's

So far we have seen how DVs are reconstructed by using the position of reconstructed charged tracks. We have also seen our treatment of resolution of tracking and its consequences for DV reconstruction. Now we are going to see the reconstruction of DV signature helps to extend the LHC search reach for new metastable particles. We take search for metastable gluinos at the LHC as an example in the following. In this section, we assume the center of mass energy of 13 TeV.

4.2.1 MC Simulation

MC simulation is used to estimate the efficiency for selecting signal events and the expected number of background events. The effect of tracking resolution on DV reconstruction is also studied with MC simulation. In this subsection, we will describe our MC simulation.

For gluino pair production processes, we first fix the mass and the decay length $c\tau_{\tilde{g}}$ of gluino (as well as other MSSM parameters). Then, event samples for the gluino pair production process are generated; `MadGraph5_aMC@NLO v2` [162] and `PYTHIA v8.2` are used for this purpose. For signal events, we do not include the contribution from additional partons. In our event generation, contributions from squarks are omitted. We generate 50,000 events for each mass of SUSY particles (*i.e.* gluino and the LSP) and lifetime of gluino. Sample points are summarized in Table 4.2. For each event, we determine the flight lengths of two gluinos using the lifetime of the gluino, and hence the position of two decay vertices. The production point of each final-state particle is shifted by the flight length of its parent gluino. We do not consider the effect of gluino hadronization since the fraction of momentum carried away by SM hadrons emitted during hadronization

$m_{\tilde{g}}$	1000, 1200, ... 3200 GeV
$m_{\tilde{\chi}_1^0}$	100 GeV, $(0.2, 0.4, 0.6, 0.7, 0.8) \times m_{\tilde{g}}$, $m_{\tilde{g}} - (150\,\text{GeV}, 100\,\text{GeV}, 50\,\text{GeV}, 25\,\text{GeV})$
$c\tau_{\tilde{g}}$	0, 50, 100, 200, 500, 1000, 3000 μm, 1×10^4, 3×10^4, 1×10^5, 3×10^5, 1×10^6 μm

Table 4.2: Sample points for signal in parameter space. We generate 50,000 events for each sample point. Note that for $m_{\tilde{g}} \leq 1800$ GeV ($m_{\tilde{g}} = 3200$ GeV), we do not generate events at sample points with $m_{\tilde{\chi}_1^0} \leq 600$ GeV ($m_{\tilde{\chi}_1^0} \neq 100$ GeV) since they are not our main concern.

is expected to be small when gluino has a large mass [163]. Signal event samples are normalized according to the NLL+NLO gluino pair production cross section [133] with PDF sets of CTEQ6.6 [134]. The produced gluinos are forced to decay into first-generation quarks and a neutralino with a fixed mass.

As a contribution from SM background, we consider events in the production processes of EW gauge boson (Z and W) and $t\bar{t}$. In our analysis, we do not consider fully hadronic decay processes since we require large missing energy in the events. Diboson production and multi-jet processes are not considered in our analysis since they are expected to give subdominant contribution [75]. For Z boson production, matrix elements are calculated with up to four additional partons. Due to the limitation of our available computational resources, we approximate other sub-dominant processes, W and $t\bar{t}$ production, with calculation up to three and one additional partons respectively. Although the number of generated samples is small, we check that the results are not altered so much for samples calculated with additional one more partons. Therefore, we expect our approximation does not change the results significantly. Samples with the different number of additional partons are merged using five flavour MLM matching scheme with k_t jets [164]. Here we adopt the shower-k_t scheme and the matching parameters QCUT = XQCUT are set to 40 GeV for Z and W and 80 GeV for $t\bar{t}$ production processes according to Ref. [165] respectively. All generated samples are passed to `PYTHIA v8.2` [161] and then `DELPHES v3` [166] for the purpose of parton showering and fast detector simulation.

In general, the tails of distributions of discriminating variables are relevant for a search with large amount of luminosity. Nevertheless the estimation of the contributions to such tails using MC simulation is not easy especially for background processes since a huge amount of MC samples are required. In order to generate MC samples efficiently in the region of phase space which is relevant to such tails, we adopt a technique given in Ref. [165]. The key point is that we divide the generator-level phase space into several regions and generate MC samples in each region individually. Then MC samples in each region are weighted and combined with samples in other regions. Since events with SUSY particles are characterized by high-p_{T} jets and large missing energy ($E_{\mathrm{T}}^{\mathrm{miss}}$), we divide

the generator-level phase space according to the scalar sum of $p_{\rm T}$ of partons in the event ($= \sum_{\rm partons} p_{\rm T} \equiv H_{T,0}$); the generator-level phase space is split into bins of the variable $H_{T,0}$. Widths of the $H_{T,0}$ bins are determined by requiring that the cross section of each bin is about 1/10 of that of the adjacent bin. In Tables 4.3–4.5 we present upper edge values of bin α ($\equiv H_{T,0}^{\rm max}(\alpha)$). We also present cross section before matching $\sigma_{\rm no-mattching}(\alpha)$, the number of MC samples we generate ($N_{\rm gen}(\alpha)$), and equivalent luminosity ($\mathcal{L}_{\rm gen} \equiv N_{\rm gen}(\alpha)/\sigma_{\rm no-mattching}(\alpha)$) respectively. In event generation, we impose a generator-level cut of $|\sum_{{\rm all}\,\nu} \boldsymbol{p}_{\rm T}| > 200$ GeV for $Z \to \nu\bar{\nu}$ and $\left|\sum_{{\rm all}\,l,\nu} \boldsymbol{p}_{\rm T}\right| > 100$ GeV for other processes, respectively. As we already mentioned, event samples in the different bins have different size of weight in our treatment. Here weight w_α associated with samples in the bin α is defined as,

$$w_\alpha = (1/N_{\rm matched}\,(\alpha)) \times \sigma_{\rm matched}\,(\alpha)\,, \tag{4.5}$$

with $N_{\rm matched}(\alpha)$ being the total number of MC samples after matching and $\sigma_{\rm matched}(\alpha)$ being the LO-matched cross section of the bin α. In Figs. 4.5–4.8, we present distributions of $m_{\rm eff}$(incl.) obtained by our MC simulation. Here $m_{\rm eff}$(incl.) is defined as the scalar sum of $E_{\rm T}^{\rm (miss)}$ and the transverse momenta of all jets with $p_{\rm T} > 50$ GeV. In the following, $m_{\rm eff}$(incl.) will be used to define signal regions. The distributions are obtained for events passing a selection requirement `Preselection-H`, whose definition can be found in Table 4.6. From these figures, we can see a relatively good correspondence between $H_{T,0}$ and $m_{\rm eff}$(incl.). Therefore it can be said that dividing the generator-level phase-space according to $H_{T,0}$ is adequate for the estimation of the expected number of events in signal regions based on $m_{\rm eff}$(incl.) values.

Next we describe the definition of reconstructed objects adopted in our study such as jets, charged leptons, and charged tracks. Our definition is mainly based on Ref. [75]. For a charged track to be reconstructed, we require $p_{\rm T} > 1$ GeV and $|\eta| < 2.5$. We remove charged tracks of particles whose production point is outer than the innermost pixel layer at $|\boldsymbol{r}_{\rm T}| = 33.25$ mm. These requirements are also intended to reduce tracks with poor measurement quality. Jets are clustered using `FastJet v3.1` [167] with a jet radius parameter of 0.4 and required to satisfy $p_{\rm T} > 20$ GeV and $|\eta| < 2.8$. For electrons (muons), we require $p_{\rm T} > 7$ GeV and $|\eta| < 2.47$ (2.7) to be reconstructed. We introduce electron (muon) reconstruction probability ($p_{\rm reco.}^{e(\mu)}(p_{\rm T}, \eta)$). Here we assume the default momentum and rapidity dependence of reconstruction probability adopted in `DELPHES v3` [166]. In our treatment, if the absence of reconstructed electrons and/or muons is required, above mentioned sample weight is multiplied by $\prod_{{\rm all}\,e_i}(1 - p_{\rm reco.}^{e_i}) \times \prod_{{\rm all}\,\mu_i}(1 - p_{\rm reco.}^{\mu_i})$.

We would like to mention the validation procedure of our MC simulation at this point. For this purpose, we estimate the expected number of BG events and the expected 95 % confidence level (CL) exclusion limit on gluino mass using our MC simulation. The kinematical selection cuts `Meff-4j-3000`, which is adopted in Ref. [75], is imposed and the integrated luminosity of 36.1 fb^{-1} is assumed. `Meff-4j-3000` is equivalent to imposing both `Preselection-H` defined in Table 4.6 and $m_{\rm eff}$(incl.) > 3000 GeV. We obtain the

	bin α	0	1	2	3	4
$H_{T,0}^{\max}(\alpha)$	(GeV)	600	1200	2000	2900	∞
$\sigma_{\mathrm{no-mattching}}(\alpha)$	(fb)	1.91×10^{3}	1.33×10^{3}	1.83×10^{2}	19.7	2.60
$N_{\mathrm{gen}}(\alpha)$	$(\times10^{3})$	10	130	180	590	90
$\mathcal{L}_{\mathrm{gen}}(\alpha)$	(ab^{-1})	5.23×10^{-3}	0.0975	0.982	29.9	34.6

(a) $Z \to \nu\bar{\nu} + 4j$.

	bin α	0	1	2	3	4
$H_{T,0}^{\max}(\alpha)$	(GeV)	600	1200	2000	2900	∞
$\sigma_{\mathrm{no-mattching}}(\alpha)$	(fb)	2.84×10^{4}	2.42×10^{3}	1.94×10^{2}	17.2	2.03
$N_{\mathrm{gen}}(\alpha)$	$(\times10^{3})$	500	1000	2000	500	500
$\mathcal{L}_{\mathrm{gen}}(\alpha)$	(ab^{-1})	0.0176	0.413	10.3	29.1	247

(b) $Z \to \nu\bar{\nu} + 0, 1, 2, 3\, j$.

	bin α	0	1	2	3	4
$H_{T,0}^{\max}(\alpha)$	(GeV)	600	1200	2000	2900	∞
$\sigma_{\mathrm{no-mattching}}(\alpha)$	(fb)	1.12×10^{5}	2.34×10^{3}	1.75×10^{2}	14.6	1.67
$N_{\mathrm{gen}}(\alpha)$	$(\times10^{3})$	500	500	500	500	500
$\mathcal{L}_{\mathrm{gen}}(\alpha)$	(ab^{-1})	4.46×10^{-3}	0.214	2.85	34.1	300

(c) $Z \to l\bar{l} + 0, 1, 2, 3\, j$.

Table 4.3: The upper edge value of $H_{T,0}$ ($H_{T,0}^{\max}(\alpha)$), cross section before matching ($\sigma_{\mathrm{no-mattching}}$), the number of generated events (N_{gen}), and equivalent luminosity $\mathcal{L}_{\mathrm{gen}}$ for each $H_{T,0}$ bin. For the definition of $H_{T,0}$ and $\mathcal{L}_{\mathrm{gen}}$, see the text. Here values for processes with Z production are presented.

	bin α	0	1	2	3	4	5
$H_{T,0}^{\max}(\alpha)$	(GeV)	400	900	1600	2500	3400	∞
$\sigma_{\text{no-mattching}}(\alpha)$	(fb)	9.01×10^{5}	6.75×10^{4}	4.82×10^{3}	4.15×10^{2}	34.2	4.66
$N_{\text{gen}}(\alpha)$	($\times10^3$)	500	500	5000	4000	1000	500
$\mathcal{L}_{\text{gen}}(\alpha)$	(ab^{-1})	5.5×10^{-4}	7.41×10^{-3}	1.04	9.64	29.2	107

Table 4.4: Same as Table 4.3 except values for processes with W production are presented. Here we consider only processes with leptonic decay of W boson. Up to three additional partons are taken into account ($W \to l\nu + 0, 1, 2, 3\, j$).

	bin α	0	1	2	3	4	5
$H_{T,0}^{\max}(\alpha)$	(GeV)	600	1100	1700	2400	3200	∞
$\sigma_{\text{no-mattching}}(\alpha)$	(fb)	9.62×10^{4}	6.96×10^{3}	5.01×10^{2}	41.6	3.78	0.362
$N_{\text{gen}}(\alpha)$	($\times10^3$)	200	1500	1500	200	200	200
$\mathcal{L}_{\text{gen}}(\alpha)$	(ab^{-1})	2.08×10^{-3}	0.216	2.99	4.81	53.0	552

(a) $t\bar{t} \to$ (semi-leptonic)$+0, 1j$.

	bin α	0	1	2	3
$H_{T,0}^{\max}(\alpha)$	(GeV)	800	1400	2100	∞
$\sigma_{\text{no-mattching}}(\alpha)$	(fb)	510	40.9	3.85	0.342
$N_{\text{gen}}(\alpha)$	($\times10^3$)	50	50	100	50
$\mathcal{L}_{\text{gen}}(\alpha)$	(ab^{-1})	0.0980	1.22	26.0	146

(b) $t\bar{t} \to$ (leptonic)$+0, 1j$.

Table 4.5: Same as Table 4.3 except values for processes with $t\bar{t}$ production are presented. Here we consider only processes with semi-leptonic and leptonic decay of $t\bar{t}$. Up to one additional parton is taken into account.

expected BG event number of 1.4 and the exclusion limit on the gluino mass of 1960 GeV. Comparing these results with the ones reported by the ATLAS collaboration [75], which are 1.6 and 2030 GeV respectively, we can say that our MC simulation reproduces the ATLAS results relatively well.

4.2.2 Event Selection

In our work, we first reduce the number of background events drastically by imposing traditional selection cuts based on kinematical variables such as missing energy and jet $p_{\rm T}$. Then we further reduce background events by imposing our new selection cuts relevant to the distance between two reconstructed DVs. In this subsection, we are going to discuss these event selections and their consequences.

In the present analysis, we optimize two selection cuts based on $m_{\rm eff}$(incl.), which is the scalar sum of $E_{\rm T}^{\rm (miss)}$ and the transverse momenta of all jets with $p_{\rm T} > 50$GeV, and DV measurement to achieve the best sensitivity. We treat all other kinematical selection cuts as a preselection. We expect kinematical selections devised for promptly decaying gluino search are also effective in our analysis, since we mainly focus on the metastable gluino with small decay length compared to the detector size. With this in mind, we mainly follow the selection prescription adopted in the ATLAS promptly decaying gluino search [75]. We study three types of preselection, named `preselection-L,M,H`. For each sample point, a preselection which can set the most stringent limit on gluino mass is adopted. We present the definition of these preselections in Table 4.6 with $E_{\rm T}^{\rm (miss)}$ being the missing energy, $p_{\rm T}(j_i)$ being the transverse momentum of i-th jet, $\Delta\phi$ being the azimuthal angle between the jet and the missing energy, and $m_{\rm eff}(4)$ being the scalar sum of $E_{\rm T}^{\rm (miss)}$ and the transverse momenta of leading 4-jets. Requirements on $\Delta\phi$ and $E_{\rm T}^{\rm (miss)}/m_{\rm eff}(4)$ are intended to reduce contributions from QCD multi-jets processes [75]. Although such multi-jets processes are not considered in the present analysis, these requirements also seem to reject BG events with semi-leptonically decaying t (or $\bar{t}$) efficiently. Here the aplanarity A is defined as $A = 3/2\lambda_3$ with λ_3 being the smallest eigenvalue of the sphericity tensor $S^{i,j}$ $(i, j = x, y, z)$ of the jets [168, 169]. The sphericity tensor is defined as

$$S^{i,j} = \frac{\sum_{k\in\text{jets}} p^i(k)\, p^j(k)}{\sum_{k\in\text{jets}} |\vec{p}(k)|^2}\,, \tag{4.6}$$

where $\vec{p}(k)$ is the spatial component of momentum of jet k in the jet rest frame. All jets with $p_{\rm T} > 50$ GeV are taken into account for the calculation of the sphericity tensor. The aplanarity A measures the sphericity of jet distribution and can take values between 0 and 1/2. $A = 1/2$ ($A = 0$) corresponds to an isotopic (highly-directional) distribution, respectively [169]. In addition to these kinematical requirements, we also require that no electrons and muons are reconstructed. In Figs. 4.9–4.11, we present the $m_{\rm eff}$(incl.) distribution after imposing `preselection-L, M, H` for the SM backgrounds and gluinos with various mass.

In the pair production processes of new metastable particles, no hard particles are produced at the interaction point (assuming that the new particles decay after flying

Requirement	L	M	H
Number of jets with $p_{\mathrm{T}} > 50$ GeV		≥ 4	
$E_{\mathrm{T}}^{(\mathrm{miss})}$ [GeV]		> 250	
$p_{\mathrm{T}}(j_1)$ [GeV]		> 200	
$p_{\mathrm{T}}(j_4)$ [GeV]	> 100	> 100	> 150
$\lvert\eta(j_{i=1,2,3,4})\rvert$	< 1.2	< 2.0	< 2.0
$\Delta\phi(j_{p_{\mathrm{T}}>50\,\mathrm{GeV}}, E_{\mathrm{T}}^{(\mathrm{miss})})_{\mathrm{min}}$		> 0.4	
$E_{\mathrm{T}}^{(\mathrm{miss})}/m_{\mathrm{eff}}(4)$	> 0.3	> 0.25	> 0.2
Aplanarity		> 0.04	

Table 4.6: Definition of `preselection-L, M, H`. In addition to requirements presented in this table, we also require that no electrons and muons are reconstructed.

X	$\sigma_X(\infty)$	p_X
d_0	$23\,\mu$m	3.1 GeV
$z_0 \sin\theta$	$78\,\mu$m	1.6 GeV

Table 4.7: Track-resolution parameters used in our main analysis. Same as Table 4.1 except the measured impact parameter resolution for tracks satisfying $p_{\mathrm{T}} > 1$ GeV and $|\eta| < 0.2$ are used for fitting.

sizable amount of distance) except those from initial state radiation. For this reason, we do not try to determine the position of the interaction point in each event. [#2] We instead use the distance between the two reconstructed DVs. As a DV based variable, we try three candidates;

$$\left|\boldsymbol{r}_{\mathrm{DV1}} - \boldsymbol{r}_{\mathrm{DV2}}\right|, \ \left|(\boldsymbol{r}_{\mathrm{DV1}} - \boldsymbol{r}_{\mathrm{DV2}})_{\mathrm{T}}\right|, \text{ and } \left|(\boldsymbol{r}_{\mathrm{DV1}} - \boldsymbol{r}_{\mathrm{DV2}})_{z}\right|.$$

Here $\boldsymbol{r}_{\mathrm{DV1,2}}$ represents the position of the one of the reconstructed DV respectively. Among them, a one which realizes the best sensitivity is adopted for each sample point.

Now we describe DV reconstruction procedure in a search for metastable gluinos. In gluino searches, we focus on events with relatively high-p_{T} jets. In reconstructing DVs, this allows us to tighten the track selection cuts to $p_{\mathrm{T}} > 1$ GeV in order to eliminate low-p_{T} tracks, whose impact-parameter resolution is rather poor as can be seen from Eq. (4.1).

[#2] We however note that the reconstruction of the primary vertex is possible if hard jets or leptons are associated with the production point. It may also be possible to reconstruct the primary vertex using initial state radiation. Information about the primary vertex may also be utilized to eliminate the background. In addition, information about the position of the beam axis may be useful.

For tracks with $p_{\rm T} > 1$ GeV, the best-fit values of $\sigma_{d_0}(\infty)$ ($\sigma_{z_0\sin\theta}(\infty)$) and p_{d_0} ($p_{z_0\sin\theta}$) in Eq. (4.1) are presented in Table 4.7. We use the these values in the following. We also require the tracks used for DV reconstruction to satisfy $|d_0| < 10$ mm and $|z_0| < 320$ mm [170]. [#3] For DV reconstruction, we only use tracks associated with four-highest $p_{\rm T}$ jets. [#4] If one of these jets contains no track satisfying the above requirements, then we add the fifth-highest $p_{\rm T}$ jet. If more than one jets among these five high $p_{\rm T}$ jets do not offer any tracks which meet the above conditions, then we suppose that DV reconstruction is not possible in such an event.

In the present analysis, reconstructing two DVs from the four jets is not so straightforward since it is not clear which pair of jets originate from a common parent gluino. Reflecting this complexity, we study all possible patterns of pairings out of the four jets. For each paring, we find two DVs, each of which is reconstructed from tracks associated with the corresponding jet pair. Among the possible pairings, we adopt the one which minimizes an objective function $\chi^2_{\rm pairing}$ defined as,

$$\chi^2_{\rm pairing} \equiv \frac{1}{\langle N_{\rm trk}\rangle}\left(\sum_{i\in{\rm trk}(\boldsymbol{v}_1)} w_i\left(\chi^2_i(\boldsymbol{v}_1)\right)\chi^2_i(\boldsymbol{v}_1) + \sum_{j\in{\rm trk}(\boldsymbol{v}_2)} w_j\left(\chi^2_j(\boldsymbol{v}_2)\right)\chi^2_j(\boldsymbol{v}_2)\right) \ , \tag{4.7}$$

with

$$\langle N_{\rm trk}\rangle \equiv \sum_{i\in{\rm trk}(\boldsymbol{v}_1)} w_i\left(\chi^2_i(\boldsymbol{v}_1)\right) + \sum_{j\in{\rm trk}(\boldsymbol{v}_2)} w_j\left(\chi^2_j(\boldsymbol{v}_2)\right) \ , \tag{4.8}$$

where ${\rm trk}(\boldsymbol{v}_{1,2})$ denotes the set of tracks associated with the DV $\boldsymbol{v}_{1,2}$ reconstructed for each pair of jets and track χ^2_i is defined by Eq. (4.3). Here we use the same weight $w_i\,(\chi^2_i)$ as that given by Eq. (4.2) and we take $T = 1$ and $\chi_c = 3$ in the weights.

Since we mainly consider DVs inside the beam pipe, we neglect background vertices from hadronic interactions in the detector materials. Therefore we only consider background vertices which are mis-reconstructed as displaced ones due to the resolution of track impact parameters. With this simplification, we reject an event with a DV whose reconstructed position is inside the detector materials: *i.e.*, 22 mm $\leq |(\boldsymbol{r}_{\rm DV})_{\rm T}| \leq$ 25 mm, 29 mm $\leq |(\boldsymbol{r}_{\rm DV})_{\rm T}| \leq$ 38 mm, 46 mm $\leq |(\boldsymbol{r}_{\rm DV})_{\rm T}| \leq$ 73 mm, 84 mm $\leq |(\boldsymbol{r}_{\rm DV})_{\rm T}| \leq$ 111 mm, or $|(\boldsymbol{r}_{\rm DV})_{\rm T}| \geq$ 120 mm [152, 171–173].

In Fig. 4.12, we show the $|\boldsymbol{r}_{\rm DV1} - \boldsymbol{r}_{\rm DV2}|$ distribution of signal events for a gluino with $m_{\tilde{g}} = 3$ TeV and several values of $c\tau_{\tilde{g}}$. We also present the distribution for the SM background events. In these distributions, `preselection-H` and requirement of $m_{\rm eff}$(incl.) > 2800 GeV are imposed. In Fig. 4.13 we plot a fraction of events passing a selection cut of $|\boldsymbol{r}_{\rm DV1} - \boldsymbol{r}_{\rm DV2}| > r_{\rm cut}$ as a function of $r_{\rm cut}$.

[#3] When two DVs are well separated, one of them can be identified as a pile-up interaction point. Since such mis-identification reduces the efficiency, modifications to the pile-up rejection procedure might be necessary.

[#4] This reflects the event topology under consideration; gluinos are always pair-produced and each of them decays into two quarks and a neutralino.

Selection	Requirments
Preselection	$\in$ (`preslection-L, M, H`)
Lepton veto	No reconstructed electrons and muons
Material veto	No DVs are reconstructed in the detector material regions; *i.e.* (in a unit of mm) $\lvert(\boldsymbol{r}_{\rm DV})_{\rm T}\rvert \notin (22,25), (29,38), (46,73), (84,111), (120,\infty)$
$m_{\rm eff}$(incl.) cut	Require $m_{\rm eff}(\text{incl.}) > (m_{\rm effcut})_{\rm optimal}$ over $m_{\rm effcut} \in (1000\ \text{GeV}, 10^4\ \text{GeV})$
$\Delta r_{\rm DV}$ cut	Require $\Delta r_{\rm DV} > (r_{\rm cut})_{\rm optimal}$ over $\Delta r_{\rm DV} \in (\lvert\Delta\boldsymbol{r}_{\rm DV}\rvert, \lvert(\Delta\boldsymbol{r}_{\rm DV})_{\rm T}\rvert, \lvert(\Delta\boldsymbol{r}_{\rm DV})_{\rm z}\rvert)$ $r_{\rm cut} \in (0, 2\times 10^5 \mu\text{m})$

Table 4.8: A summary of selections we imposed. Here we abbreviate $(\boldsymbol{r}_{\rm DV1} - \boldsymbol{r}_{\rm DV2})$ as $\Delta\boldsymbol{r}_{\rm DV}$.

Note that the background distribution deviates from the signal distribution with $c\tau_{\tilde{g}} = 0$. This is because the flavour content of jets are different between the signal and the background samples. In signal events, gluino decay into only 1st generation quarks, on the other hand, in background events, jets may also be derived from heavy flavour quarks. Such jets may contain metastable SM hadrons. For example, a decay length of B-mesons is about $c\tau_B \sim 400\,\mu$m and they might fly over a few mm before their decay when they are highly boosted. Decay products of these metastable SM hadrons can form a secondary vertex and deteriorate resolution of DV reconstruction. Nevertheless note that existence of metastable SM hadrons in jets does not spoil our DV reconstruction procedure completely. For jets derived from heavy flavour quarks, in addition to metastable SM hadrons, many hadrons are emitted during hadronization. Since the DV reconstruction algorithm we adopt will choose a point where tracks are concentrated most densely as a reconstructed DV position, secondary vertices due to metastable SM hadrons will not be identified as a DV in most cases.

These figures show that if we set $r_{\rm cut}$ to be $\gtrsim 100\ \mu$m, then a significant fraction of SM background fails to pass the selection cut while a sizable number of signal events for $c\tau_{\tilde{g}} \gtrsim 100\ \mu$m remain after the cut. This observation indicates that this cut may be useful to probe a gluino with a decay length of $c\tau_{\tilde{g}} \gtrsim 100\ \mu$m.

4.2.3 Expected Reach with DVs

Now we are going to demonstrate the performance of the new selection cut based on DVs by showing how far we can extend the discovery reach and exclusion limit in a search for metastable gluinos.

After applying one of the `preselection-L,M,H`, we further require events to satisfy

$$m_{\rm eff}(\text{incl.}) > (m_{\rm effcut})_{\rm optimal}\,,\ \Delta r_{\rm DV} > (r_{\rm cut})_{\rm optimal}\ ,$$

where $\Delta r_{\rm DV}$ is one of the DV based observables;

$$\left|\boldsymbol{r}_{\rm DV1} - \boldsymbol{r}_{\rm DV2}\right|,\ \left|(\boldsymbol{r}_{\rm DV1} - \boldsymbol{r}_{\rm DV2})_{\rm T}\right|,\ \text{or}\ \left|(\boldsymbol{r}_{\rm DV1} - \boldsymbol{r}_{\rm DV2})_{z}\right|.$$

Among them, the ones which realize the best sensitivity are adopted for each sample point. We vary the cut parameters $m_{\rm effcut}$ and $r_{\rm cut}$ from 1000 GeV to 10^4 GeV and from 0 to 2×10^5 μm respectively, and adopt the values which optimize the results. We present a summary of selections we impose on events in Table 4.8.

For exclusion limits, we compute the expected 95% confidence level (CL) limits on the gluino mass using the CL_s prescription [174]. We also study expected 5σ discovery reach, which is determined by calculating the expected significance of discovery Z_0 [175]:

$$Z_0 = \sqrt{2\left\{(S+B)\log\left(1+S/B\right) - S\right\}}\ , \tag{4.9}$$

where S (B) is the expected number of signal (background) events. For discovery, we require Z_0 and S to be larger than 5. In Figs. 4.14–4.19, we present optimal cut values ($(m_{\rm effcut})_{\rm optimal}$, $(r_{\rm cut})_{\rm optimal}$) for each sample point with various $c\tau_{\tilde{g}}$. These values are obtained by requiring that they maximize the expected significance Z_0. Here the integrated luminosity of 3000 fb^{-1} is assumed. The preselection and the DV based observables which give the largest value of Z_0 are also presented. In Tables 4.9 and 4.10, the expected number of background and signal events after imposing selection cuts are presented. Here the integrated luminosity of $\mathcal{L} = 3000$ fb^{-1} is assumed. In Table 4.9 (4.10), we consider the massless LSP (moderately degenerate) case, where $m_{\tilde{g}} = 2800$ (2400) GeV and $m_{\tilde{\chi}^0_1} = 100$ (1440) GeV. In these tables, statistical uncertainty of MC simulation (ΔN) is also presented. Here ΔN is estimated as,

$$\Delta N = \mathcal{L} \times \sqrt{\sum w^2_{\rm sample}}, \tag{4.10}$$

where $\mathcal{L}$ is an integrated luminosity, $w_{\rm sample}$ is the MC sample weight given by Eq. (4.5), and the summation is taken over all MC samples passing the selection cut. In Figs. 4.20–4.22, we present the distribution of $m_{\rm eff}$(incl.) after imposing `preselection-H`, the vetos presented in Table 4.8, and $\left|\boldsymbol{r}_{\rm DV1} - \boldsymbol{r}_{\rm DV2}\right| > 100$ (200, 500) μm for the SM background processes and gluinos with various $c\tau_{\tilde{g}}$. Here the mass of gluinos and LSP are set to be 2600 GeV and 100 GeV respectively. From these figures, it can also be seen that the new DV-based selection is effective in reducing the number of the SM background events.

	Z	W	$t\bar{t}$	total
`preselection-H` ($\times 10^3$)	4.7 $\pm$0.3	4.1 $\pm$0.6	4.5 $\pm$0.2	13.3 $\pm$0.7
$m_{\rm eff}$(incl.) $>$ 3600 GeV	12.5 $\pm$1	4.1 $\pm$0.7	1.6 $\pm$0.4	18.2 $\pm$1
$\left\|\boldsymbol{r}_{\rm DV1} - \boldsymbol{r}_{\rm DV2}\right\| > 80$ μm	2.1 $\pm$0.4	0.8 $\pm$0.4	0.2 $\pm$0.1	3.2 $\pm$0.6
$\left\|\boldsymbol{r}_{\rm DV1} - \boldsymbol{r}_{\rm DV2}\right\| > 160$ μm	0.1 $\pm$0.1	< 0.1	< 0.1	0.1 $\pm$0.1
$\left\|\boldsymbol{r}_{\rm DV1} - \boldsymbol{r}_{\rm DV2}\right\| > 200$ μm	0.1 $\pm$0.1	< 0.1	< 0.1	0.1 $\pm$0.1

(a) The expected number of background events.

	$c\tau_{\tilde{g}} = 0$	$c\tau_{\tilde{g}} = 200$ μm	$c\tau_{\tilde{g}} = 500$ μm	$c\tau_{\tilde{g}} = 1$ mm
`preselection-H`	8.2 $\pm$0.1			
$m_{\rm eff}$(incl.) $>$ 3600 GeV	6.9 $\pm$0.1			
$\left\|\boldsymbol{r}_{\rm DV1} - \boldsymbol{r}_{\rm DV2}\right\| > 80$ μm	1.6 $\pm$0.04	5.3 $\pm$0.1	6.3 $\pm$0.1	6.6 $\pm$0.1
$\left\|\boldsymbol{r}_{\rm DV1} - \boldsymbol{r}_{\rm DV2}\right\| > 160$ μm	0.2 $\pm$0.01	2.9 $\pm$0.1	5.1 $\pm$0.1	5.9 $\pm$0.1
$\left\|\boldsymbol{r}_{\rm DV1} - \boldsymbol{r}_{\rm DV2}\right\| > 200$ μm	< 0.1	2.2 $\pm$0.1	4.5 $\pm$0.1	5.6 $\pm$0.1

(b) The expected number of signal events for $m_{\tilde{g}} = 2800$ GeV, $m_{\tilde{\chi}_1^0} = 100$ GeV, and several values of $c\tau_{\tilde{g}}$.

Table 4.9: The expected number of background (a) and signal (b) events after imposing selection cuts. Here the integrated luminosity of $\mathcal{L} = 3000$ fb^{-1} is assumed. Estimated statistical uncertainty of MC simulation is also presented. The masses of gluinos and the LSP are set to be 2800 GeV and 100 GeV respectively.

In the following, we first consider the case in which LSP mass is set to 100 GeV. Then we extend our analysis to the cases in which LSP is degenerate with a gluino.

In Fig. 4.23, we show the expected limit on the gluino mass as a function of $c\tau_{\tilde{g}}$ based on the currently available luminosity of 36.1 fb^{-1} at the 13 TeV LHC (red solid line). Here the mass of LSP is set to be 100 GeV. We can see that, even with the current data, the exclusion limit can be improved by about 100 and 120 GeV for $c\tau_{\tilde{g}} = 0.5$ and 1 mm, respectively. Note that the sensitivity deteriorates for $c\tau_{\tilde{g}} \gtrsim \mathcal{O}(10)$ mm. This is because the signal efficiency is decreased by the requirement on the production point of the tracks and the detector material veto on the reconstructed DV position. To compare the result with the current sensitivities of other gluino searches, we also show the 95% CL exclusion limits given by the ATLAS prompt-decay gluino search with the 13 TeV 36.1 fb^{-1} data (black dotted line) [136], the ATLAS DV search with the 13 TeV 32.8 fb^{-1} data (blue dashed line) [32], and the ATLAS search of large ionization energy loss in the Pixel detector with the 13 TeV 3.2 fb^{-1} data (green dot-dashed line) [137]. Note

	Z	W	$t\bar{t}$	total
`preselection-M` $(\times 10^4)$	1.7 $\pm$0.10	1.7 $\pm$0.22	1.8 $\pm$0.05	5.2 $\pm$0.25
$m_{\rm eff}$(incl.) > 2400 GeV	357 $\pm$41	148 $\pm$13	37 $\pm$5	542 $\pm$44
$\left\|\boldsymbol{r}_{\rm DV1} - \boldsymbol{r}_{\rm DV2}\right\| > 160$ μm	8.2 $\pm$4	3.6 $\pm$1	0.5 $\pm$0.2	12.3 $\pm$4
$\left\|\boldsymbol{r}_{\rm DV1} - \boldsymbol{r}_{\rm DV2}\right\| > 320$ μm	0.2 $\pm$0.1	< 0.1	0.2 $\pm$0.2	0.5 $\pm$0.2
$\left\|\boldsymbol{r}_{\rm DV1} - \boldsymbol{r}_{\rm DV2}\right\| > 400$ μm	< 0.1	< 0.1	< 0.1	< 0.1

(a) The expected number of background events.

	$c\tau_{\tilde{g}} = 0$	$c\tau_{\tilde{g}} = 200$ μm	$c\tau_{\tilde{g}} = 500$ μm	$c\tau_{\tilde{g}} = 1$ mm
`preselection-M`	68.6 $\pm$0.7			
$m_{\rm eff}$(incl.) > 2400 GeV	31.2 $\pm$0.5			
$\left\|\boldsymbol{r}_{\rm DV1} - \boldsymbol{r}_{\rm DV2}\right\| > 160$ μm	0.8 $\pm$0.1	12.7 $\pm$0.3	21.1 $\pm$0.4	24.1 $\pm$0.4
$\left\|\boldsymbol{r}_{\rm DV1} - \boldsymbol{r}_{\rm DV2}\right\| > 320$ μm	< 0.1	4.6 $\pm$0.2	13.9 $\pm$0.3	18.9 $\pm$0.4
$\left\|\boldsymbol{r}_{\rm DV1} - \boldsymbol{r}_{\rm DV2}\right\| > 400$ μm	< 0.1	2.5 $\pm$0.1	10.2 $\pm$0.3	16.2 $\pm$0.4

(b) The expected number of signal events for $m_{\tilde{g}} = 2400$ GeV, $m_{\tilde{\chi}_1^0} = 1440$ GeV, and several values of $c\tau_{\tilde{g}}$.

Table 4.10: Same as Table. 4.9 except now the `preselection-M` is imposed and the masses of gluinos and the LSP are set to be 2400 GeV and 1440 GeV respectively.

that we extend the black dotted line for the ATLAS prompt-decay gluino search up to $c\tau_{\tilde{g}} \sim \mathcal{O}(1)$ mm just for comparison; the reach of the prompt-decay gluino search is expected to become worse when $c\tau_{\tilde{g}} \gtrsim \mathcal{O}(1)$ mm [146]. The existing metastable gluino searches are insensitive to a gluino with $c\tau_{\tilde{g}} \lesssim 1$ mm, as shown in Fig. 4.23 (blue dashed and green dot-dashed lines), to which searches with the new DV cut may offer a good sensitivity. In this sense, this new search strategy plays a complementary role in probing metastable gluinos.

In Fig. 4.24, we show the expected 95% CL exclusion limits (in dotted lines) and 5σ discovery reaches (in solid lines) for gluino as functions of $c\tau_{\tilde{g}}$ for different values of integrated luminosity at the 13 TeV LHC run. The mass of LSP is also set to be 100 GeV. Notice that the expected reaches for an extremely small $c\tau_{\tilde{g}}$ should correspond to those for the prompt-decay gluino with the same data set since the new DV cut plays no role in this case. As can be seen from this figure, the reach for the gluino can be extended with the help of the additional DV selection cut for $c\tau_{\tilde{g}} \gtrsim 100$ μm; for instance, for a gluino with $c\tau_{\tilde{g}} \sim \mathcal{O}$(1–10) mm, the expected discovery reach for the gluino mass can be extended by as large as ~ 240 GeV (320 GeV) with an integrated luminosity of $\mathcal{L} = 300$ fb^{-1} (3000 fb^{-1}). These reaches for a gluino with $c\tau_{\tilde{g}} \sim \mathcal{O}$(1–10) mm are

obtained by `preselection H` and $|\boldsymbol{r}_{\rm DV1} - \boldsymbol{r}_{\rm DV2}|$ with $(m_{\rm effcut})_{\rm optimal} = 2400$ GeV (3400 GeV) and $(r_{\rm cut})_{\rm optimal} \sim 300\,\mu$m ($160\,\mu$m) for $\mathcal{L} = 300\,{\rm fb}^{-1}$ ($3000\,{\rm fb}^{-1}$). Compared to a promptly decaying gluino, where $(m_{\rm effcut})_{\rm optimal} = 3400$ GeV (4200 GeV) respectively, the $m_{\rm eff}$(incl.) selection cut is loosened and the new DV cut plays an important role in background rejection. As we already mentioned, because charged tracks with $|d_0| > 10$ mm are not included in the analysis, and also because we reject all events with a DV whose reconstructed position radius is larger than 120 mm, the expected exclusion limits decrease for $c\tau_{\tilde{g}} \gtrsim 100$ mm. Such a larger $c\tau_{\tilde{g}}$ region can however be covered by other long-lived gluino searches.

Next we discuss the cases where gluino and the LSP are degenerate. In Fig. 4.25, we show the expected 95% CL exclusion limits (dotted lines) and 5σ discovery reaches (solid lines) for gluino as functions of $c\tau_{\tilde{g}}$ for different values of integrated luminosity at the 13 TeV LHC run. In this figure, the mass difference between gluinos and the LSP is set to be 100 GeV. We can see that the limits and the reaches grow especially for $c\tau_{\tilde{g}} \sim \mathcal{O}(1$–$100)$ mm. Contrary to the massless LSP case, we cannot set reach or limit larger than 1000 GeV for the case of relatively low luminosity when gluino and LSP are degenerate.

Note that since relatively tight requirements on jet $p_{\rm T}$ are imposed in our preselections, they are not optimized for the cases where gluino and LSP are degenerate. Therefore our results for degenerate cases may be improved if we relax requirements on jet $p_{\rm T}$ in our preselections. This is also implied by the fact that the ATLAS collaboration reported that for degenerate cases, the signal region `Meff-5j-1400`, where requirements on $p_{\rm T}$ for 2nd – 4th jets are relaxed and, instead, another 5th jet is required, provided the best sensitivity [176]. Since the number of additional partons in our MC simulation is restricted less than five, we do not try to study preselections which require the existence of the 5th jet and leave it for future study.

Finally, we present the expected 95% CL exclusion limits and 5σ discovery reaches in terms of the gluino and the LSP masses in Figs. 4.26–4.31. In these figures, we assume several values of $c\tau_{\tilde{g}}$. In Fig. 4.27 we also present the observed 95% CL exclusion limit (black dotted line) given by the ATLAS [75]. Relatively good agreement between the ATLAS result and our result for $c\tau_{\tilde{g}} = 0\ \mu$m (black solid line) can be seen except in regions where gluinos and the LSP are highly degenerate. Since more optimized preselections are used for highly mass degenerate cases in Ref. [75], we expect that the discrepancy in the mass degenerate regions comes from the difference in adopted preselections. Therefore we consider that the agreement seen in Fig. 4.27 also validates our MC simulation.

From Figs. 4.26–4.31, it can be seen that application of the new DV cut leads to sizable improvement in the discovery reach and the exclusion limit for $c\tau_{\tilde{g}} \gtrsim 200\,\mu$m. As we already mentioned, the results for $c\tau_{\tilde{g}} = 0\ \mu$m (black solid lines) corresponds to results which would be obtained without introducing the new DV cut. The improvement is maximized for $c\tau_{\tilde{g}} \sim \mathcal{O}(1$–$10)$ mm cases. Note that the improvement is most significant in cases where gluino and the LSP are degenerate. When gluino and the LSP are degenerate, jets from gluino decays and the missing energy become soft. Therefore in these cases,

traditional selections which rely solely on kinematical observables such as jet $p_{\rm T}$ and the missing energy will lose their power. This is the reason why introduction of the selection cut based on DV observables leads to the great enhancement when metastable gluino and LSP are degenerate.

At this point, we mention our treatment of the effect of pile-up events. At the High-Luminosity LHC (HL-LHC), the average number of pile-up events per bunch crossing $\langle\mu\rangle \sim 140$ is expected. Although quite busy environment is expected, we do not include the effect of pile-up events in our analysis. The reason is two-folded. Firstly the effect of pile-up events to selections based on kinematical variables is expected to be small [177]. Secondary we expect that the contamination of tracks from pile-up events does not affect reconstruction of DVs severely since we reconstruct DVs using tracks only in high-$p_{\rm T}$ jets and the DV reconstruction algorithm determines the point where tracks are most concentrated as the position of a DV. From these considerations, we expect the effect of pile-up events to DV search to be limited. [#5]

4.2.4 Lifetime Measurement

If a new metastable particle is discovered at the LHC, measurement of its lifetime is of crucial importance to understand the nature of new physics behind this metastable particle. In this subsection, we discuss the prospect of the lifetime measurement by means of the DV reconstruction method we have discussed.

To see the prospect of the lifetime measurement, we study the expected significance of rejection of a hypothesis that the gluino decay length is $c\tau_{\tilde{g}}^{(\rm hypo)}$ for gluino samples with a decay length of $c\tau_{\tilde{g}}$. Event samples are binned according to the DV distance $|\boldsymbol{r}_{\rm DV1} - \boldsymbol{r}_{\rm DV2}|$ of the events. Then the expected significance $\langle Z_{c\tau_{\tilde{g}}^{(\rm hypo)}}\rangle_{c\tau_{\tilde{g}}}$ is determined as $\langle Z_{c\tau_{\tilde{g}}^{(\rm hypo)}}\rangle_{c\tau_{\tilde{g}}} \equiv \sqrt{\Delta\chi^2(c\tau_{\tilde{g}}^{(\rm hypo)}, c\tau_{\tilde{g}})}$, where

$$\Delta\chi^2(c\tau_{\tilde{g}}^{(\rm hypo)}, c\tau_{\tilde{g}}) = \sum_{\text{bin } i} \frac{\left\{S_i(c\tau_{\tilde{g}}^{(\rm hypo)}) - S_i(c\tau_{\tilde{g}})\right\}^2}{S_i(c\tau_{\tilde{g}}^{(\rm hypo)}) + B_i}\,. \tag{4.11}$$

Here, $S_i(c\tau)$ is the expected number of signal events in the bin i on the assumption that gluinos have a decay length of $c\tau$, while B_i is the number of SM background. In Figs. 4.32a and 4.32b, we show the expected upper and lower bounds on the decay length as a function of $c\tau_{\tilde{g}}$ for a gluino with a mass of 2.2 TeV. Here we impose `preselection-H` and require $m_{\rm eff}(\text{incl.}) > 3500$ GeV. From the figures, we find that a metastable gluino with $c\tau_{\tilde{g}} \gtrsim 30$ (60) μm can be distinguished from a promptly decaying one with the significance of 2σ (5σ) with an integrated luminosity of 3000 fb^{-1}. Moreover, Fig. 4.32b shows that the decay length of a gluino with $c\tau_{\tilde{g}} \sim \mathcal{O}(100)$ μm can be measured with an

[#5] However further consideration to the effect of pile-up events might be required when the center of mass energy is increased.

$\mathcal{O}(1)$ accuracy at the high-luminosity LHC. With such a measurement, we may probe the squark mass scale $m_{\tilde{q}}$ via Eq. (2.42) even though squarks are inaccessible at the LHC. Such measurement will shed light on the SUSY mass spectrum as well as the mediation mechanism of SUSY-breaking effects.

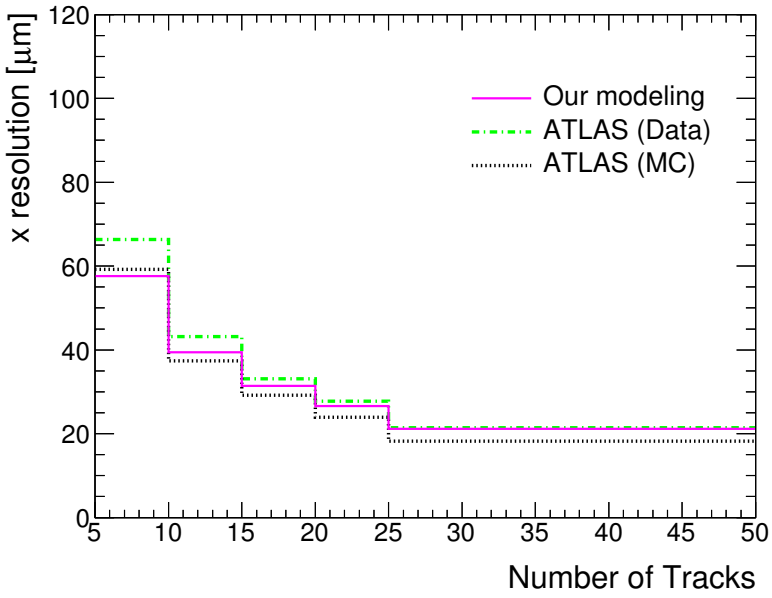

(a) x-direction

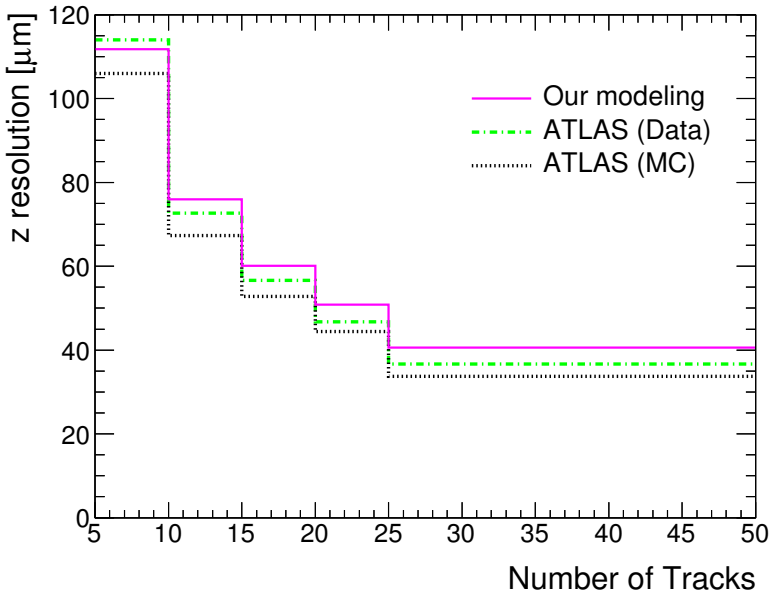

(b) z-direction

Figure 4.2: The resolutions of reconstructed primary vertex position as a function of the number of tracks associated with the primary vertex [39]. The resolutions obtained with our modeling are shown in purple lines while those provided by the ATLAS collaboration [154] are shown in green dot-dashed (derived from data) and black dotted (derived from MC samples) ones.

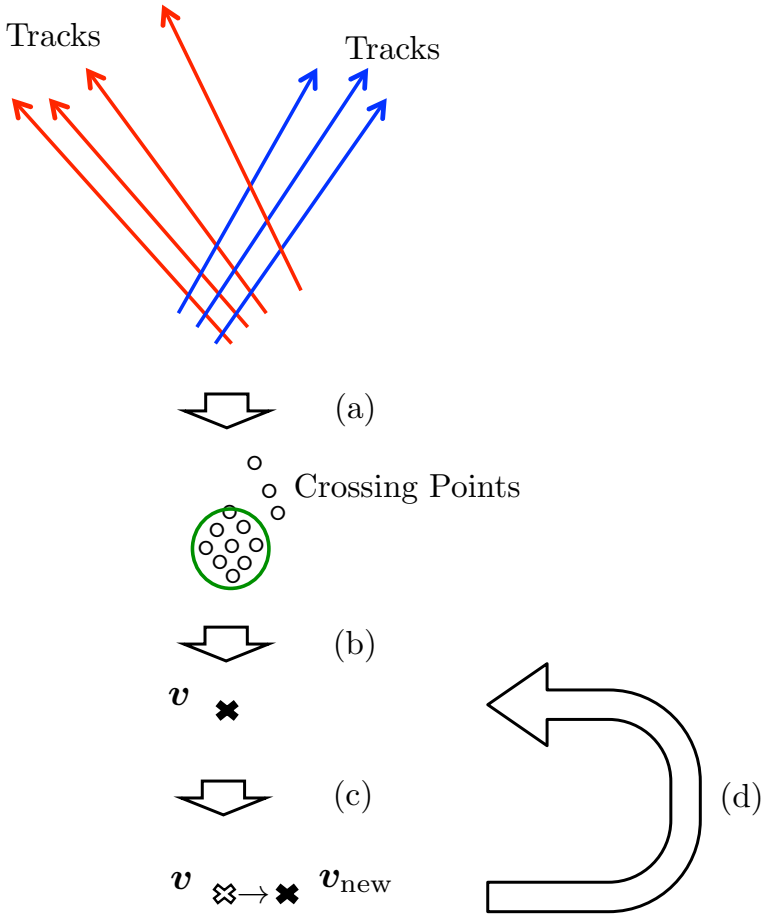

Figure 4.3: A flow chart of the vertex reconstruction procedure which reconstructs a vertex from a given set of charged tracks. In step (a), crossing points are determined from a pair of two reconstructed tracks. In step (b), a vertex seed $\boldsymbol{v}$ is found from the crossing points by means of a method called the fraction of sample mode with weights (FSMW) [160]. Then, in step (c), a new vertex position $\boldsymbol{v}_{\text{new}}$ is determined by solving Eq. (4.4). This new vertex position is used as an initial vertex position to repeat this process (step (d)).

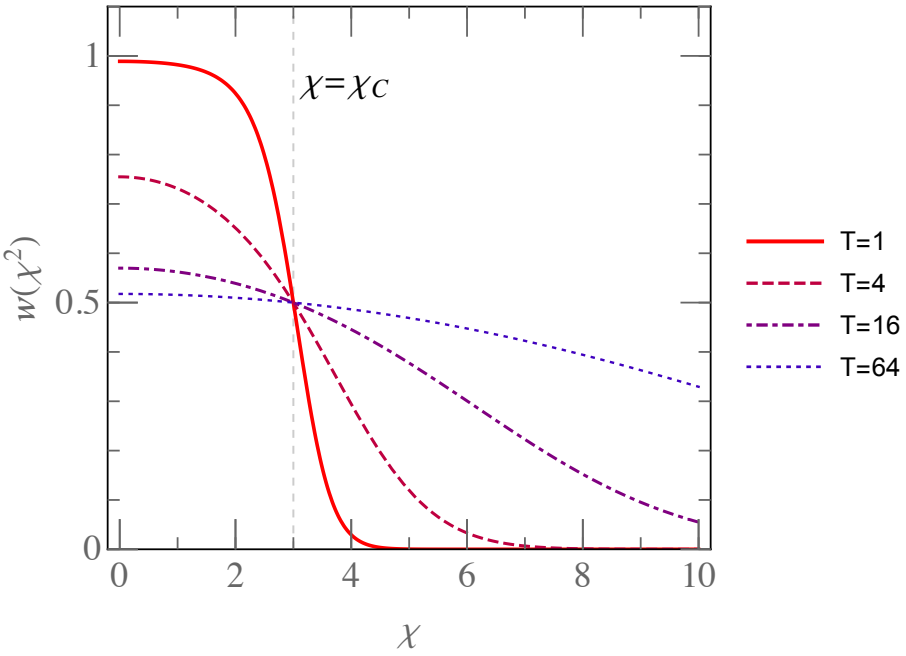

Figure 4.4: Plot of the weight function $w_i(\chi_i^2)$ given in Eq. (4.2) with several values of T. Here χ_c is set to 3.

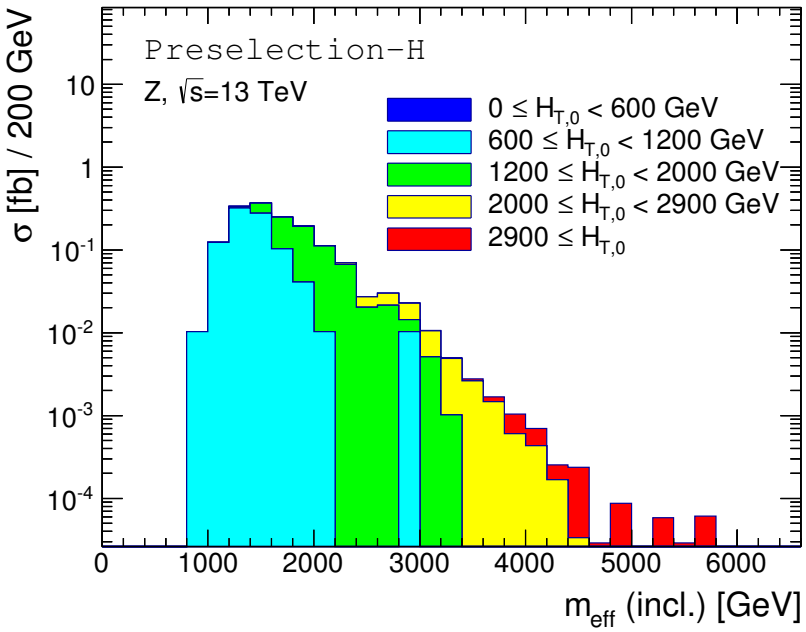

Figure 4.5: Distribution of m_{eff}(incl.) after imposing `preselection-H` defined in Table 4.6 for the SM background processes with Z boson. Contributions from MC samples in different $H_{T,0}$ bins are filled with different colors.

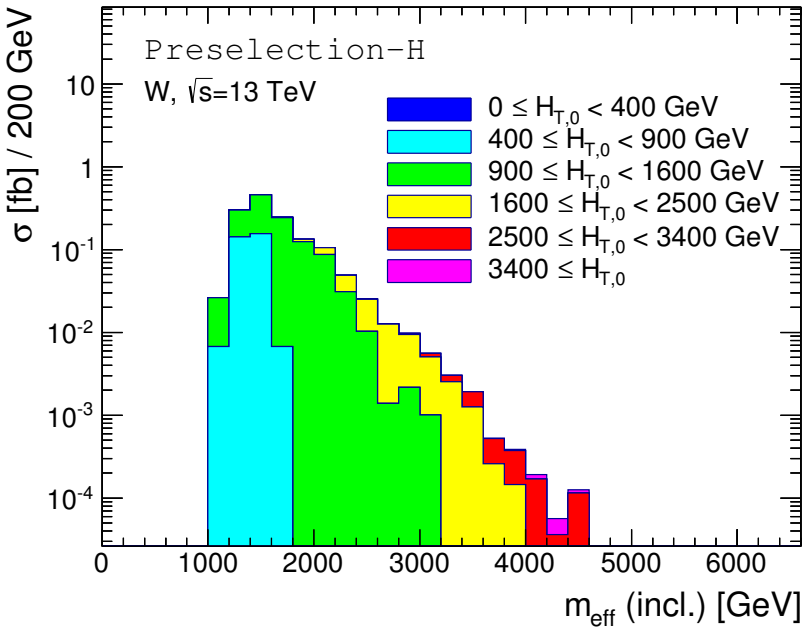

Figure 4.6: Same as Fig. 4.5 except contributions from processes with W boson are presented.

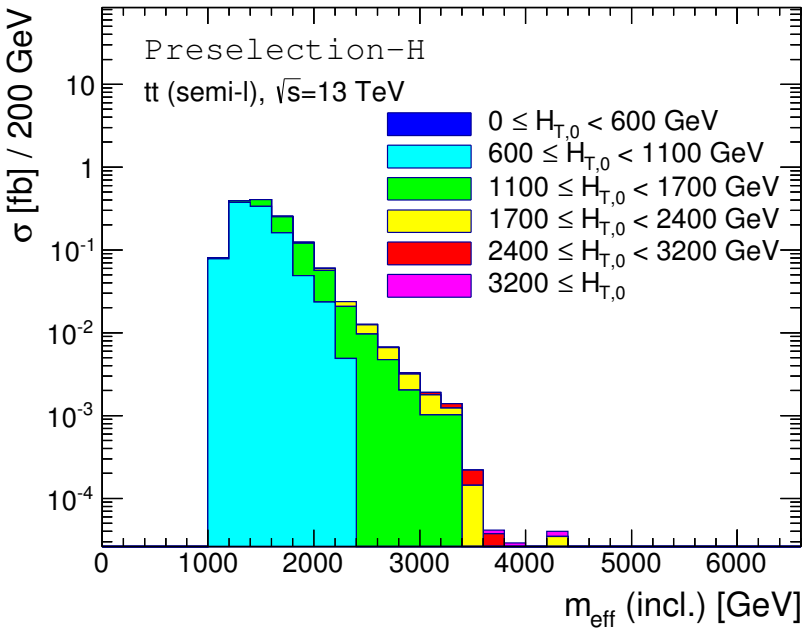

Figure 4.7: Same as Fig. 4.5 except contributions from processes with $t\bar{t}$ are presented. Semi-leptonic decays of $t\bar{t}$ are assumed.

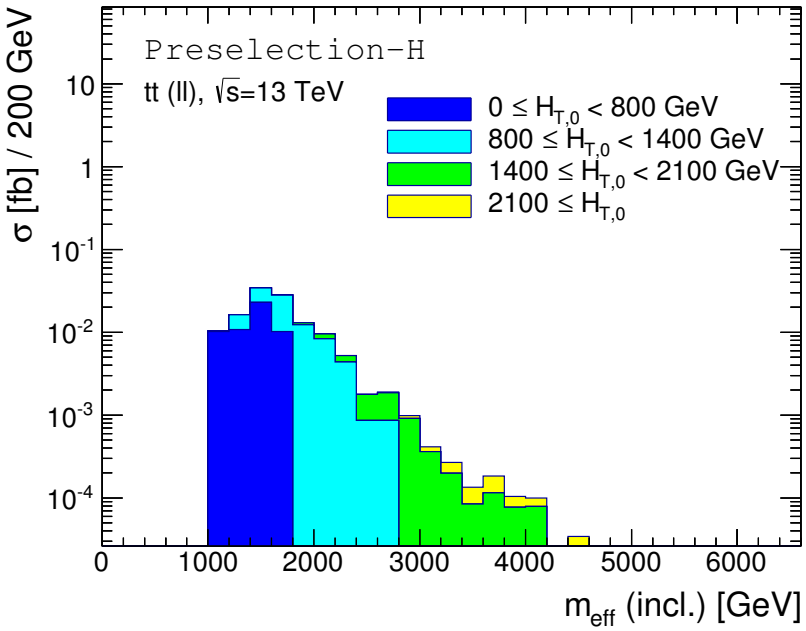

Figure 4.8: Same as Fig. 4.5 except contributions from processes with $t\bar{t}$ are presented. Leptonic decays of $t\bar{t}$ are assumed.

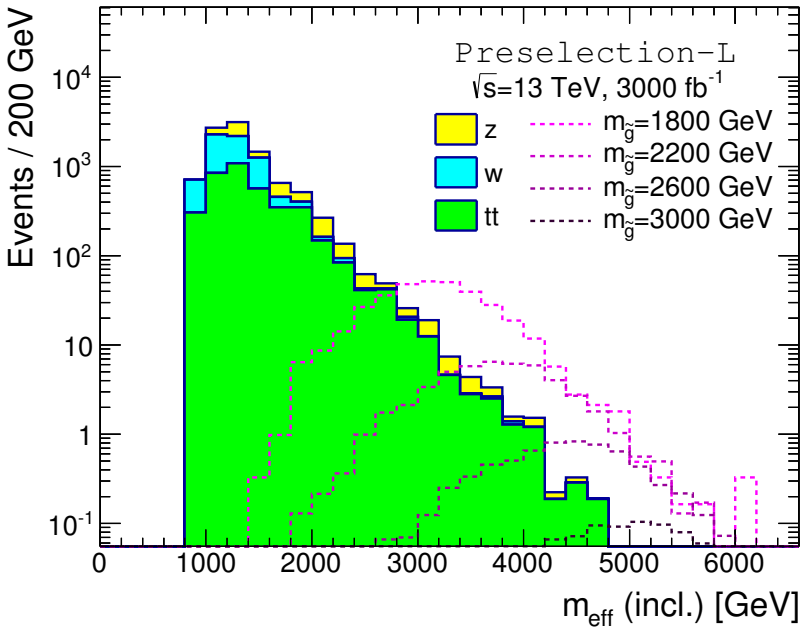

Figure 4.9: Distribution of $m_{\rm eff}$(incl.) after imposing `preselection-L` for the SM background processes and gluinos with various mass. The mass of LSP is set to be 100 GeV.

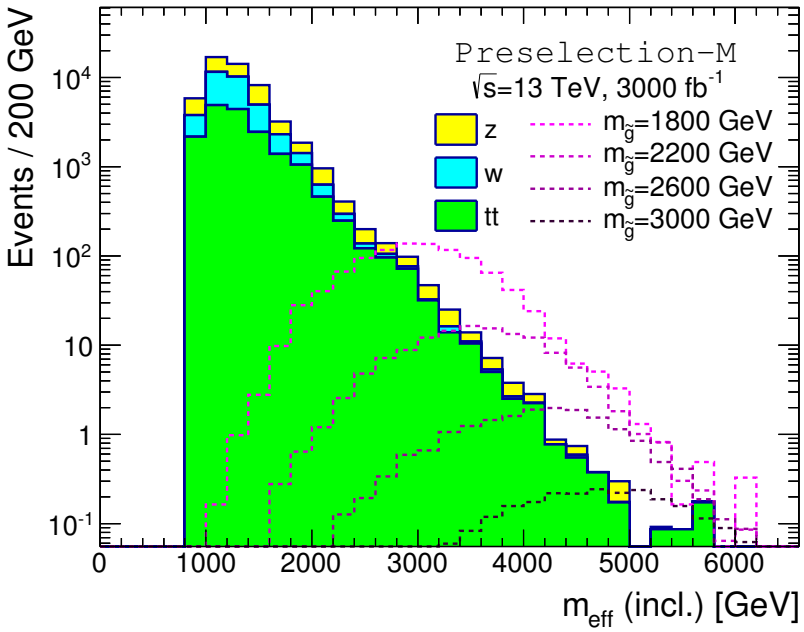

Figure 4.10: Same as Fig. 4.9 except `preselection-M` is imposed.

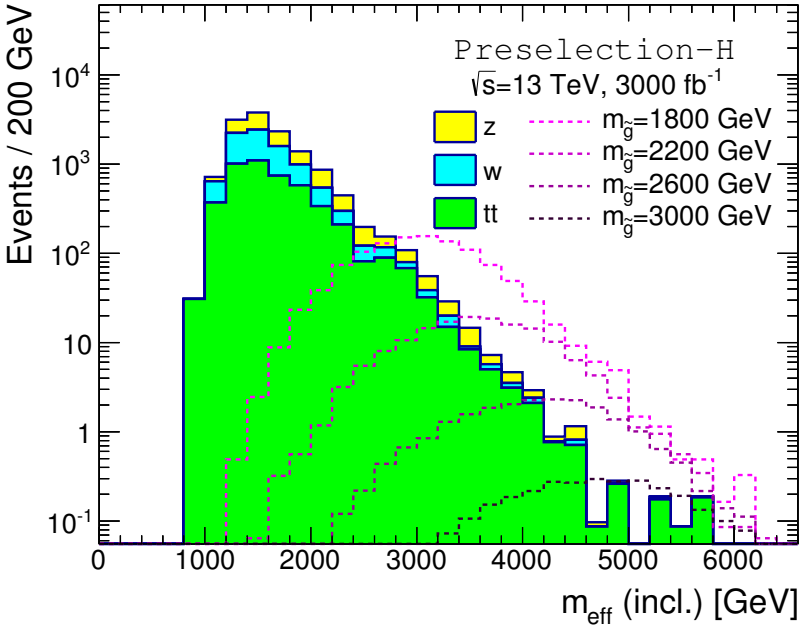

Figure 4.11: Same as Fig. 4.9 except `preselection-H` is imposed.

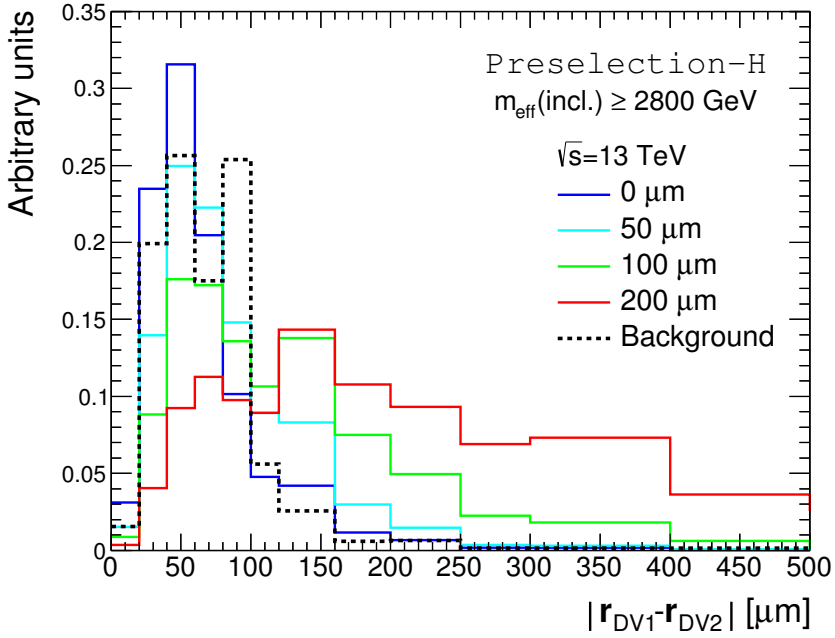

Figure 4.12: $|\boldsymbol{r}_{\mathrm{DV1}} - \boldsymbol{r}_{\mathrm{DV2}}|$ distribution of signal events (solid) and the SM background events (dashed). For signal events, we assume gluinos with mass of 3 TeV and several values of $c\tau_{\tilde{g}}$. In these distributions, `preselection-H` and requirement of $m_{\mathrm{eff}}(\mathrm{incl.}) > 2800$ GeV are imposed.

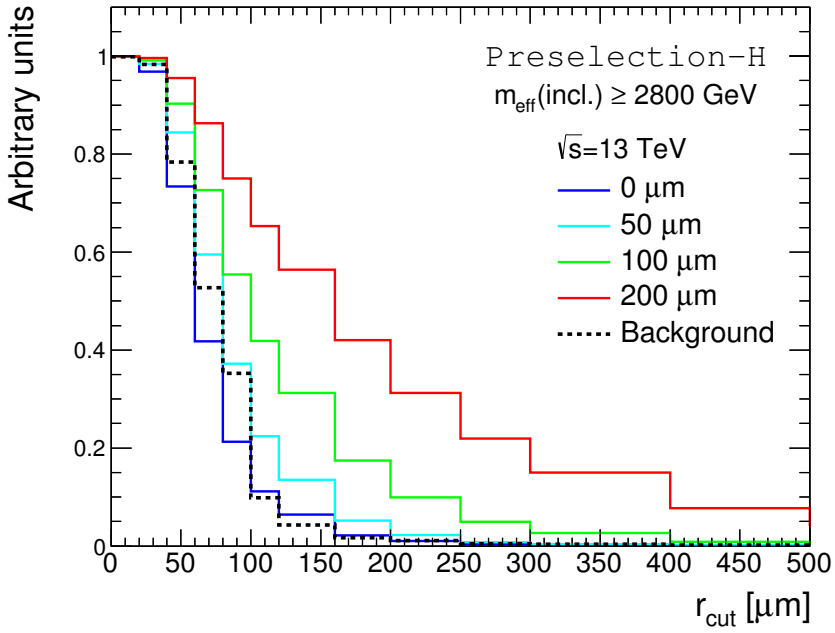

Figure 4.13: A fraction of events passing a selection cut of $|\boldsymbol{r}_{\mathrm{DV1}} - \boldsymbol{r}_{\mathrm{DV2}}| > r_{\mathrm{cut}}$. For signal events, we assume gluinos with mass of 3 TeV and several values of $c\tau_{\tilde{g}}$. In these distributions, `preselection-H` and requirement of $m_{\mathrm{eff}}(\mathrm{incl.}) > 2800$ GeV are imposed.

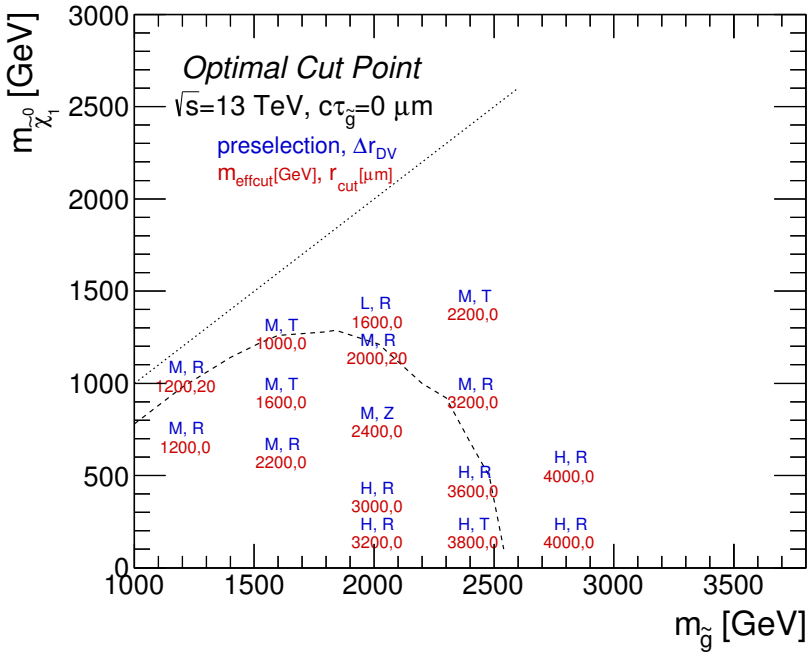

Figure 4.14: Optimal cut values ($(m_{\text{effcut}})_{\text{optimal}}$, $(r_{\text{cut}})_{\text{optimal}}$) for each sample point with $c\tau_{\tilde{g}} = 0$ μm, which maximize the expected significance Z_0 when the integrated luminosity of 3000 fb^{-1} is assumed. The preselection and the DV based observables which give the largest value of Z_0 are also presented. In the figure, R, T, and Z denote $|\boldsymbol{r}_{\text{DV1}} - \boldsymbol{r}_{\text{DV2}}|$, $|(\boldsymbol{r}_{\text{DV1}} - \boldsymbol{r}_{\text{DV2}})_{\text{T}}|$, and $|(\boldsymbol{r}_{\text{DV1}} - \boldsymbol{r}_{\text{DV2}})_z|$, respectively. The expected 5σ discovery reaches for gluinos are also presented in a dashed line.

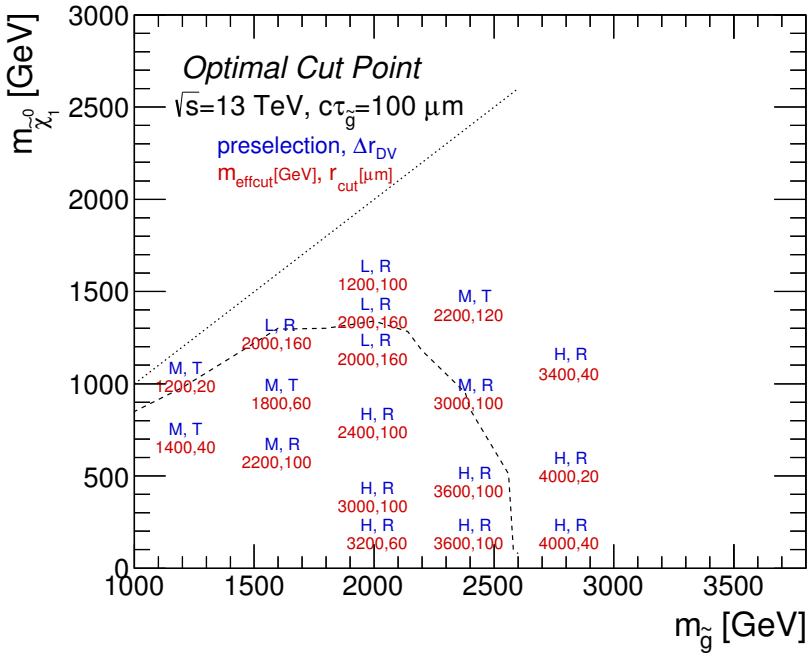

Figure 4.15: Same as Fig. 4.14 except $c\tau_{\tilde{g}} = 100$ μm.

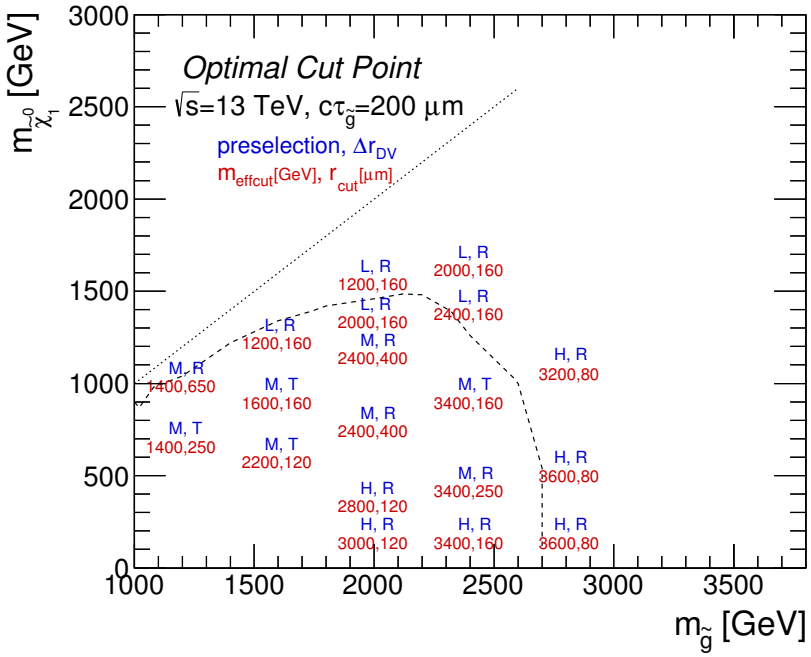

Figure 4.16: Same as Fig. 4.14 except $c\tau_{\tilde{g}} = 200$ μm.

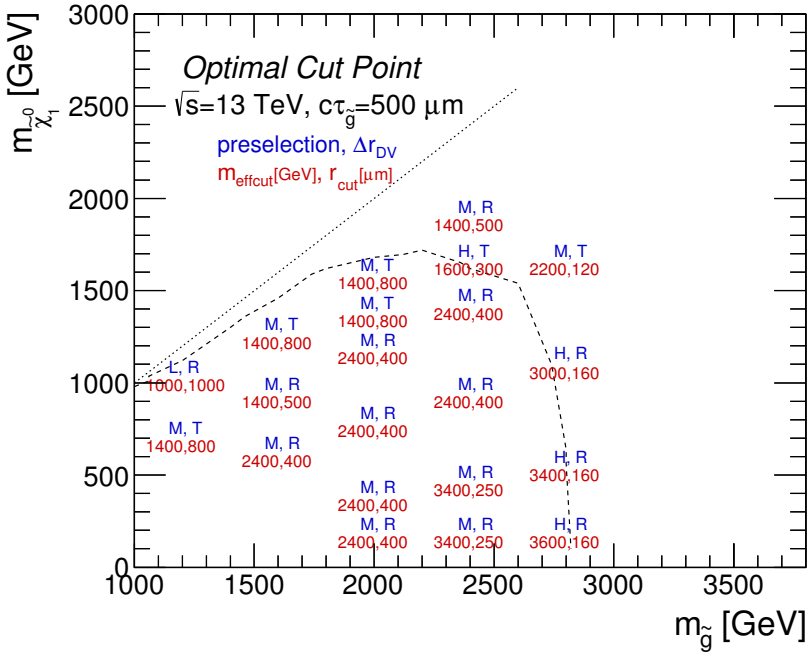

Figure 4.17: Same as Fig. 4.14 except $c\tau_{\tilde{g}} = 500$ μm.

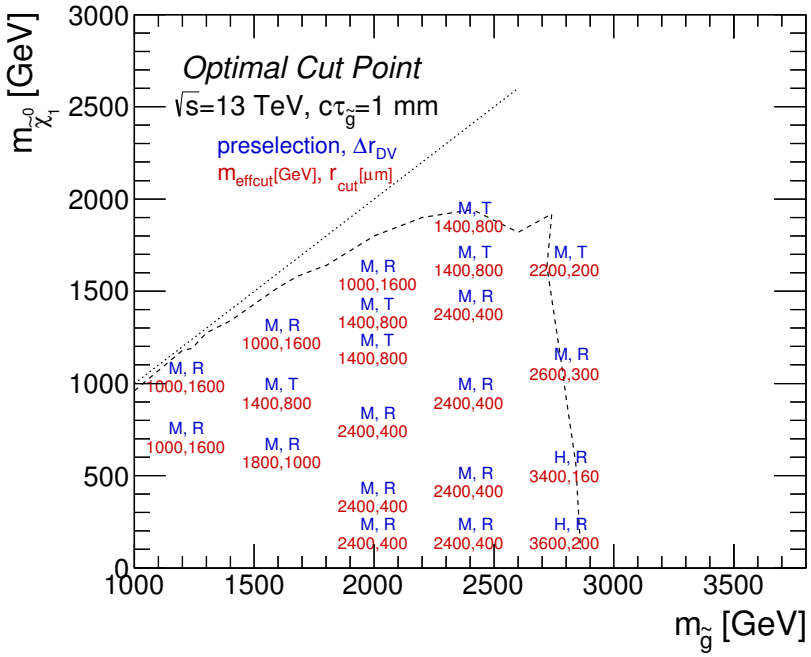

Figure 4.18: Same as Fig. 4.14 except $c\tau_{\tilde{g}} = 1$ mm.

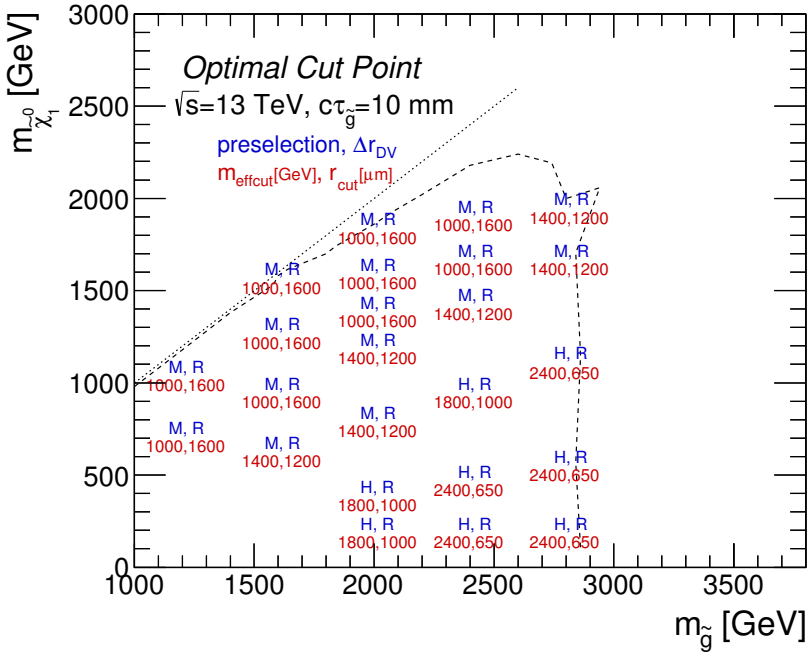

Figure 4.19: Same as Fig. 4.14 except $c\tau_{\tilde{g}} = 10$ mm.

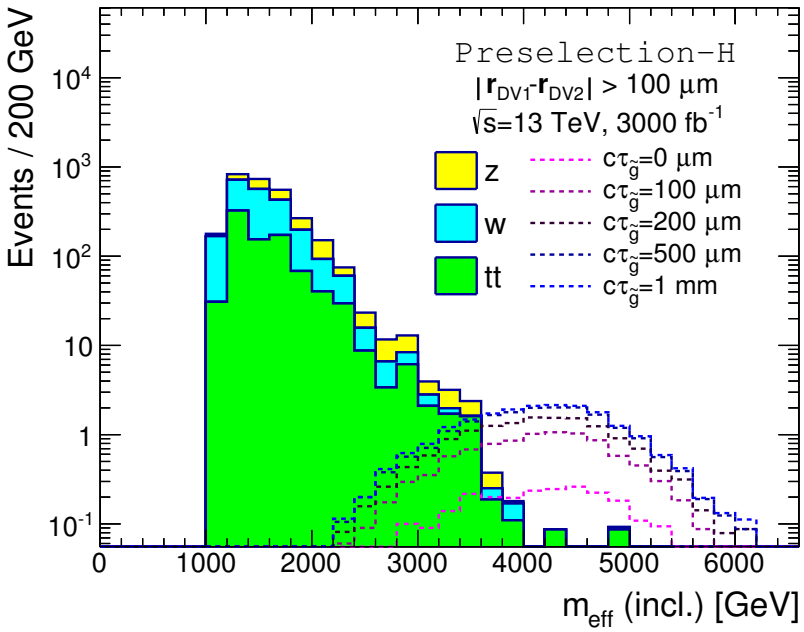

Figure 4.20: Distribution of m_{eff}(incl.) after imposing `preselection-H`, the vetos presented in Table 4.8, and $\left|\boldsymbol{r}_{\text{DV1}} - \boldsymbol{r}_{\text{DV2}}\right| > 100$ μm for the SM background processes and gluinos with various $c\tau_{\tilde{g}}$. The mass of gluinos and LSP are set to be 2600 GeV and 100 GeV respectively.

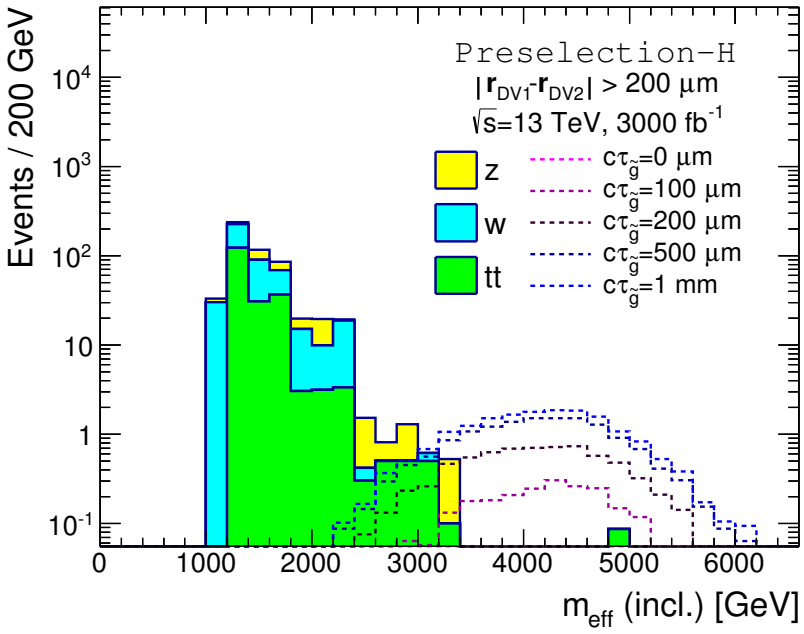

Figure 4.21: Same as Fig. 4.20 except $\left|\boldsymbol{r}_{\mathrm{DV1}} - \boldsymbol{r}_{\mathrm{DV2}}\right| > 200$ μm is required.

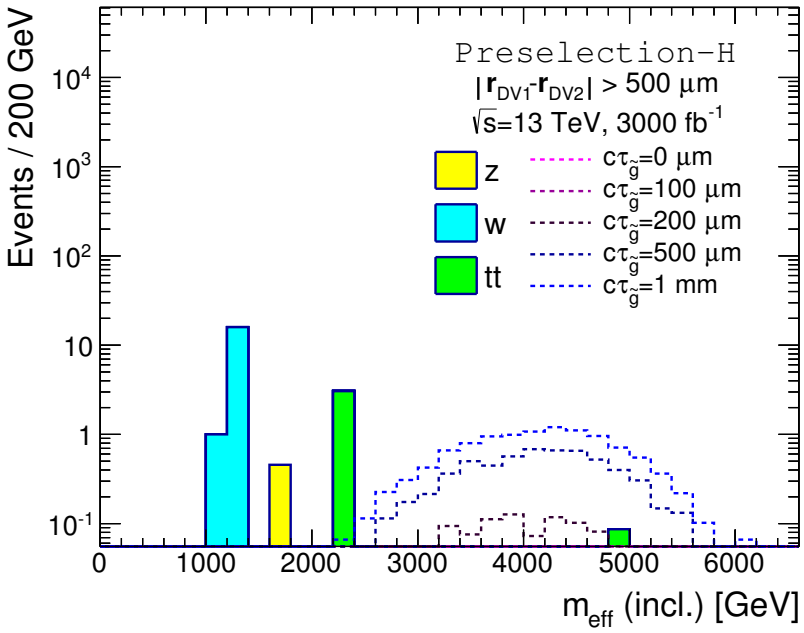

Figure 4.22: Same as Fig. 4.20 except $\left|\boldsymbol{r}_{\mathrm{DV1}} - \boldsymbol{r}_{\mathrm{DV2}}\right| > 500$ μm is required.

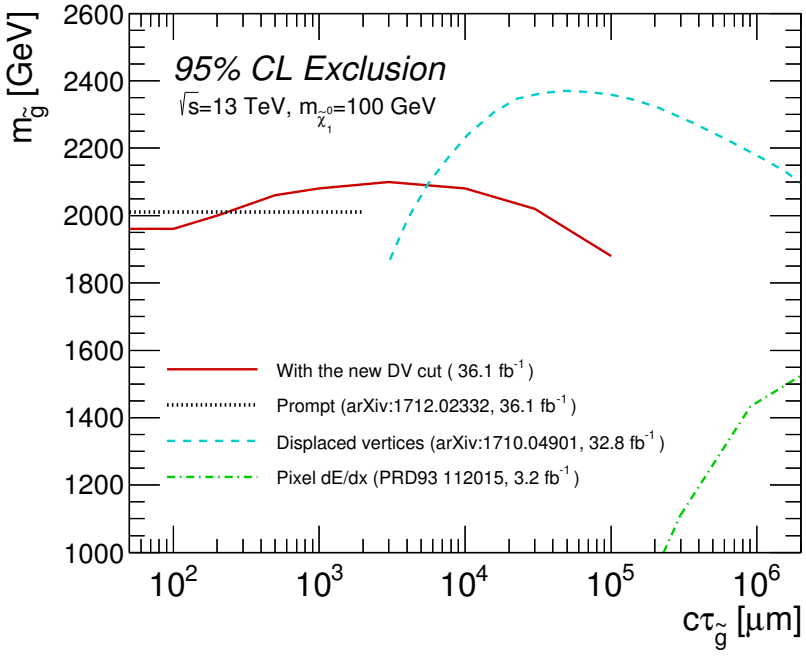

Figure 4.23: The 95% CL expected exclusion limits on the gluino mass with $\mathcal{L} = 36.1$ fb^{-1} at the 13 TeV LHC run as a function of $c\tau_{\tilde{g}}$ (red solid line). For comparison, we also show the 95% CL exclusion limits given by the ATLAS prompt-decay gluino search (black dotted line) [136], the ATLAS DV search (blue dashed line) [32], and the ATLAS search of large ionization energy loss in the Pixel detector (green dot-dashed line) [137].

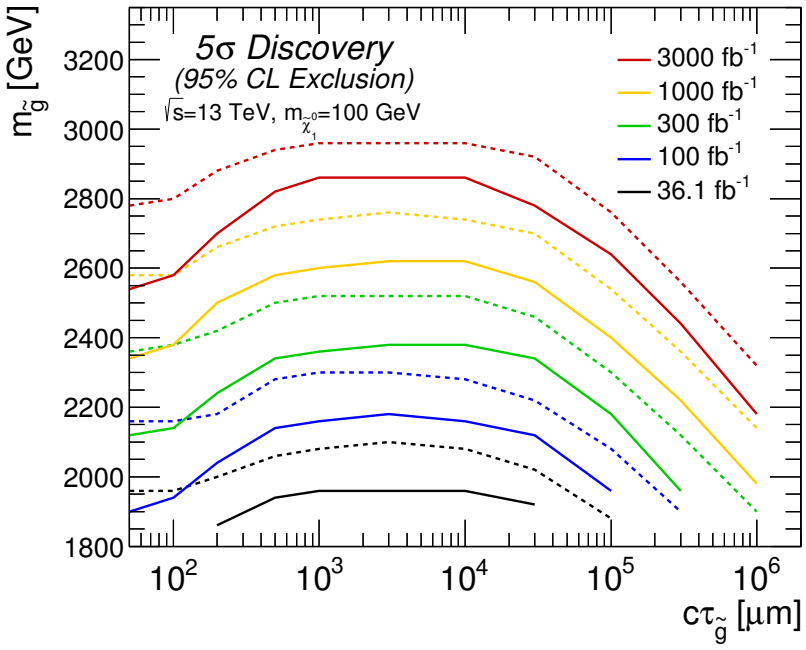

Figure 4.24: The expected 95% CL exclusion limits (dotted) and 5σ discovery reaches (solid) as functions of $c\tau_{\tilde{g}}$ for different values of integrated luminosity at the 13 TeV LHC run. The mass of LSP is set to be 100 GeV.

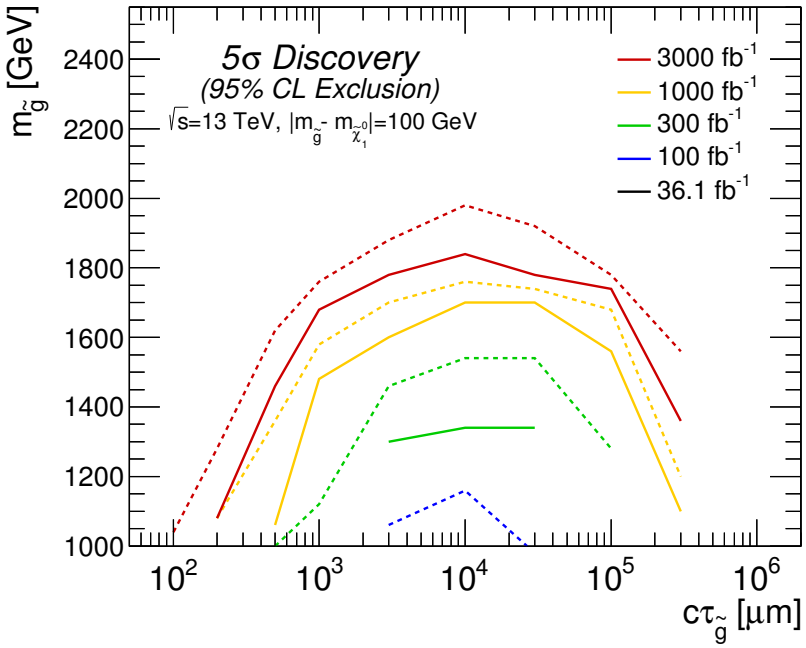

Figure 4.25: The expected 95% CL exclusion limits (dotted) and 5σ discovery reaches (solid) as functions of $c\tau_{\tilde{g}}$ for different values of integrated luminosity at the 13 TeV LHC run. Now the mass difference between gluinos and the LSP is set to be 100 GeV.

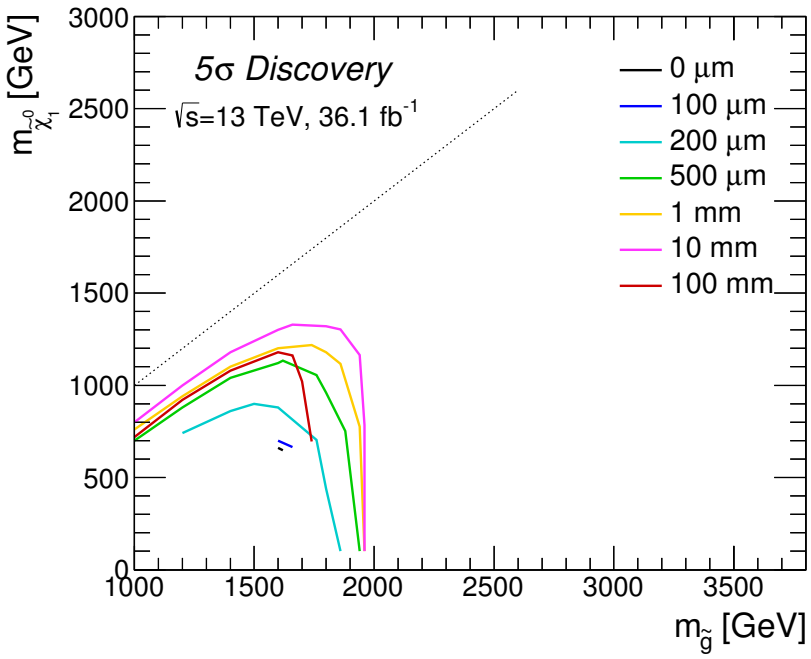

Figure 4.26: 5σ discovery reaches for gluinos with different $c\tau_{\tilde{g}}$ in terms of the gluino and the LSP masses. The integrated luminosity of 36.1 fb^{-1} is assumed.

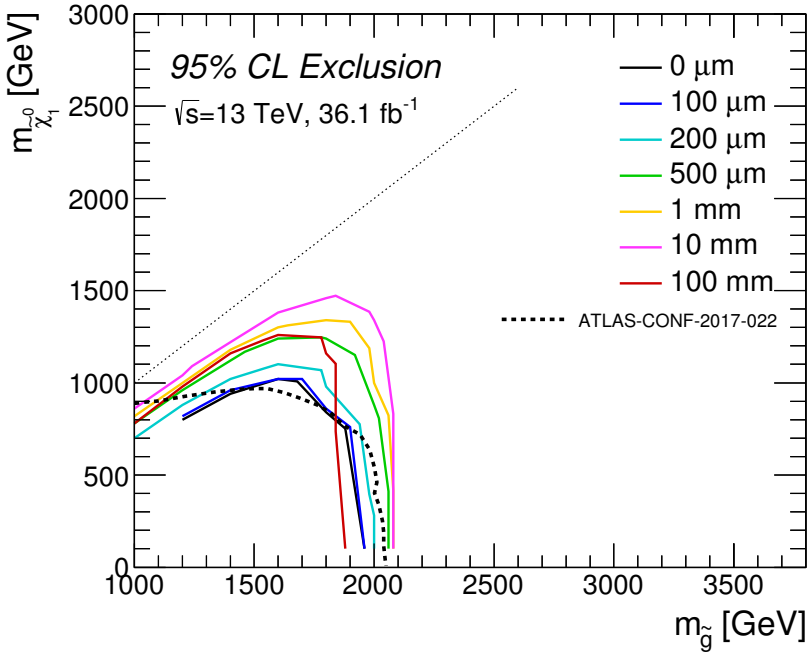

Figure 4.27: Expected 95% CL exclusion limits on gluino masses in terms of the gluino and the LSP masses. Several values of $c\tau_{\tilde{g}}$ are assumed. The observed 95% CL exclusion limits given by the ATLAS promptly decaying gluino search [75] is also presented (black dotted line). The integrated luminosity of 36.1 fb^{-1} is assumed.

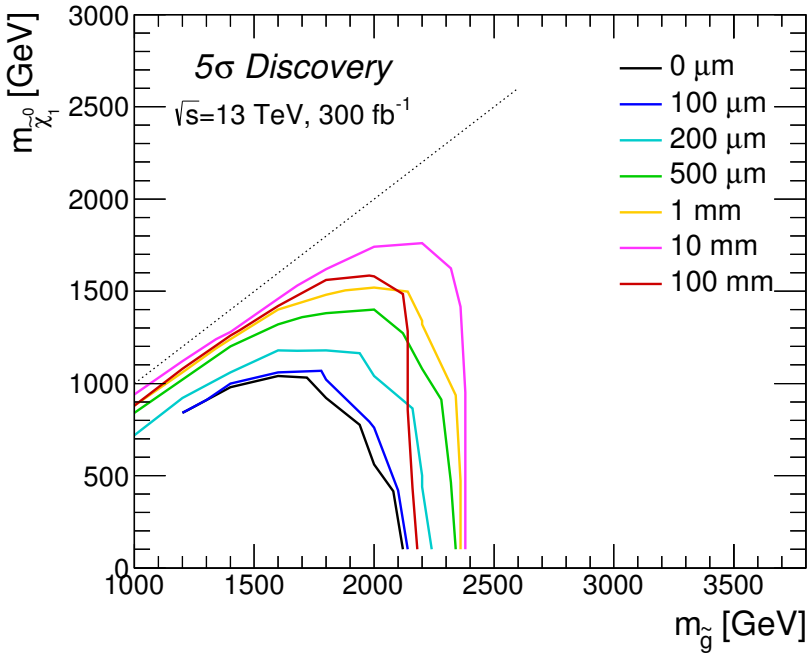

Figure 4.28: Same as Fig. 4.26 except the integrated luminosity of $300\,\mathrm{fb}^{-1}$ is assumed.

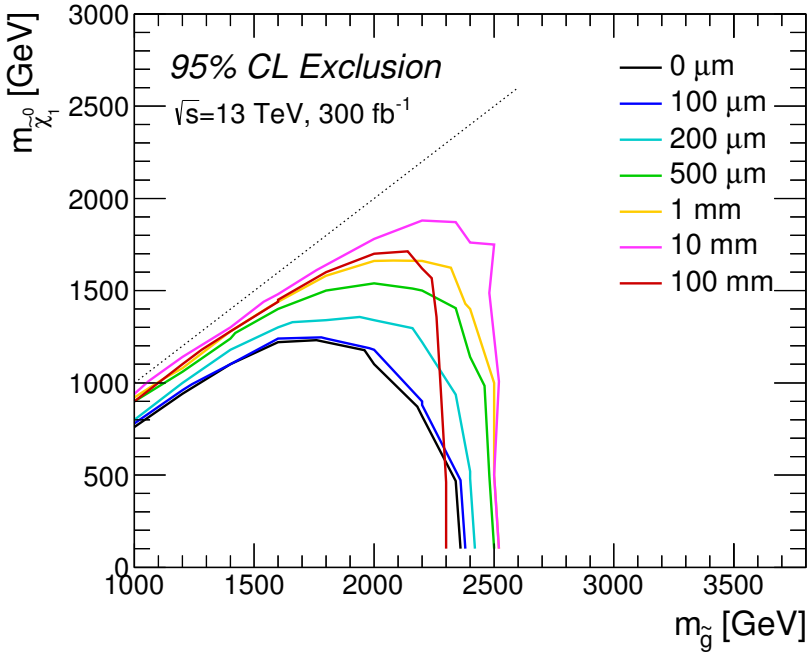

Figure 4.29: Same as Fig. 4.27 except the integrated luminosity of $300\,\mathrm{fb}^{-1}$ is assumed.

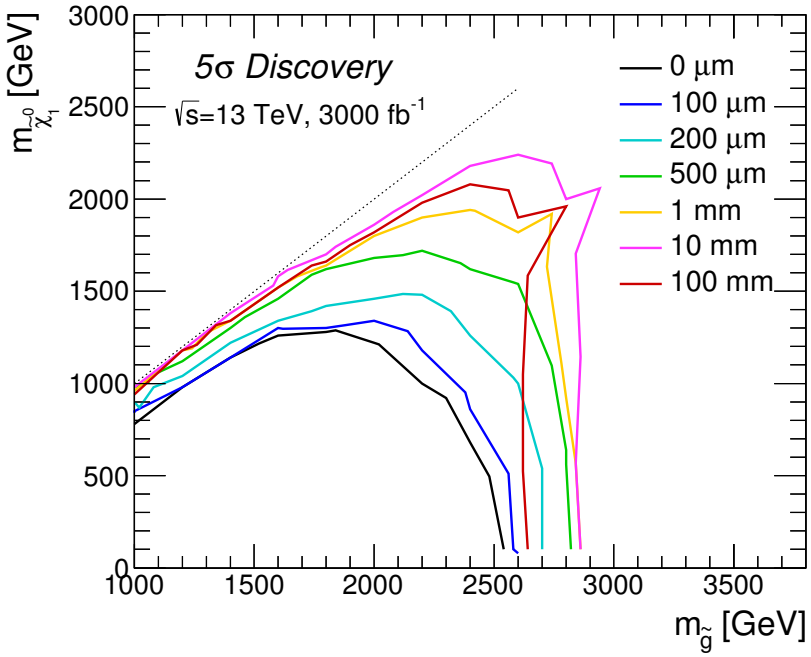

Figure 4.30: Same as Fig. 4.26 except the integrated luminosity of 3000 fb^{-1} is assumed.

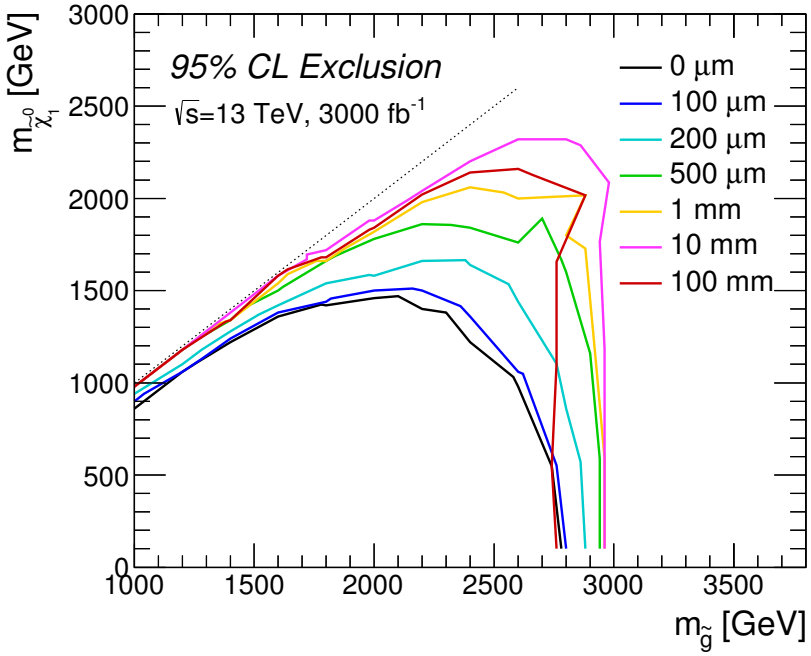

Figure 4.31: Same as Fig. 4.27 except the integrated luminosity of 3000 fb^{-1} is assumed.

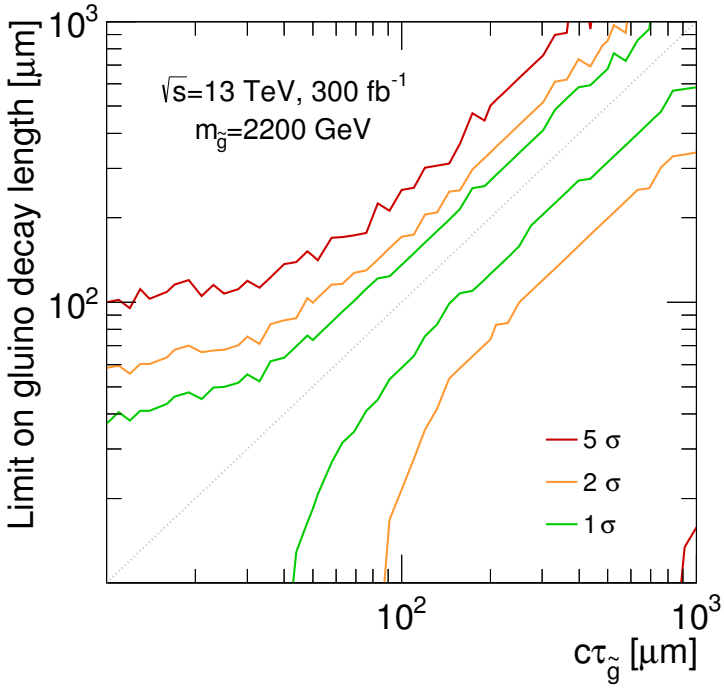

(a) $\mathcal{L} = 300\,\mathrm{fb}^{-1}$

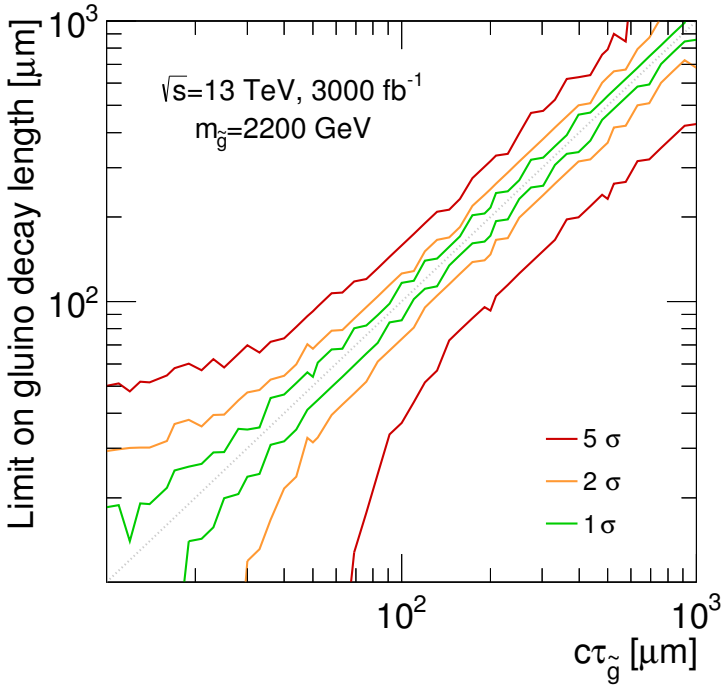

(b) $\mathcal{L} = 3000\,\mathrm{fb}^{-1}$

Figure 4.32: The expected upper and lower bounds on the decay length of gluino as a function of the underlying value of $c\tau_{\tilde{g}}$. Here, we set $m_{\tilde{g}} = 2.2$ TeV. `preselection-H` and a selection cut $m_{\mathrm{eff}}(\mathrm{incl.}) > 3500$ GeV are imposed.

Chapter 5

DV Search at a Future 100 TeV pp Collider

Physics at a future 100 TeV pp collider has been discussed [178, 179]. In this chapter, we try to apply the DV reconstruction methods discussed in Chapter 4 to searches for metastable gluinos at a future 100 TeV pp collider. As we have already seen in Chapter 2.3, the production cross section of gluinos is enhanced significantly at a 100 TeV pp collider compared to at the LHC. Therefore we expect that the reach of searches for metastable gluinos at a 100 TeV pp collider is extended drastically. Note that there is another appealing point to searches for metastable particles. At a 100 TeV pp collider, particles tend to be produced more energetically. This leads to the production of highly boosted metastable particles. It is the well-known fact that highly boosted particles live longer than particles at rest. Therefore we expect that metastable particles with shorter decay length can be probed with the DV reconstruction method we discussed in Chapter 4.

Since this is the first study of searches for metastable particles with DV reconstruction at a 100 TeV pp collider, we simply apply the procedure of DV reconstruction, the technique of generation of MC event samples, and event selection requirements which are all devised for the LHC study to the present 100 TeV pp collider case with minor modification. Therefore in this chapter, we mainly present points where modifications are made.

5.1 MC Simulation

MC simulation is used in the same way as is done in Chapter 4. For signal processes, sample points are summarized in Table 5.1. For background processes, we consider events in the dominant production processes of EW gauge boson (Z and W) and $t\bar{t}$ according to Ref. [177]. Since we are concerned about events with large missing energy, events with fully hadronic decays are ignored. Due to the limitation of our available computational resources, we approximate all processes with calculation up to three (for Z and W production) and one (for $t\bar{t}$ production) additional partons respectively. Background samples with different number of additional partons are matched in the same way as is

$m_{\tilde{g}}$	3, 4, ... 6, 8, ... 16, 18 TeV
$m_{\tilde{\chi}_1^0}$	100 GeV, $(0.2, 0.4, 0.6, 0.8) \times m_{\tilde{g}}$, $m_{\tilde{g}} - (150\,\text{GeV}, 100\,\text{GeV}, 50\,\text{GeV}, 25\,\text{GeV})$
$c\tau_{\tilde{g}}$	0, 50, 100, 200, 500, 1000, 3000 μm, 1×10^4, 3×10^4, 1×10^5, 3×10^5, 1×10^6 μm

Table 5.1: Sample points for signal in parameter space. We generate 50,000 events for each sample point. Note that for $m_{\tilde{g}} = 18$ TeV, we only generate samples with $m_{\tilde{\chi}_1^0} = 100$ GeV since others are not our main concern.

done in Chapter 4. In the generation of background samples, the generator-level phase space is divided according to $H_{T,0}$ ($\equiv \sum_{\text{partons}} p_{\text{T}}$). In Tables 5.2–5.4, we present upper edge values of bin α ($\equiv H_{T,0}^{\max}(\alpha)$), the cross section before matching $\sigma_{\text{no-mattching}}(\alpha)$, the number of MC samples we generate ($N_{\text{gen}}(\alpha)$), and equivalent luminosity ($\mathcal{L}_{\text{gen}} \equiv N_{\text{gen}}(\alpha)/\sigma_{\text{no-mattching}}(\alpha)$). In Figs. 5.1–5.4, we present distributions of m_{eff}(incl.) obtained by our MC simulation. Here the preselection requirement `Preselection-H` defined in Table 4.6 is imposed. A relatively good correspondence between $H_{T,0}$ and m_{eff}(incl.) can be seen. For reconstructed objects such as jets, charged leptons, and charged tracks, the same definitions as in Chapter 4 are adopted.

To validate our MC simulation, we compare the expected event number obtained by our MC simulation with the one given in Ref. [177], imposing the same selection cuts adopted in Ref. [177]. In most of the signal regions, they are consistent to within 20%.

5.2 Event Selection

For the search at a 100 TeV pp collider, we adopt the same strategy for background reduction as the one employed in Chapter 4; we first reduce background drastically by applying kinematical selection cuts, then we further impose the new selection cuts based on DV reconstruction.

As preselections, we study the same preselections given in Table 4.6, though we expect they may be optimized further. Among them, a preselection which can set the most stringent limit on gluino mass is adopted for each sample point. Lepton and detector material veto are also imposed. Here we assume the ATLAS detector. Therefore the same track-resolution parameters presented in Table 4.7 are also used in the current analysis. In Figs. 5.5–5.7, we present the m_{eff}(incl.) distribution after imposing `preselection-L, M, H` for the SM backgrounds and gluinos with various mass.

	bin α	0	1	2	3	4
$H_{T,0}^{\max}(\alpha)$	(GeV)	900	2100	4000	6400	∞
$\sigma_{\text{no-mattching}}(\alpha)$	(pb)	1.22×10^{3}	91.4	8.56	0.911	0.166
$N_{\text{gen}}(\alpha)$	($\times10^3$)	2400	1840	1720	1840	2400
$\mathcal{L}_{\text{gen}}(\alpha)$	(ab^{-1})	1.97×10^{-3}	0.0201	0.201	2.02	14.5

(a) $Z \to \nu\bar{\nu} + 0, 1, 2, 3\, j$.

	bin α	0	1	2	3	4
$H_{T,0}^{\max}(\alpha)$	(GeV)	900	2100	4000	6400	∞
$\sigma_{\text{no-mattching}}(\alpha)$	(pb)	2.97×10^{3}	73.8	6.16	0.605	0.102
$N_{\text{gen}}(\alpha)$	($\times10^3$)	300	300	300	300	300
$\mathcal{L}_{\text{gen}}(\alpha)$	(ab^{-1})	1.01×10^{-4}	4.06×10^{-3}	0.0487	0.496	2.95

(b) $Z \to l\bar{l} + 0, 1, 2, 3\, j$.

Table 5.2: The upper edge value of $H_{T,0}$ ($H_{T,0}^{\max}(\alpha)$), cross section before matching ($\sigma_{\text{no-mattching}}$), the number of generated events (N_{gen}), and equivalent luminosity $\mathcal{L}_{\text{gen}}$ for each $H_{T,0}$ bin. For the definition of $H_{T,0}$ and $\mathcal{L}_{\text{gen}}$, see the text. Here values for processes with Z production are presented.

	bin α	0	1	2	3	4	5
$H_{T,0}^{\max}(\alpha)$	(GeV)	600	1500	3000	5000	7500	∞
$\sigma_{\text{no-mattching}}(\alpha)$	(pb)	2.32×10^{4}	1.63×10^{3}	1.44×10^{2}	14.5	1.86	0.379
$N_{\text{gen}}(\alpha)$	($\times10^3$)	4600	3200	2800	2800	3800	7800
$\mathcal{L}_{\text{gen}}(\alpha)$	(ab^{-1})	1.99×10^{-4}	1.97×10^{-3}	0.0195	0.193	2.05	20.6

Table 5.3: Same as Table 5.2 except values for processes with W production are presented. Here we consider only processes with leptonic decay of W boson. Up to three additional partons are taken into account ($W \to l\nu + 0, 1, 2, 3\, j$).

	bin α	0	1	2	3	4	5	6
$H_{T,0}^{\rm max}(\alpha)$	(GeV)	800	1600	2800	4600	7200	10000	∞
$\sigma_{\rm no-mattch}(\alpha)$	(pb)	6.56×10^{3}	4.73×10^{2}	42.4	4.17	0.406	0.0359	6.10×10^{-3}
$N_{\rm gen}(\alpha)$	($\times10^3$)	80	80	80	80	80	80	80
$\mathcal{L}_{\rm gen}(\alpha)$	(ab^{-1})	1.22×10^{-5}	1.69×10^{-4}	1.89×10^{-3}	0.0192	0.197	2.23	13.1

(a) $t\bar{t} \to$ (semi-leptonic)+$0, 1j$.

	bin α	0	1	2	3	4
$H_{T,0}^{\rm max}(\alpha)$	(GeV)	1100	2300	3900	6000	∞
$\sigma_{\rm no-mattching}(\alpha)$	(pb)	72.1	7.23	0.603	0.0589	7.30×10^{-3}
$N_{\rm gen}(\alpha)$	($\times10^3$)	80	80	80	80	80
$\mathcal{L}_{\rm gen}(\alpha)$	(ab^{-1})	1.11×10^{-3}	1.11×10^{-2}	0.133	1.36	11.0

(b) $t\bar{t} \to$ (leptonic)+$0, 1j$.

Table 5.4: Same as Table 5.2 except values for processes with $t\bar{t}$ production are presented. Here we consider only processes with semi-leptonic and leptonic decay of $t\bar{t}$. Up to one additional parton is taken into account.

As a DV based variable, we try three candidates,

$$\left|\boldsymbol{r}_{\rm DV1} - \boldsymbol{r}_{\rm DV2}\right|,\ \ \left|(\boldsymbol{r}_{\rm DV1} - \boldsymbol{r}_{\rm DV2})_{\rm T}\right|,\ \text{and}\ \ \left|(\boldsymbol{r}_{\rm DV1} - \boldsymbol{r}_{\rm DV2})_{z}\right|,$$

and adopt a one which realizes the best sensitivity for each sample point. In Fig. 5.8 (5.10), we show the $|\boldsymbol{r}_{\rm DV1} - \boldsymbol{r}_{\rm DV2}|$ distribution of signal events for a gluino with $m_{\tilde{g}} = 3$ (14) TeV and several values of $c\tau_{\tilde{g}}$. We also present the distribution for the SM background events. In these distributions, `preselection-H` and requirement of $m_{\rm eff}$(incl.) $>$ 2800 (17600) GeV are imposed. In Figs. 5.9 and 5.11, we plot a fraction of events passing a selection cut of $|\boldsymbol{r}_{\rm DV1} - \boldsymbol{r}_{\rm DV2}| > r_{\rm cut}$ as a function of $r_{\rm cut}$. The effect of Lorentz boost of metastable particles on DVs can be seen clearly by comparing Fig. 5.8 (5.9) with Fig. 4.12 (4.13). In Figs. 4.12 and 4.13, the difference between distributions for $c\tau_{\tilde{g}} = 0$ μm and $c\tau_{\tilde{g}} = 50$ μm is hardly discernible. On the other hand, for the 100 TeV pp collider case in Figs. 5.8 and 5.9, the distributions for $c\tau_{\tilde{g}} = 50$ μm clearly deviate from those for $c\tau_{\tilde{g}} = 0$ μm. These observations indicate that gluinos tend to be more boosted at 100 TeV pp colliders than at the LHC, hence flight over longer distance before they decay. On the other hand, such difference between $c\tau_{\tilde{g}} = 0$ μm and $c\tau_{\tilde{g}} = 50$ μm is less clear in Figs. 5.10 and 5.11 where $m_{\tilde{g}} = 14$ TeV. This reflects the fact that heavier particles are likely to be produced less boosted than light particles.

Selection	Requirments
Preselection	$\in$ (`preslection-L, M, H`)
Lepton veto	No reconstructed electrons and muons
Material veto	No DVs are reconstructed in the detector material regions; *i.e.* (in a unit of mm) $\lvert(\boldsymbol{r}_{\rm DV})_{\rm T}\rvert \notin (22,25), (29,38), (46,73), (84,111), (120,\infty)$
$m_{\rm eff}$(incl.) cut	Require $m_{\rm eff}(\text{incl.}) > (m_{\rm effcut})_{\rm optimal}$ over $m_{\rm effcut} \in (1000\ \text{GeV}, 3\times10^4\ \text{GeV})$
$\Delta r_{\rm DV}$ cut	Require $\Delta r_{\rm DV} > (r_{\rm cut})_{\rm optimal}$ over $\Delta r_{\rm DV} \in (\lvert\Delta\boldsymbol{r}_{\rm DV}\rvert, \lvert(\Delta\boldsymbol{r}_{\rm DV})_{\rm T}\rvert, \lvert(\Delta\boldsymbol{r}_{\rm DV})_{\rm z}\rvert)$ $r_{\rm cut} \in (0, 2\times10^5 \mu\text{m})$

Table 5.5: A summary of selections we imposed in the study of the search for metastable gluinos at a 100 TeV *pp* collider. Here we abbreviate $(\boldsymbol{r}_{\rm DV1} - \boldsymbol{r}_{\rm DV2})$ as $\Delta\boldsymbol{r}_{\rm DV}$.

5.3 Expected Reach at a Future 100 TeV *pp* Collider

Next we are going to present the performance of the new selection cut based on DVs by showing how far we can extend the discovery reach and exclusion limit in a search for metastable gluinos at a future 100 TeV *pp* collider.

As we did in Chapter 4, after applying one of the `preselection-L,M,H`, we further require events to satisfy

$$m_{\rm eff}(\text{incl.}) > (m_{\rm effcut})_{\rm optimal}\,,\ \Delta r_{\rm DV} > (r_{\rm cut})_{\rm optimal}\ ,$$

where $\Delta r_{\rm DV}$ is one of the DV based observables;

$$\left|\boldsymbol{r}_{\rm DV1} - \boldsymbol{r}_{\rm DV2}\right|,\ \left|(\boldsymbol{r}_{\rm DV1} - \boldsymbol{r}_{\rm DV2})_{\rm T}\right|,\ \text{or}\ \left|(\boldsymbol{r}_{\rm DV1} - \boldsymbol{r}_{\rm DV2})_{z}\right|.$$

Among them, the ones which realize the best sensitivity are adopted for each sample point. We vary the cut parameters $m_{\rm effcut}$ and $r_{\rm cut}$ from 1000 GeV to 3×10^4 GeV and from 0 to 2×10^5 μm respectively, and adopt the values which optimize the results. We present a summary of selections we impose on events in Table 5.5. For exclusion limits, we compute the expected 95% confidence level (CL) limits on the gluino mass using the CL_s prescription [174]. For expected 5σ discovery reach, both the expected significance of discovery Z_0 given by Eq. (4.9) and the expected number of signal events larger than 5 are required. In Figs. 5.12–5.17, we present optimal cut values ($(m_{\rm effcut})_{\rm optimal}$, $(r_{\rm cut})_{\rm optimal}$

	Z	W	$t\bar{t}$	total
`preselection-H` ($\times 10^6$)	0.42 $\pm$0.01	0.45 $\pm$0.02	1.26 $\pm$0.4	2.13 $\pm$0.4
$m_{\rm eff}$(incl.) > 17.8 TeV	3.1 $\pm$0.8	0.9 $\pm$0.3	0.5 $\pm$0.4	4.6 $\pm$0.9
$\left\|\boldsymbol{r}_{\rm DV1} - \boldsymbol{r}_{\rm DV2}\right\| > 100$ μm	< 0.1	< 0.1	< 0.1	< 0.1
$\left\|\boldsymbol{r}_{\rm DV1} - \boldsymbol{r}_{\rm DV2}\right\| > 200$ μm	< 0.1	< 0.1	< 0.1	< 0.1

(a) The expected number of background events.

	$c\tau_{\tilde{g}} = 0$	$c\tau_{\tilde{g}} = 200$ μm	$c\tau_{\tilde{g}} = 500$ μm	$c\tau_{\tilde{g}} = 1$ mm
`preselection-H`	20.5 $\pm$0.3			
$m_{\rm eff}$(incl.) > 17.8 TeV	14.5 $\pm$0.2			
$\left\|\boldsymbol{r}_{\rm DV1} - \boldsymbol{r}_{\rm DV2}\right\| > 100$ μm	0.5 $\pm$0.04	9.8 $\pm$0.2	12.5 $\pm$0.2	12.9 $\pm$0.2
$\left\|\boldsymbol{r}_{\rm DV1} - \boldsymbol{r}_{\rm DV2}\right\| > 200$ μm	< 0.1	5.5 $\pm$0.1	9.6 $\pm$0.2	11.3 $\pm$0.2

(b) The expected number of signal events for $m_{\tilde{g}} = 12$ TeV, $m_{\tilde{\chi}_1^0} = 100$ GeV, and several values of $c\tau_{\tilde{g}}$.

Table 5.6: The expected number of background (a) and signal (b) events after imposing selection cuts. Here the integrated luminosity of $\mathcal{L} = 3000$ fb^{-1} is assumed. Estimated statistical uncertainty of MC simulation is also presented. The masses of gluinos and the LSP are set to be 12 TeV and 100 GeV respectively.

) for each sample point with various $c\tau_{\tilde{g}}$. These values are obtained by requiring that they maximize the expected significance Z_0. Here the integrated luminosity of 3000 fb^{-1} is assumed. The preselection and the DV based observables which give the largest value of Z_0 are also presented. In Tables 5.6 and 5.7, the expected number of background and signal events after imposing selection cuts are presented. Here the integrated luminosity of $\mathcal{L} = 3000$ fb^{-1} is assumed. In Table 5.6 (5.7), we consider the massless LSP (moderately degenerate) case, where $m_{\tilde{g}} = 12$ (10) TeV and $m_{\tilde{\chi}_1^0} = 100$ GeV (8 TeV). In these tables, statistical uncertainty of MC simulation (ΔN), which is estimated as Eq. (4.10), is also presented. In Figs. 5.18–5.20, we present the distribution of $m_{\rm eff}$(incl.) after imposing `preselection-H`, the vetos presented in Table 5.5, and $\left|\boldsymbol{r}_{\rm DV1} - \boldsymbol{r}_{\rm DV2}\right| > 100$ (200, 500) μm for the SM background processes and gluinos with various $c\tau_{\tilde{g}}$. Here the mass of gluinos and LSP are set to be 14 TeV and 100 GeV respectively. In the following, we first consider the case in which LSP mass is set to be 100 GeV. Then we extend our analysis to the cases in which LSP is degenerate with gluinos.

In Fig. 5.21, we show the expected 95% CL exclusion limits (in dotted lines) and 5σ discovery reaches (in solid lines) for gluino as functions of $c\tau_{\tilde{g}}$ for different values of integrated luminosity at a 100 TeV pp collider. Note that the expected exclusion limit

	Z	W	$t\bar{t}$	total
`preselection-H` $(\times 10^6)$	0.42 $\pm$0.01	0.45 $\pm$0.02	1.26 $\pm$0.4	2.13 $\pm$0.4
$m_{\rm eff}$(incl.) > 6 TeV $(\times 10^3)$	2.2 $\pm$0.1	1.0 $\pm$0.1	0.8 $\pm$0.2	4.0 $\pm$0.3
$\left\|\boldsymbol{r}_{\rm DV1} - \boldsymbol{r}_{\rm DV2}\right\| > 200$ μm	5.9 $\pm$3	5.7 $\pm$2.	2.2 $\pm$2	14 $\pm$4
$\left\|\boldsymbol{r}_{\rm DV1} - \boldsymbol{r}_{\rm DV2}\right\| > 500$ μm	< 0.1	< 0.1	< 0.1	< 0.1

(a) The expected number of background events.

	$c\tau_{\tilde{g}} = 0$	$c\tau_{\tilde{g}} = 200$ μm	$c\tau_{\tilde{g}} = 500$ μm	$c\tau_{\tilde{g}} = 1$ mm
`preselection-H`	143 $\pm$2			
$m_{\rm eff}$(incl.) > 6 TeV	70 $\pm$1			
$\left\|\boldsymbol{r}_{\rm DV1} - \boldsymbol{r}_{\rm DV2}\right\| > 200$ μm	0.4 $\pm$0.1	26.5 $\pm$0.7	45.1 $\pm$0.9	53.5 $\pm$1
$\left\|\boldsymbol{r}_{\rm DV1} - \boldsymbol{r}_{\rm DV2}\right\| > 500$ μm	< 0.1	6.4 $\pm$0.3	22.8 $\pm$0.6	36.5 $\pm$0.8

(b) The expected number of signal events for $m_{\tilde{g}} = 10$ TeV, $m_{\tilde{\chi}_1^0} = 8$ TeV, and several values of $c\tau_{\tilde{g}}$.

Table 5.7: Same as Table. 5.6 except the masses of gluinos and the LSP are set to be 10 TeV and 8 TeV respectively.

(discovery reach) for $c\tau_{\tilde{g}} = 0$ is represented by a circle (a filled circle). The mass of LSP is set to be 100 GeV. As can be seen from the figure, the reach for the gluino can be extended with the help of the additional DV selection cut for $c\tau_{\tilde{g}} \gtrsim 100$ μm; for instance, for a gluino with $c\tau_{\tilde{g}} \sim \mathcal{O}$(1–10) mm, the expected discovery reach for the gluino mass can be extended by as large as ~ 1.4 TeV (1.8 TeV) with an integrated luminosity of $\mathcal{L} = 300\,{\rm fb}^{-1}$ ($3000\,{\rm fb}^{-1}$). These reaches for a gluino with $c\tau_{\tilde{g}} \sim \mathcal{O}$(1–10) mm are obtained by `preselection H` and $|\boldsymbol{r}_{\rm DV1} - \boldsymbol{r}_{\rm DV2}|$ ($|\boldsymbol{r}_{\rm DV1} - \boldsymbol{r}_{\rm DV2}|_{\rm T}$) with $(m_{\rm effcut})_{\rm optimal} = 10$ TeV (12.6 TeV) and $(r_{\rm cut})_{\rm optimal} \sim 120\,\mu$m ($160\,\mu$m) for $\mathcal{L} = 300\,{\rm fb}^{-1}$ ($3000\,{\rm fb}^{-1}$). Compared to a promptly decaying gluino, where $(m_{\rm effcut})_{\rm optimal} = 13.8$ TeV (17.8 TeV) respectively, the $m_{\rm eff}$(incl.) selection cut is loosened and the new DV cut plays an important role in background rejection.

Next we discuss the cases where gluino and the LSP are degenerate. In Figs. 5.22–5.24, we show the expected 95% CL exclusion limits (dotted lines) and 5σ discovery reaches (solid lines) for gluino as functions of $c\tau_{\tilde{g}}$ for different values of integrated luminosity at a 100 TeV pp collider. The expected exclusion limit (discovery reach) for $c\tau_{\tilde{g}} = 0$ is also represented by a circle (a filled circle). In these figures, the mass difference between gluinos and the LSP are set to be 100, 50, and 25 GeV, respectively. In Figs. 5.25–5.28, we present the expected 95% CL exclusion limits and 5σ discovery reaches in terms of the gluino and the LSP masses. Several values of $c\tau_{\tilde{g}}$ are assumed. From these figures,

it can be seen that use of the new DV cut leads to sizable improvement in the discovery reach and the exclusion limit when $c\tau_{\tilde{g}} \gtrsim 100\,\mu$m. As we already mentioned, the results for $c\tau_{\tilde{g}} = 0\ \mu$m (black solid lines) corresponds to results which would be obtained without introducing the new DV cut. The improvement is maximized for $c\tau_{\tilde{g}} \sim \mathcal{O}(1\text{–}10)$ mm and in cases where gluino and the LSP are degenerate. Note that corresponding improvements for $c\tau_{\tilde{g}} = 100\,\mu$m at the LHC are expected to be not so significant. (See Figs. 4.28–4.31.) This also shows that boosting metastable particles is helpful to searches for such particles.

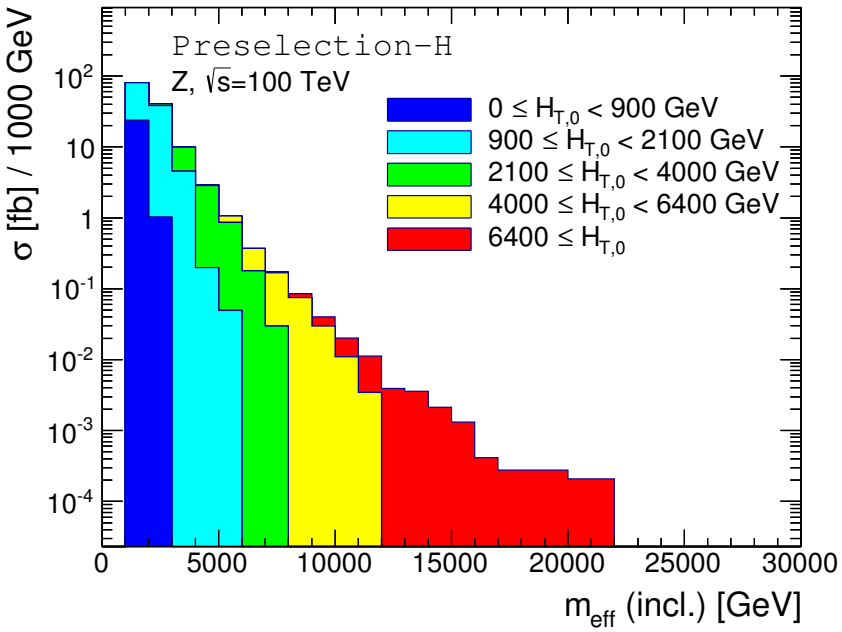

Figure 5.1: Distribution of m_{eff}(incl.) after imposing `preselection-H` defined in Table 4.6 for the SM background processes with Z boson. Contributions from MC samples in different $H_{T,0}$ bins are filled with different colors.

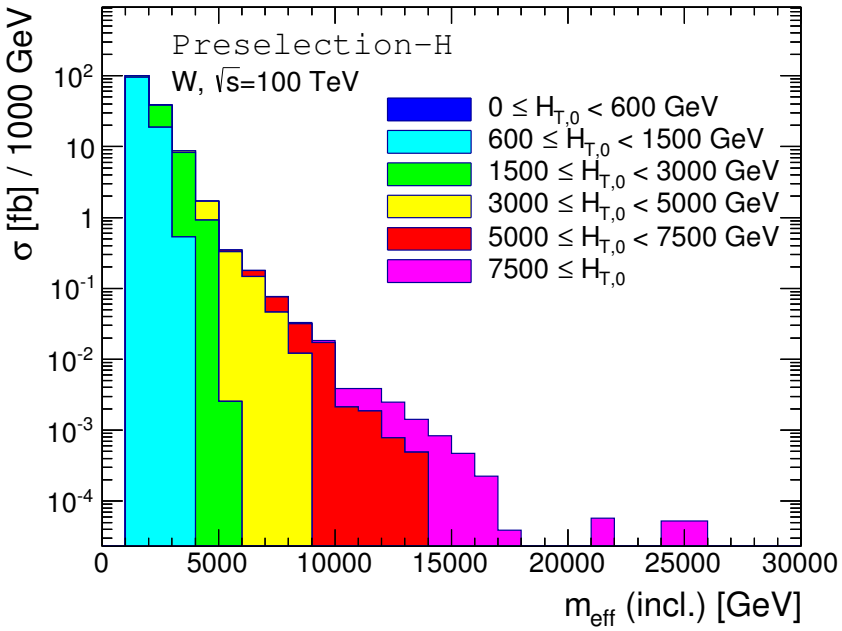

Figure 5.2: Same as Fig. 5.1 except contributions from processes with W boson are presented.

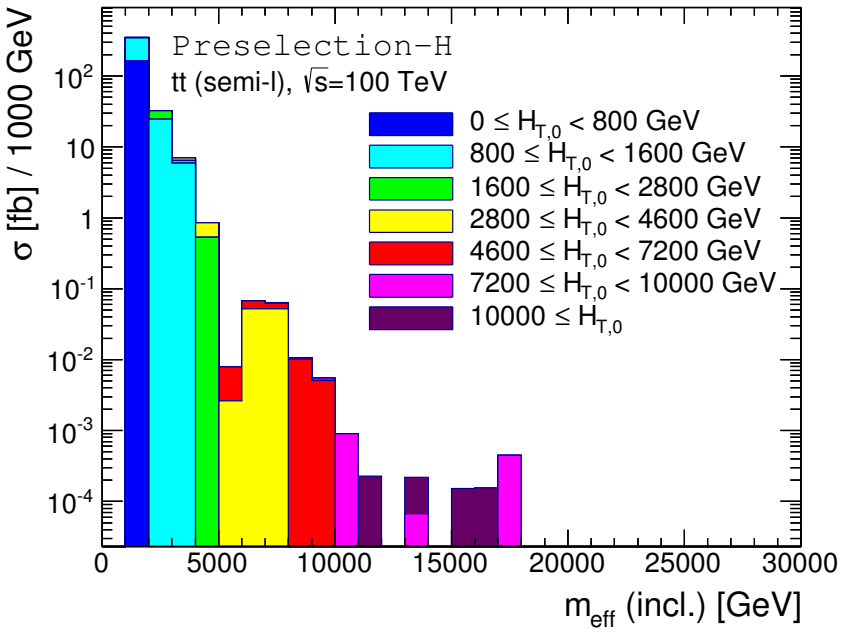

Figure 5.3: Same as Fig. 5.1 except contributions from processes with $t\bar{t}$ are presented. Semi-leptonic decays of $t\bar{t}$ are assumed.

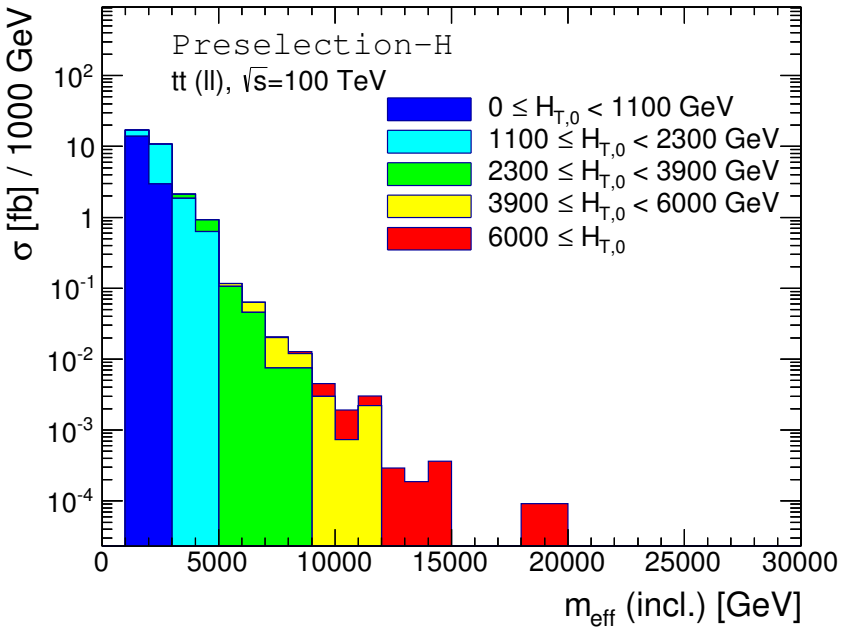

Figure 5.4: Same as Fig. 5.1 except contributions from processes with $t\bar{t}$ are presented. Leptonic decays of $t\bar{t}$ are assumed.

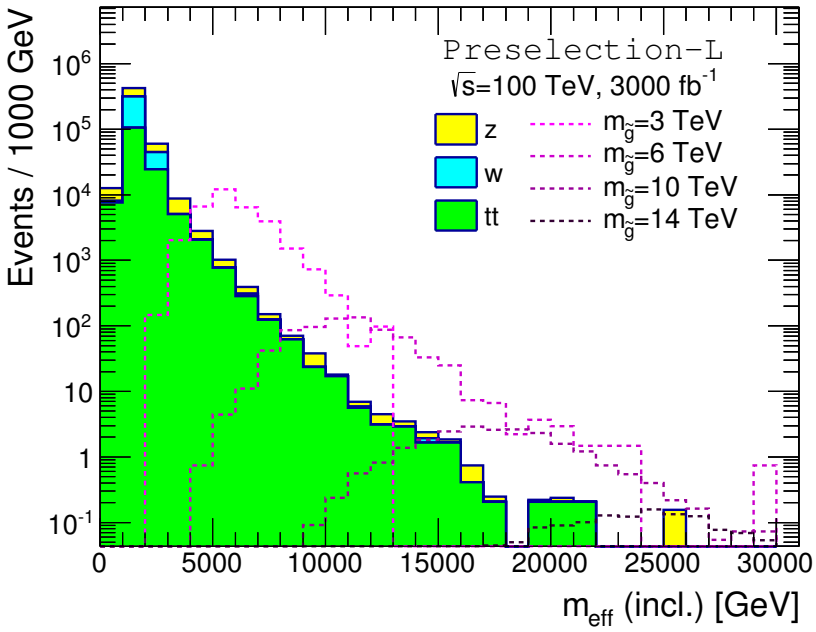

Figure 5.5: Distribution of $m_{\rm eff}$(incl.) after imposing `preselection-L` for the SM background processes and gluinos with various mass. The mass of LSP is set to be 100 GeV.

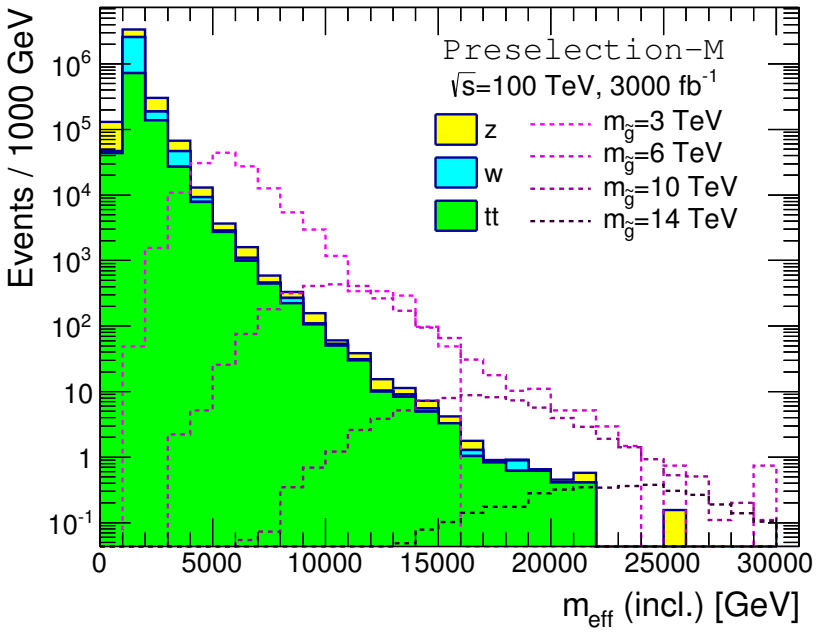

Figure 5.6: Same as Fig. 5.5 except `preselection-M` is imposed.

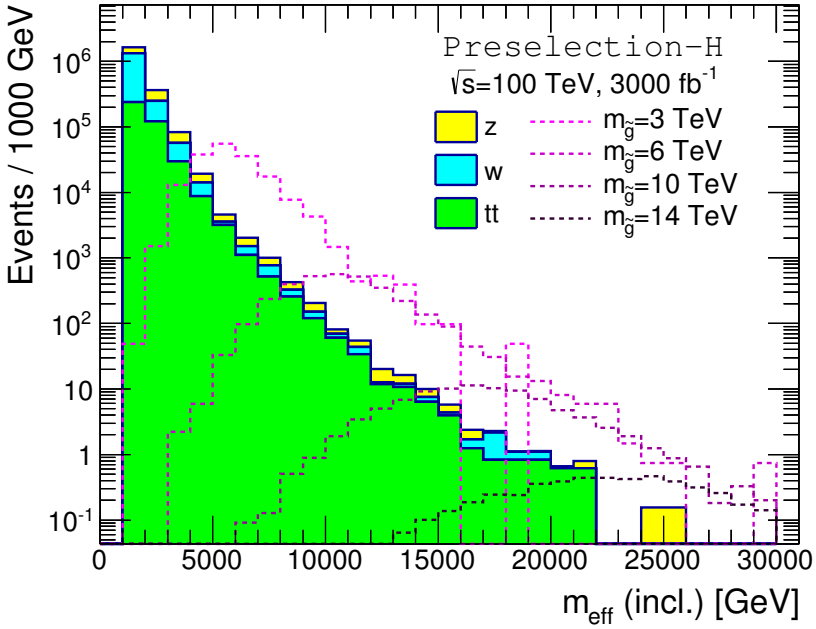

Figure 5.7: Same as Fig. 5.5 except `preselection-H` is imposed.

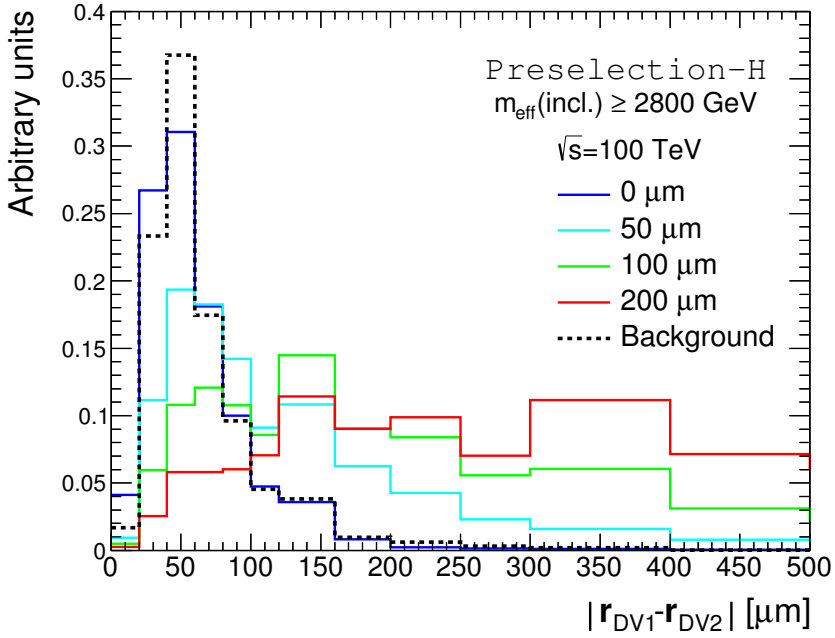

Figure 5.8: $|\boldsymbol{r}_{\mathrm{DV1}} - \boldsymbol{r}_{\mathrm{DV2}}|$ distribution of signal events (solid) and the SM background events (dashed). For signal events, we assume gluinos with mass of 3 TeV and several values of $c\tau_{\tilde{g}}$. In these distributions, `preselection-H` and requirement of $m_{\mathrm{eff}}(\mathrm{incl.}) > 2800$ GeV are imposed.

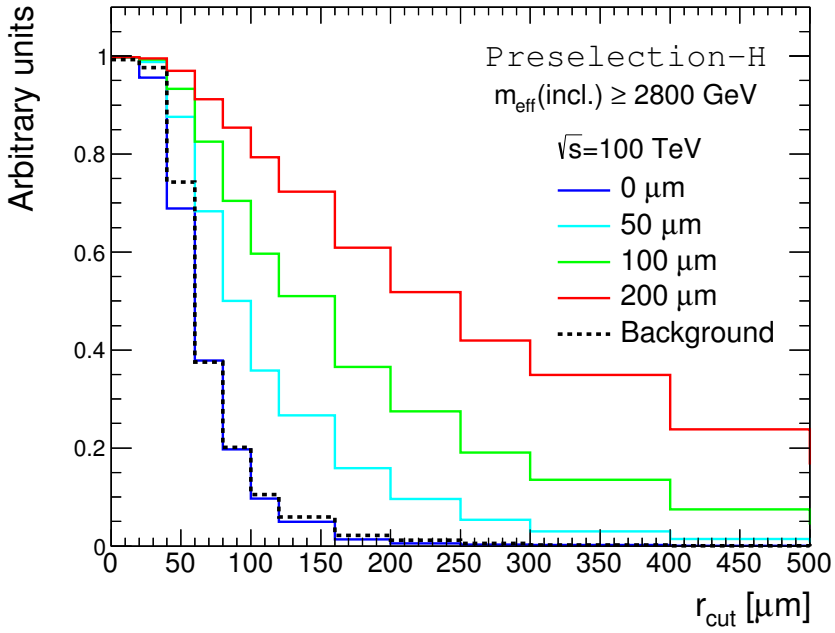

Figure 5.9: A fraction of events passing a selection cut of $|\boldsymbol{r}_{\mathrm{DV1}} - \boldsymbol{r}_{\mathrm{DV2}}| > r_{\mathrm{cut}}$. For signal events, we assume gluinos with mass of 3 TeV and several values of $c\tau_{\tilde{g}}$. In these distributions, `preselection-H` and requirement of $m_{\mathrm{eff}}(\mathrm{incl.}) > 2800$ GeV are imposed.

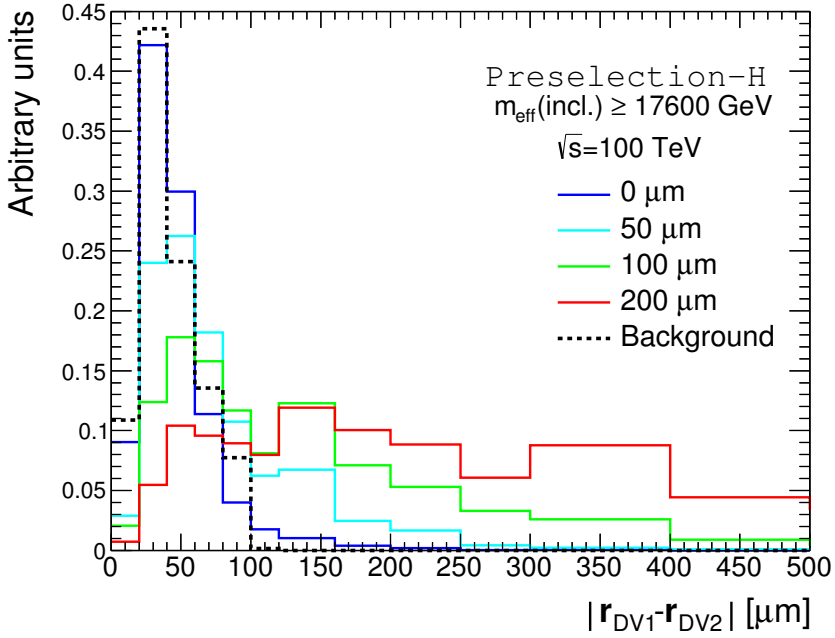

Figure 5.10: Same as Fig. 5.8 except the gluino mass of 14 TeV is assumed and m_{eff}(incl.) > 17600 GeV is imposed.

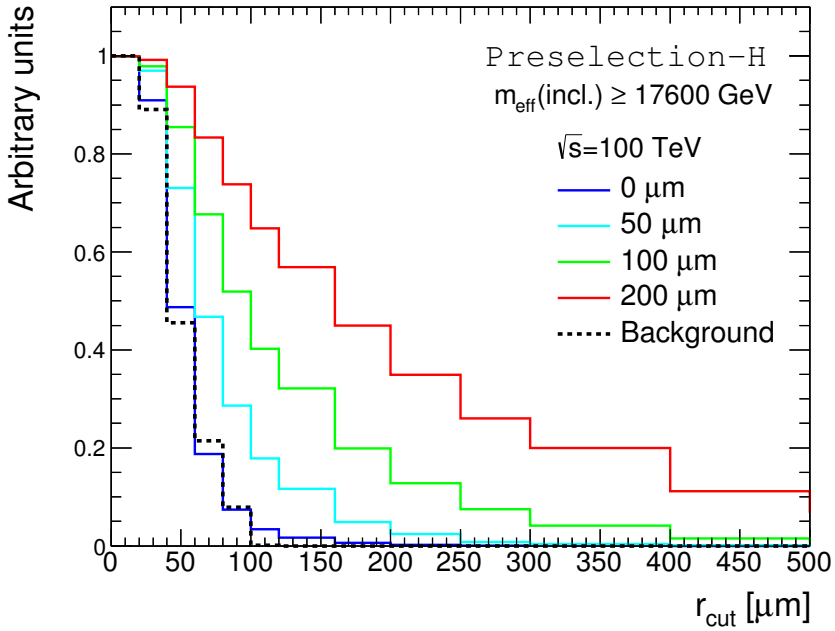

Figure 5.11: Same as Fig. 5.9 except the gluino mass of 14 TeV is assumed and m_{eff}(incl.) > 17600 GeV is imposed.

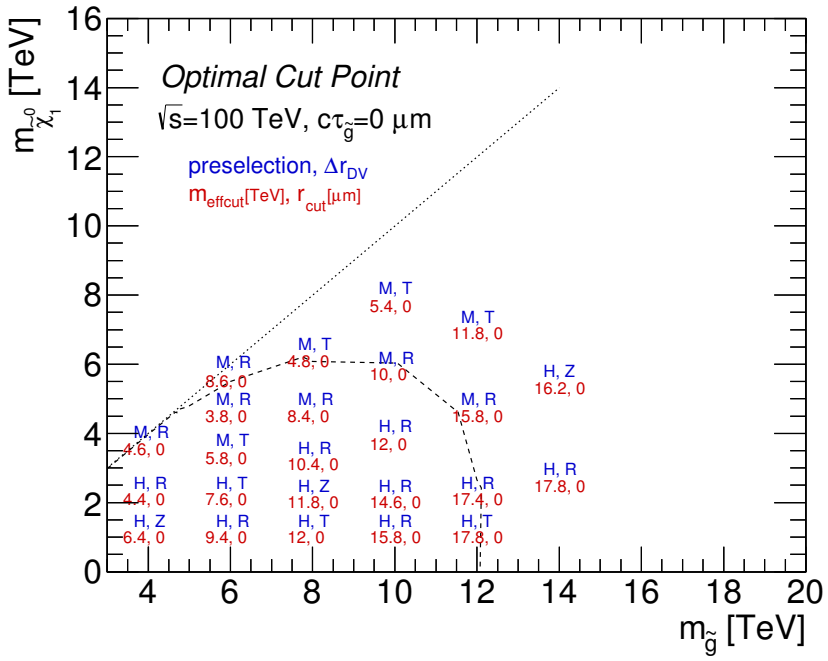

Figure 5.12: Optimal cut values ($(m_{\rm effcut})_{\rm optimal}$, $(r_{\rm cut})_{\rm optimal}$) for each sample point with $c\tau_{\tilde{g}} = 0$ μm, which maximize the expected significance Z_0 when the integrated luminosity of 3000 fb^{-1} is assumed. The preselection and the DV based observables which give the largest value of Z_0 are also presented. In the figure, R, T, and Z denote $|\boldsymbol{r}_{\rm DV1} - \boldsymbol{r}_{\rm DV2}|$, $|(\boldsymbol{r}_{\rm DV1} - \boldsymbol{r}_{\rm DV2})_{\rm T}|$, and $|(\boldsymbol{r}_{\rm DV1} - \boldsymbol{r}_{\rm DV2})_z|$, respectively. The expected 5σ discovery reaches for gluinos are also presented in a dashed line.

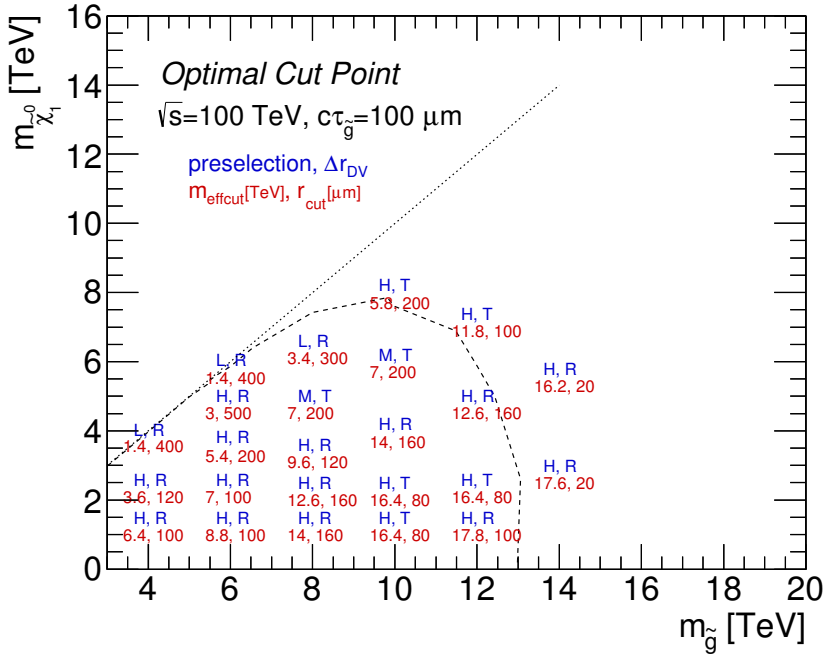

Figure 5.13: Same as Fig. 5.12 except $c\tau_{\tilde{g}} = 100$ μm.

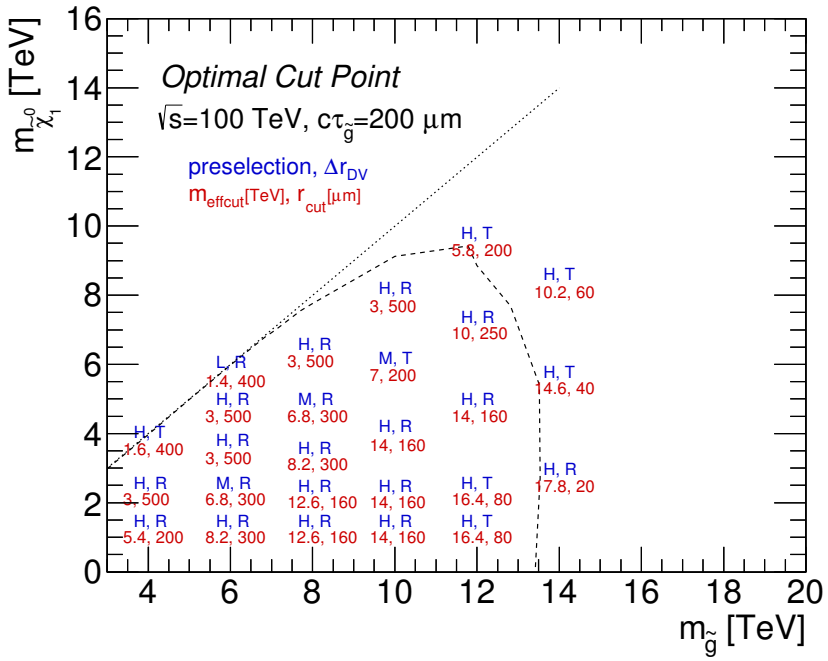

Figure 5.14: Same as Fig. 5.12 except $c\tau_{\tilde{g}} = 200$ μm.

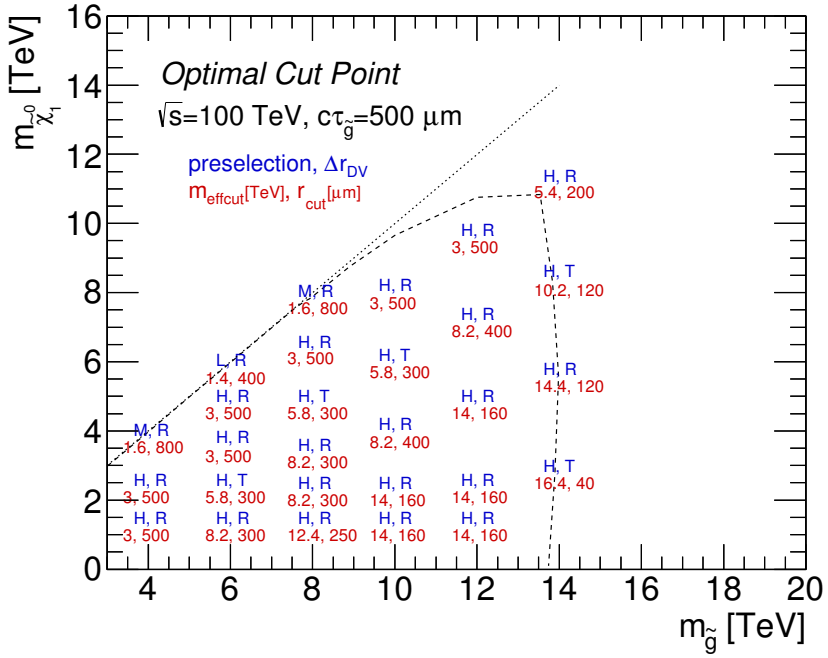

Figure 5.15: Same as Fig. 5.12 except $c\tau_{\tilde{g}} = 500$ μm.

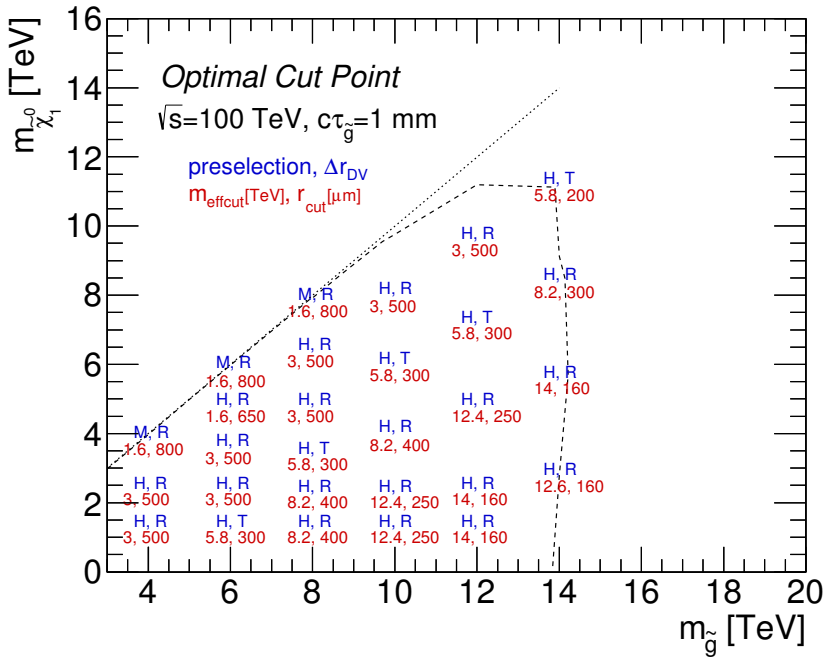

Figure 5.16: Same as Fig. 5.12 except $c\tau_{\tilde{g}} = 1$ mm.

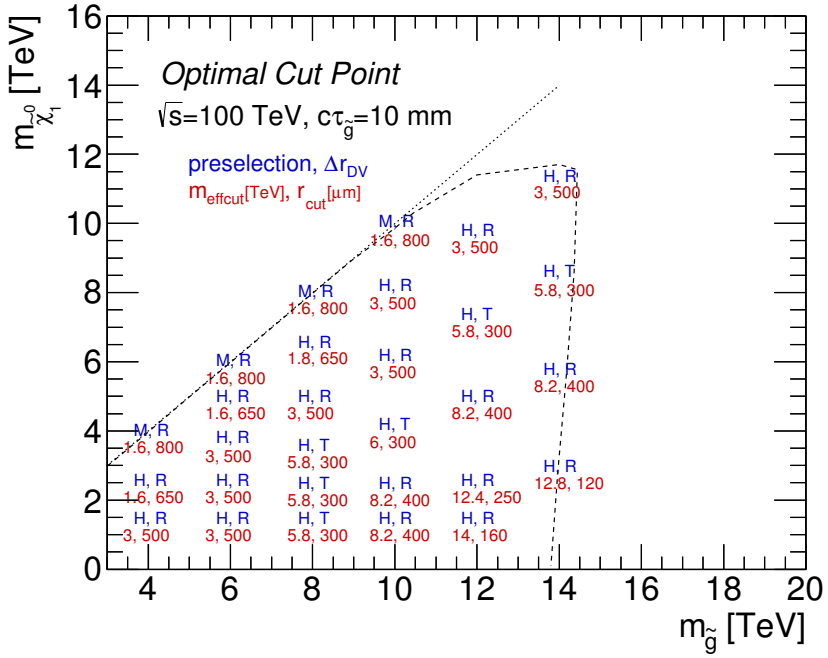

Figure 5.17: Same as Fig. 5.12 except $c\tau_{\tilde{g}} = 10$ mm.

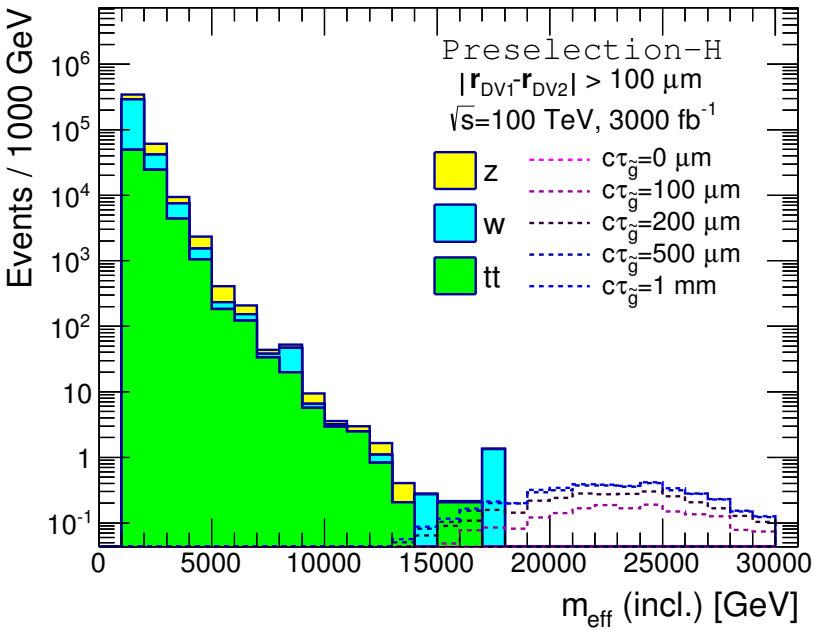

Figure 5.18: Distribution of m_{eff}(incl.) after imposing `preselection-H`, the vetos presented in Table 5.5, and $\left|\boldsymbol{r}_{\text{DV1}} - \boldsymbol{r}_{\text{DV2}}\right| > 100$ μm for the SM background processes and gluinos with various $c\tau_{\tilde{g}}$. The mass of gluinos and LSP are set to be 14 TeV and 100 GeV respectively.

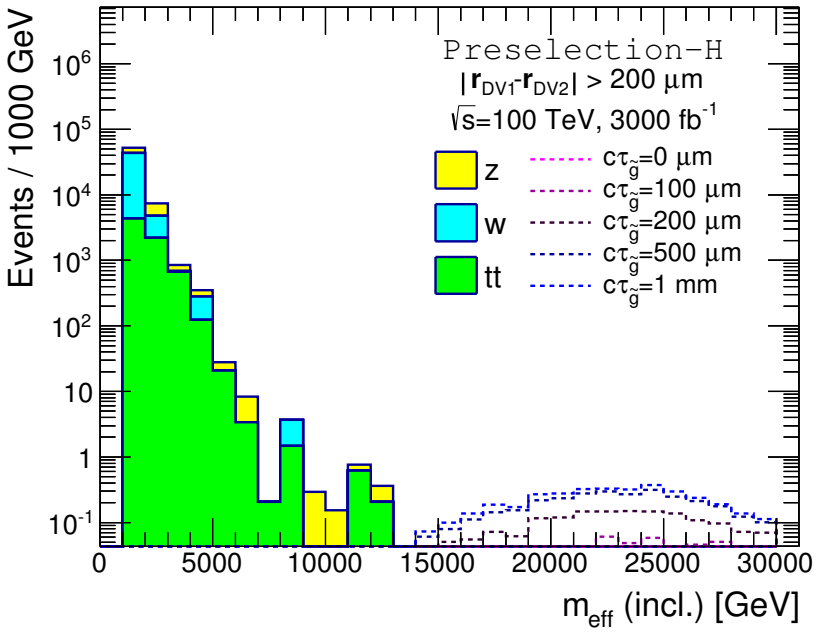

Figure 5.19: Same as Fig. 5.18 except $\left|\boldsymbol{r}_{\mathrm{DV1}} - \boldsymbol{r}_{\mathrm{DV2}}\right| > 200$ μm is required.

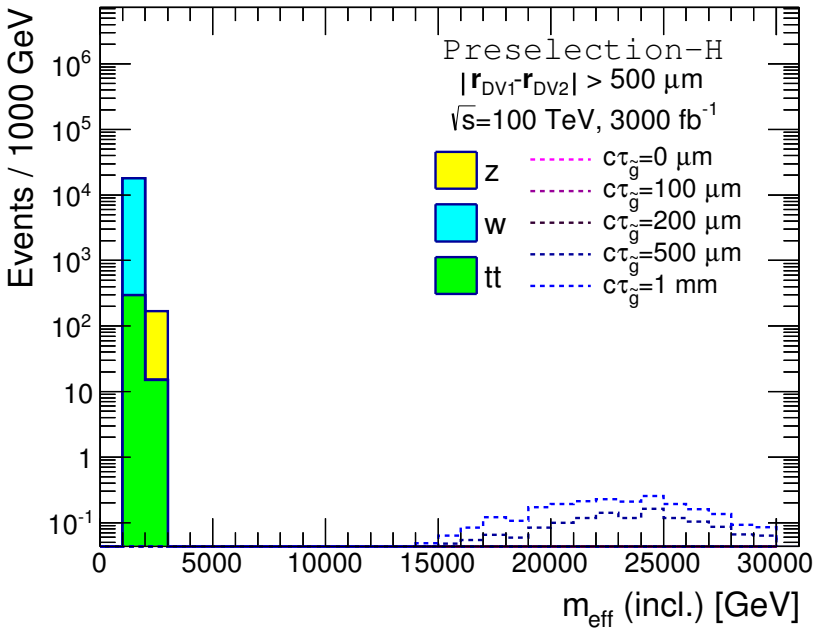

Figure 5.20: Same as Fig. 5.18 except $\left|\boldsymbol{r}_{\mathrm{DV1}} - \boldsymbol{r}_{\mathrm{DV2}}\right| > 500$ μm is required.

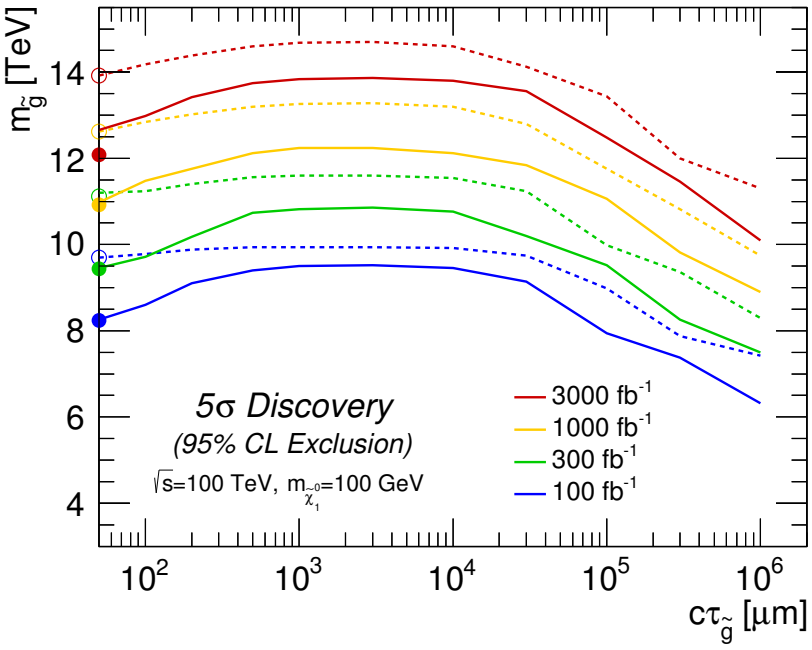

Figure 5.21: The expected 95% CL exclusion limits (dotted) and 5σ discovery reaches (solid) as functions of $c\tau_{\tilde{g}}$ for different values of integrated luminosity at a 100 TeV pp collider. The expected exclusion limit (discovery reach) for $c\tau_{\tilde{g}} = 0$ is represented by a circle (a filled circle). The mass of LSP is set to be 100 GeV.

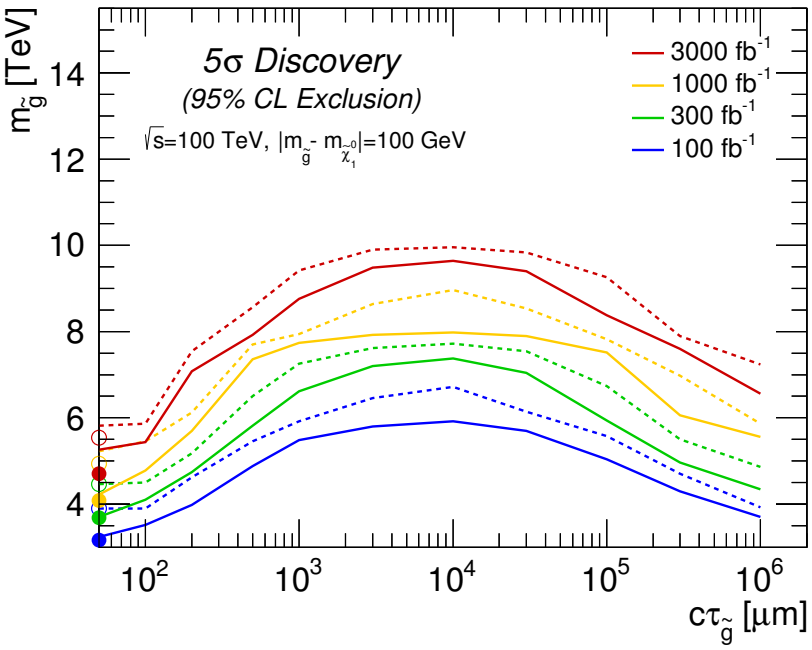

Figure 5.22: Same as Fig. 5.21 except now the mass difference between gluinos and the LSP is set to be 100 GeV.

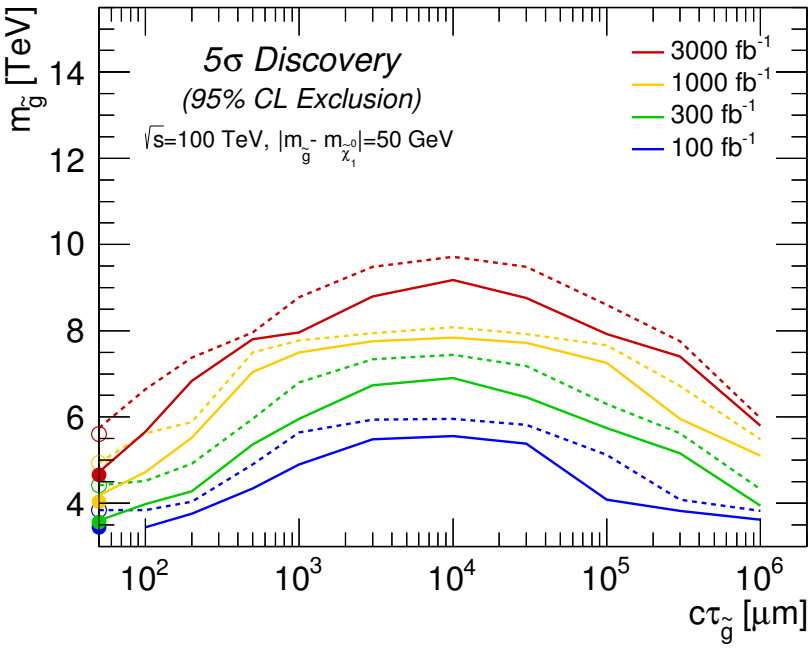

Figure 5.23: Same as Fig. 5.22 except the mass difference between gluinos and the LSP is set to be 50 GeV.

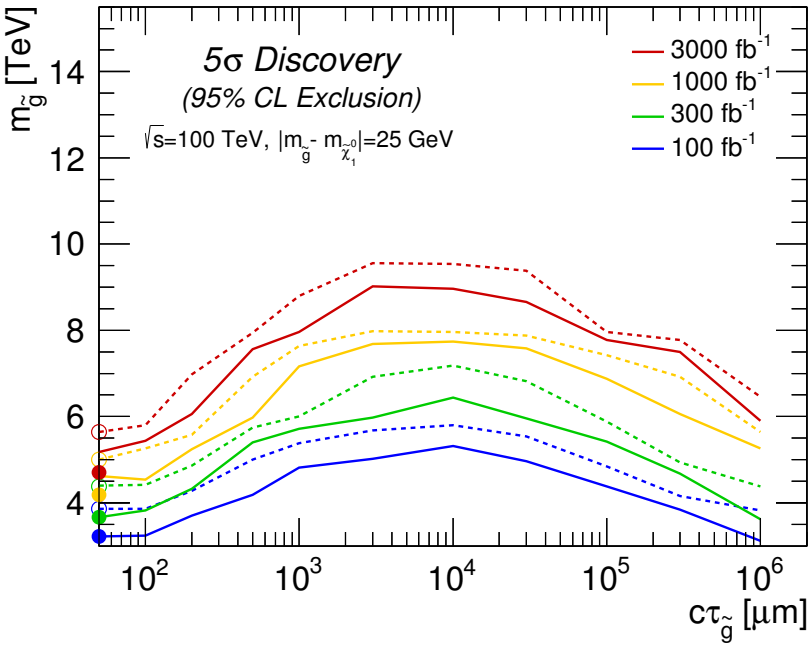

Figure 5.24: Same as Fig. 5.22 except the mass difference between gluinos and the LSP is set to be 25 GeV.

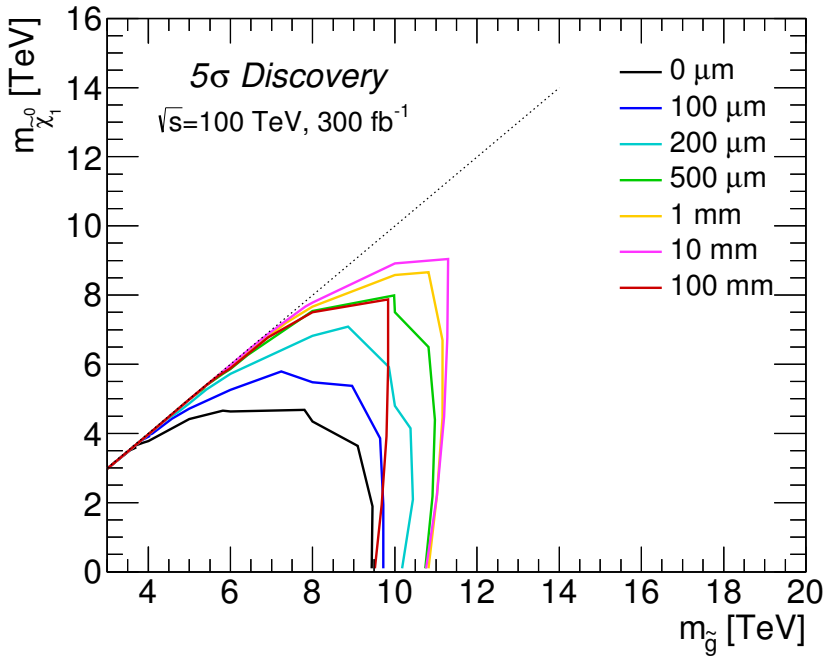

Figure 5.25: 5σ discovery reaches for gluinos with different $c\tau_{\tilde{g}}$ in terms of the gluino and the LSP masses. The integrated luminosity of $300\,\mathrm{fb}^{-1}$ is assumed.

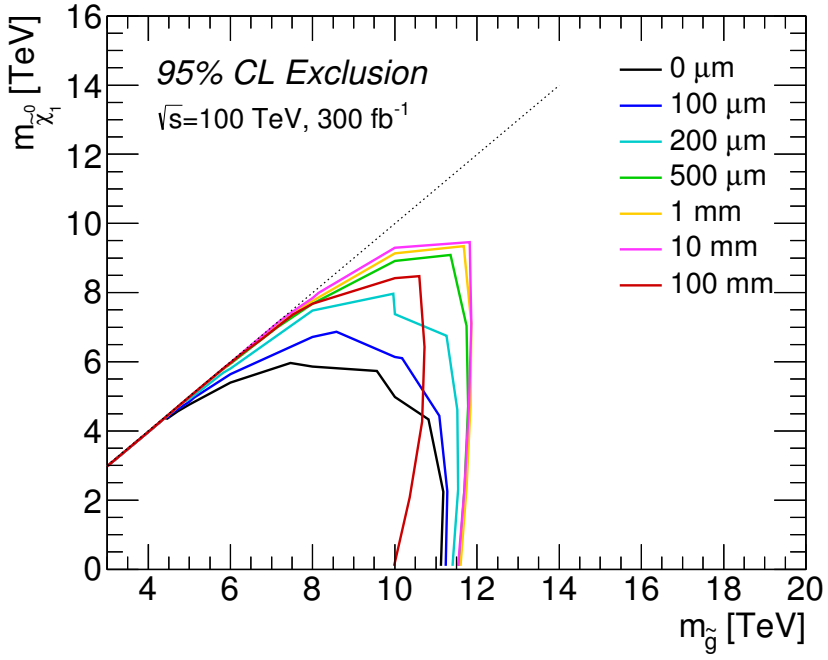

Figure 5.26: Expected 95% CL exclusion limits on gluino masses in terms of the gluino and the LSP masses. Several cases with different values of $c\tau_{\tilde{g}}$ are presented. The integrated luminosity of $300\,\mathrm{fb}^{-1}$ is assumed.

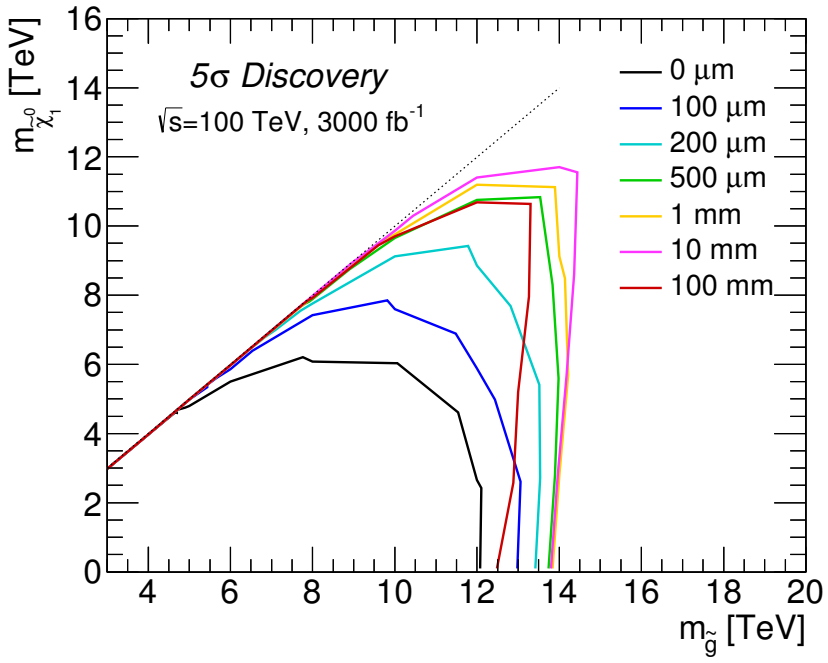

Figure 5.27: Same as Fig. 5.25 except the integrated luminosity of 3000 fb^{-1} is assumed.

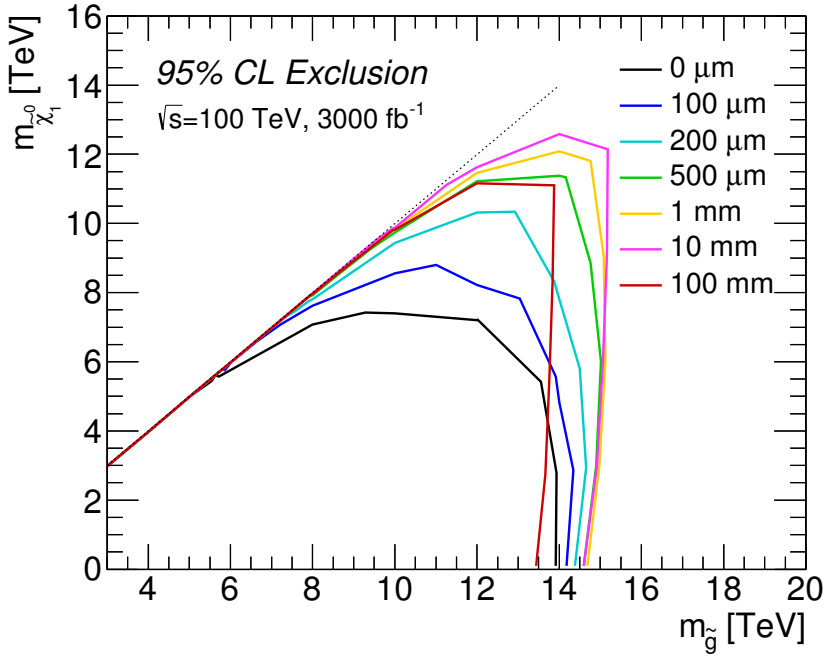

Figure 5.28: Same as Fig. 5.26 except the integrated luminosity of 3000 fb^{-1} is assumed.

Chapter 6

Conclusions and Discussion

6.1 Conclusions

In this thesis we have discussed a method of reconstructing DVs that originate from decay of metastable particles on the assumption that these metastable particles are always pair-produced and their decay products contain high-$p_{\rm T}$ jets. We consider gluinos in the SUSY models as an example, which tend to be metastable when squarks have masses much larger than the TeV scale. It is found that this method can separate out DVs if the gluino decay length is $\gtrsim 100$ μm. Then, we have seen that an event selection cut based on this DV reconstruction may be utilized to improve the potential of the gluino searches for a gluino with $c\tau_{\tilde{g}} \gtrsim 100$ μm. In particular, if $c\tau_{\tilde{g}} \sim \mathcal{O}(1\text{–}10)$ mm, then the exclusion and discovery reaches for the gluino mass can be extended by about 180 GeV and 320 GeV, respectively, with an integrated luminosity of 3000 fb^{-1} at the 13 TeV LHC when the LSP with the mass of 100 GeV is assumed. These improvement becomes more significant when gluinos and the LSP are degenerate. Furthermore, with an integrated luminosity of 3000 fb^{-1}, it is possible to measure the gluino decay length with an $\mathcal{O}(1)$ accuracy for a gluino with $c\tau_{\tilde{g}} \sim \mathcal{O}(100)$ μm and $m_{\tilde{g}} = 2.2$ TeV, which may allow us to probe the PeV-scale squarks indirectly.

We also study the prospects of searches for metastable gluinos at a future 100 TeV pp collider. Reflecting effects of the Lorentz boost, the DV reconstruction method can separate out DVs for metastable gluinos with shorter decay length. For 3 TeV gluinos, $|\boldsymbol{r}_{\rm DV1} - \boldsymbol{r}_{\rm DV2}|$ distributions significantly differ from $c\tau_{\tilde{g}} = 0$ cases if $c\tau_{\tilde{g}} \gtrsim 50$ μm. The reconstruction of DVs is found to be effective also at 100 TeV pp colliders. By imposing selection cuts based on DV variables we can extend exclusion limits and discovery reaches for $c\tau_{\tilde{g}} \gtrsim 100$ μm. If $c\tau_{\tilde{g}} \sim \mathcal{O}(1\text{–}10)$ mm, then the exclusion and discovery reaches can be extended by about 780 GeV and 1780 GeV, respectively, with an integrated luminosity of 3000 fb^{-1}, where the LSP with the mass of 100 GeV is assumed. The significant improvement for gluino-LSP degenerate cases is also seen at 100 TeV pp colliders.

6.2 Discussion

In this thesis we do not try to reconstruct the position of interaction point since we assume that no hard objects are emitted from the interaction point. However the reconstruction of the interaction point might be possible even in such case. When a hard process occurs in proton collisions, remnant of protons are also emitted from the interaction point. Although they are expected to be rather soft, we might utilize the measurement of their tracks to reconstruct the interaction point. In addition, initial state radiation (ISR) jets can also be useful. Reconstruction of the interaction point will be helpful in reducing backgrounds further.

One of the assumptions we made in this thesis is that we assume metastable particles decay into coloured particles. (For the brevity, we will mention this scenario as "hadronic DV reconstruction" in the following.) However, some models predict that new metastable particles decay into charged leptons ("leptonic DV reconstruction"). Although, we can also reconstruct DVs using tracks of charged leptons in principle, the situation might be quite different from the "hadronic DV reconstruction". As can be seen from Fig. 4.2, the resolution of vertex reconstruction depends on the number of tracks associated to the vertex. In general, the number of charged particles emitted from decay of the metastable particle is expected to be quite small if metastable particles decay into charged leptons. Therefore the resolution of vertex reconstruction is expected to deteriorate compared to the cases where metastable particles decay into coloured particles. Note that there are another difficulty in studying "leptonic DV reconstruction". In this thesis, we incorporate the effect of tracking resolution by simply shifting tracks randomly following the gaussian distribution. In spite of this simplicity, the resolution of primary vertex reconstruction is reproduced rather well as can be seen from Fig. 4.2. This is because the number of tracks used to reconstruct the position of DV is large in the "hadronic DV reconstruction' case. Since the DV reconstruction algorithm picks up the point where tracks are most densely concentrated as a position of DV, it is insensitive to the tail part of the distribution with which we model the effect of tracking resolution as long as large number of tracks are used. On the other hand, when DVs are reconstructed from small number of tracks, the resolution of DV reconstruction is also affected by the tail part of such distribution. Therefore in the "leptonic DV reconstruction" cases, more detail analysis which incorporates the effect of detector response seems to be necessary.

Another assumption which might change the results in this thesis is that metastable gluinos decay into only first-generation quarks and a neutralino. The gluino 3-body decay amplitude is proportional to inverse squared of exchanged virtual squark mass. Therefore the dominant 3-body decay mode contains quarks of the generation which contains the lightest squark. In that sense, mass spectrum of squarks may be probed by observing flavour of gluino decay products. If we assume a common scalar mass at some high scale, say GUT scale, then RGE effects on scalar masses implies stop becomes the lightest squark. In this case, dominant gluino 3-body decay becomes $\tilde{g} \to t\bar{t}\tilde{\chi}_1^0$. Since top

quarks decay into b quarks, in addition to gluino DVs, there are also secondary vertices which originate from decay of long-lived SM hadrons. With this another complexity, the performance of DV reconstruction we present might be affected in such cases.

Acknowledgments

The author wants to express his sincere gratitude to his supervisor T. Moroi, who always provides him support, and to N. Nagata, who gives him helpful comment, and to O. Jinnouchi and H. Otono, who are his collaborator of the work on which this thesis is based.

Finally, he expresses his gratitude to all the members of particle physics theory group at the University of Tokyo for their hospitality.

Appendix A

The FSMW Method

Here, we give a brief review on the FSMW method [160] used in our vertex reconstruction procedure. Our vertexing method is based on the adaptive vertex fitting algorithm [159]. In this algorithm, an initial vertex position is found using the FSMW method [160] for a pair of jets in question. This method first defines a crossing point for a pair of the two tracks chosen from each jet as the closest midpoint of these tracks. We then assign a weight to this crossing point,

$$w \equiv (d + d_{\rm min})^{-\frac{1}{2}} \ , \tag{A.1}$$

where d is the distance between the two tracks, and we set $d_{\rm min} = 10$ μm following Ref. [159]. This weight gets larger if the distance between the two tracks associated with the crossing point is smaller. Next, for a spatial coordinate, say, the x-coordinate, we consider a distribution of the crossing points and define a weighted interval for the distribution as the length of the interval divided by the sum of the weights of the points in the interval. We then find the smallest weighted interval that covers at least 40% of all the points. This process is recursively performed for the obtained smallest weighted interval until the interval contains only two points, and eventually the midpoint of the remaining two points is defined as the x-coordinate of the initial vertex position. We perform this procedure for each spatial direction.

Bibliography

[1] F. Englert and R. Brout, Phys. Rev. Lett. **13**, 321 (1964).

[2] P. W. Higgs, Phys. Lett. **12**, 132 (1964).

[3] P. W. Higgs, Phys. Rev. Lett. **13**, 508 (1964).

[4] G. S. Guralnik, C. R. Hagen, and T. W. B. Kibble, Phys. Rev. Lett. **13**, 585 (1964).

[5] P. W. Higgs, Phys. Rev. **145**, 1156 (1966).

[6] T. W. B. Kibble, Phys. Rev. **155**, 1554 (1967).

[7] S. L. Glashow, Nucl. Phys. **22**, 579 (1961).

[8] S. Weinberg, Phys. Rev. Lett. **19**, 1264 (1967).

[9] G. 't Hooft and M. J. G. Veltman, Nucl. Phys. **B44**, 189 (1972).

[10] A. Salam, Weak and electromagnetic interactions - in Elementary particle theory: relativistic groups and analyticity , N. Svartholm, ed p. 367. Almqvist & Wiksell, Proceedings of the eighth Nobel symposium. (1968).

[11] G. Aad *et al.* (ATLAS), Phys. Lett. **B716**, 1 (2012), arXiv:1207.7214 [hep-ex].

[12] S. Chatrchyan *et al.* (CMS), Phys. Lett. **B716**, 30 (2012), arXiv:1207.7235 [hep-ex].

[13] J. Wess and B. Zumino, Nucl. Phys. **B70**, 39 (1974).

[14] P. Fayet, Phys. Lett. **64B**, 159 (1976).

[15] P. Fayet, Phys. Lett. **84B**, 416 (1979).

[16] G. R. Farrar and P. Fayet, Phys. Lett. **76B**, 575 (1978).

[17] W. Altmannshofer, R. Harnik, and J. Zupan, JHEP **11**, 202 (2013), arXiv:1308.3653 [hep-ph].

[18] M. Toharia and J. D. Wells, JHEP **02**, 015 (2006), arXiv:hep-ph/0503175 [hep-ph].

[19] P. Gambino, G. F. Giudice, and P. Slavich, Nucl. Phys. **B726**, 35 (2005), arXiv:hep-ph/0506214 [hep-ph].

[20] R. Sato, S. Shirai, and K. Tobioka, JHEP **11**, 041 (2012), arXiv:1207.3608 [hep-ph].

[21] G. F. Giudice and R. Rattazzi, Phys. Rept. **322**, 419 (1999), arXiv:hep-ph/9801271 [hep-ph].

[22] P. Draper, P. Meade, M. Reece, and D. Shih, Phys. Rev. **D85**, 095007 (2012), arXiv:1112.3068 [hep-ph]; J. A. Evans and J. Shelton, JHEP **04**, 056 (2016), arXiv:1601.01326 [hep-ph]; B. C. Allanach, M. Badziak, G. Cottin, N. Desai, C. Hugonie, and R. Ziegler, Eur. Phys. J. **C76**, 482 (2016), arXiv:1606.03099 [hep-ph].

[23] R. Barbier *et al.*, Phys. Rept. **420**, 1 (2005), arXiv:hep-ph/0406039 [hep-ph].

[24] P. W. Graham, D. E. Kaplan, S. Rajendran, and P. Saraswat, JHEP **07**, 149 (2012), arXiv:1204.6038 [hep-ph]; K. Barry, P. W. Graham, and S. Rajendran, Phys. Rev. **D89**, 054003 (2014), arXiv:1310.3853 [hep-ph]; C. Csaki, E. Kuflik, and T. Volansky, Phys. Rev. Lett. **112**, 131801 (2014), arXiv:1309.5957 [hep-ph]; C. Csaki, E. Kuflik, S. Lombardo, O. Slone, and T. Volansky, JHEP **08**, 016 (2015), arXiv:1505.00784 [hep-ph].

[25] Z. Chacko, H.-S. Goh, and R. Harnik, Phys. Rev. Lett. **96**, 231802 (2006), arXiv:hep-ph/0506256 [hep-ph]; G. Burdman, Z. Chacko, H.-S. Goh, and R. Harnik, JHEP **02**, 009 (2007), arXiv:hep-ph/0609152 [hep-ph]; H. Cai, H.-C. Cheng, and J. Terning, JHEP **05**, 045 (2009), arXiv:0812.0843 [hep-ph].

[26] Z. Chacko, D. Curtin, and C. B. Verhaaren, Phys. Rev. **D94**, 011504 (2016), arXiv:1512.05782 [hep-ph].

[27] M. J. Strassler and K. M. Zurek, Phys. Lett. **B651**, 374 (2007), arXiv:hep-ph/0604261 [hep-ph].

[28] J. Barnard, P. Cox, T. Gherghetta, and A. Spray, JHEP **03**, 003 (2016), arXiv:1510.06405 [hep-ph].

[29] S. Chang and M. A. Luty, (2009), arXiv:0906.5013 [hep-ph]; R. T. Co, F. D'Eramo, L. J. Hall, and D. Pappadopulo, JCAP **1512**, 024 (2015), arXiv:1506.07532 [hep-ph].

[30] L. Basso, A. Belyaev, S. Moretti, and C. H. Shepherd-Themistocleous, Phys. Rev. **D80**, 055030 (2009), arXiv:0812.4313 [hep-ph]; J. C. Helo, M. Hirsch, and S. Kovalenko, Phys. Rev. **D89**, 073005 (2014), [Erratum: Phys. Rev.D93,no.9,099902(2016)], arXiv:1312.2900 [hep-ph]; E. Izaguirre and B. Shuve, Phys. Rev. **D91**, 093010 (2015), arXiv:1504.02470 [hep-ph]; S. Antusch, E. Cazzato, and O. Fischer, JHEP **12**, 007 (2016), arXiv:1604.02420 [hep-ph]; S. Antusch, E. Cazzato, and O. Fischer, (2016), arXiv:1612.02728 [hep-ph]; E. Accomando, L. Delle Rose, S. Moretti, E. Olaiya, and C. Shepherd-Themistocleous, (2016), arXiv:1612.05977 [hep-ph]; P. S. B. Dev, R. N. Mohapatra, and Y. Zhang, (2016), arXiv:1612.09587 [hep-ph]; A. Maiezza, M. Nemevšek, and F. Nesti, Phys. Rev. Lett. **115**, 081802 (2015), arXiv:1503.06834 [hep-ph]; M. Nemevšek, F. Nesti, and J. C. Vasquez, (2016), arXiv:1612.06840 [hep-ph].

[31] *Search for long-lived, massive particles in events with displaced vertices and missing transverse momentum in 13 TeV pp collisions with the ATLAS detector*, Tech. Rep. ATLAS-CONF-2017-026 (CERN, Geneva, 2017).

[32] M. Aaboud *et al.* (ATLAS), (2017), arXiv:1710.04901 [hep-ex].

[33] G. Aad *et al.* (ATLAS), Phys. Rev. **D88**, 112006 (2013), arXiv:1310.3675 [hep-ex].

[34] J. L. Feng, T. Moroi, L. Randall, M. Strassler, and S.-f. Su, Phys. Rev. Lett. **83**, 1731 (1999), arXiv:hep-ph/9904250 [hep-ph].

[35] M. Ibe, T. Moroi, and T. T. Yanagida, Phys. Lett. **B644**, 355 (2007), arXiv:hep-ph/0610277 [hep-ph].

[36] S. Asai, T. Moroi, K. Nishihara, and T. T. Yanagida, Phys. Lett. **B653**, 81 (2007), arXiv:0705.3086 [hep-ph]; S. Asai, T. Moroi, and T. T. Yanagida, Phys. Lett. **B664**, 185 (2008), arXiv:0802.3725 [hep-ph]; S. Asai, Y. Azuma, O. Jinnouchi, T. Moroi, S. Shirai, and T. T. Yanagida, Phys. Lett. **B672**, 339 (2009), arXiv:0807.4987 [hep-ph].

[37] N. Nagata, H. Otono, and S. Shirai, (2017), arXiv:1701.07664 [hep-ph].

[38] V. Khachatryan *et al.* (CMS), Phys. Rev. D (2016), 10.1103/PhysRevD.95.012009, [Phys. Rev.D95,012009(2017)], arXiv:1610.05133 [hep-ex].

[39] H. Ito, O. Jinnouchi, T. Moroi, N. Nagata, and H. Otono, Phys. Lett. **B771**, 568 (2017), arXiv:1702.08613 [hep-ph].

[40] S. Weinberg, Phys. Rev. **D13**, 974 (1976), [Addendum: Phys. Rev.D19,1277(1979)].

[41] E. Gildener and S. Weinberg, Phys. Rev. **D13**, 3333 (1976).

[42] E. Gildener, Phys. Rev. **D14**, 1667 (1976).

[43] L. Susskind, Phys. Rev. **D20**, 2619 (1979).

[44] G. 't Hooft, *Recent Developments in Gauge Theories. Proceedings, Nato Advanced Study Institute, Cargese, France, August 26 - September 8, 1979*, NATO Sci. Ser. B **59**, 135 (1980).

[45] K. Abe *et al.* (Super-Kamiokande), Phys. Rev. **D95**, 012004 (2017), arXiv:1610.03597 [hep-ex].

[46] S. Dimopoulos and H. Georgi, Nucl. Phys. **B193**, 150 (1981).

[47] S. Weinberg, Phys. Rev. **D26**, 287 (1982).

[48] N. Sakai and T. Yanagida, Nucl. Phys. **B197**, 533 (1982).

[49] S. Dimopoulos, S. Raby, and F. Wilczek, Phys. Lett. **112B**, 133 (1982).

[50] C. Patrignani *et al.* (Particle Data Group), Chin. Phys. **C40**, 100001 (2016).

[51] P. A. R. Ade *et al.* (Planck), Astron. Astrophys. **594**, A13 (2016), arXiv:1502.01589 [astro-ph.CO].

[52] J. R. Ellis, J. S. Hagelin, D. V. Nanopoulos, K. A. Olive, and M. Srednicki, *IN *BATAVIA 1984, PROCEEDINGS, INNER SPACE/OUTER SPACE*, 458-459., In *Srednicki, M.A. (ed.): Particle physics and cosmology* 223-246*, Nucl. Phys. **B238**, 453 (1984).

[53] L. E. Ibanez, Phys. Lett. **137B**, 160 (1984).

[54] J. S. Hagelin, G. L. Kane, and S. Raby, Nucl. Phys. **B241**, 638 (1984).

[55] T. Falk, K. A. Olive, and M. Srednicki, Phys. Lett. **B339**, 248 (1994), arXiv:hep-ph/9409270 [hep-ph].

[56] M. Beck *et al.*, Phys. Lett. **B336**, 141 (1994).

[57] E. W. Kolb and M. S. Turner, *The Early Universe* (Addison-Wesley, 1990).

[58] J. L. Feng, *Proceedings, 31st SLAC Summer Institute on Particle Physics: Cosmic Connection to Particle Physics (SSI 2003): Menlo Park, California, July 28-August 8, 2003*, eConf **C0307282**, L11 (2003), arXiv:hep-ph/0405215 [hep-ph].

[59] H. Pagels and J. R. Primack, Phys. Rev. Lett. **48**, 223 (1982).

[60] M. Dine and W. Fischler, Phys. Lett. **110B**, 227 (1982); C. R. Nappi and B. A. Ovrut, Phys. Lett. **113B**, 175 (1982); L. Alvarez-Gaume, M. Claudson, and M. B. Wise, Nucl. Phys. **B207**, 96 (1982).

[61] M. Dine and A. E. Nelson, Phys. Rev. **D48**, 1277 (1993), arXiv:hep-ph/9303230 [hep-ph]; M. Dine, A. E. Nelson, and Y. Shirman, Phys. Rev. **D51**, 1362 (1995), arXiv:hep-ph/9408384 [hep-ph]; M. Dine, A. E. Nelson, Y. Nir, and Y. Shirman, Phys. Rev. **D53**, 2658 (1996), arXiv:hep-ph/9507378 [hep-ph].

[62] J. L. Feng, A. Rajaraman, and F. Takayama, Phys. Rev. Lett. **91**, 011302 (2003), arXiv:hep-ph/0302215 [hep-ph]; J. L. Feng, A. Rajaraman, and F. Takayama, Phys. Rev. **D68**, 063504 (2003), arXiv:hep-ph/0306024 [hep-ph].

[63] L. M. Krauss, Nucl. Phys. **B227**, 556 (1983).

[64] D. V. Nanopoulos, K. A. Olive, and M. Srednicki, Phys. Lett. **127B**, 30 (1983).

[65] M. Yu. Khlopov and A. D. Linde, Phys. Lett. **138B**, 265 (1984).

[66] J. R. Ellis, J. E. Kim, and D. V. Nanopoulos, Phys. Lett. **145B**, 181 (1984).

[67] R. Juszkiewicz, J. Silk, and A. Stebbins, Phys. Lett. **158B**, 463 (1985).

[68] M. Bolz, A. Brandenburg, and W. Buchmuller, Nucl. Phys. **B606**, 518 (2001), [Erratum: Nucl. Phys.B790,336(2008)], arXiv:hep-ph/0012052 [hep-ph].

[69] M. Kawasaki, K. Kohri, and T. Moroi, Phys. Lett. **B625**, 7 (2005), arXiv:astro-ph/0402490 [astro-ph]; M. Kawasaki, K. Kohri, and T. Moroi, Phys. Rev. **D71**, 083502 (2005), arXiv:astro-ph/0408426 [astro-ph].

[70] P. Langacker and M.-x. Luo, Phys. Rev. **D44**, 817 (1991).

[71] U. Amaldi, W. de Boer, and H. Furstenau, Phys. Lett. **B260**, 447 (1991).

[72] E. Witten, Nucl. Phys. **B188**, 513 (1981).

[73] S. Dimopoulos, S. Raby, and F. Wilczek, Phys. Rev. **D24**, 1681 (1981).

[74] N. Sakai, Z. Phys. **C11**, 153 (1981).

[75] *Search for squarks and gluinos in final states with jets and missing transverse momentum using 36 fb^{-1} of $\sqrt{s} = 13$ TeV pp collision data with the ATLAS detector*, Tech. Rep. ATLAS-CONF-2017-022 (CERN, Geneva, 2017); *Search for production of supersymmetric particles in final states with missing transverse momentum and multiple b-jets at $\sqrt{s} = 13$ TeV proton-proton collisions with the ATLAS detector*, Tech. Rep. ATLAS-CONF-2017-021 (CERN, Geneva, 2017).

[76] A. M. Sirunyan *et al.* (CMS), Phys. Rev. **D96**, 032003 (2017), arXiv:1704.07781 [hep-ex]; A. M. Sirunyan *et al.* (CMS), Eur. Phys. J. **C77**, 710 (2017), arXiv:1705.04650 [hep-ex].

[77] M. Aaboud *et al.* (ATLAS), (2017), arXiv:1709.04183 [hep-ex].

[78] A. M. Sirunyan *et al.* (CMS), JHEP **10**, 005 (2017), arXiv:1707.03316 [hep-ex]; A. M. Sirunyan *et al.* (CMS), JHEP **10**, 019 (2017), arXiv:1706.04402 [hep-ex].

[79] N. Arkani-Hamed and S. Dimopoulos, JHEP **0506**, 073 (2005), arXiv:hep-th/0405159 [hep-th].

[80] G. Giudice and A. Romanino, Nucl.Phys. **B699**, 65 (2004), arXiv:hep-ph/0406088 [hep-ph].

[81] J. D. Wells, in *11th International Conference on Supersymmetry and the Unification of Fundamental Interactions (SUSY 2003) Tucson, Arizona, June 5-10, 2003* (2003) arXiv:hep-ph/0306127 [hep-ph].

[82] N. Arkani-Hamed, S. Dimopoulos, G. F. Giudice, and A. Romanino, Nucl. Phys. **B709**, 3 (2005), arXiv:hep-ph/0409232 [hep-ph].

[83] J. D. Wells, Phys. Rev. **D71**, 015013 (2005), arXiv:hep-ph/0411041 [hep-ph].

[84] M. Ibe and T. T. Yanagida, Phys. Lett. **B709**, 374 (2012), arXiv:1112.2462 [hep-ph].

[85] M. Ibe, S. Matsumoto, and T. T. Yanagida, Phys. Rev. **D85**, 095011 (2012), arXiv:1202.2253 [hep-ph].

[86] L. J. Hall and Y. Nomura, JHEP **01**, 082 (2012), arXiv:1111.4519 [hep-ph].

[87] A. Arvanitaki, N. Craig, S. Dimopoulos, and G. Villadoro, JHEP **02**, 126 (2013), arXiv:1210.0555 [hep-ph].

[88] L. J. Hall, Y. Nomura, and S. Shirai, JHEP **01**, 036 (2013), arXiv:1210.2395 [hep-ph].

[89] N. Arkani-Hamed, A. Gupta, D. E. Kaplan, N. Weiner, and T. Zorawski, (2012), arXiv:1212.6971 [hep-ph].

[90] J. L. Evans, M. Ibe, K. A. Olive, and T. T. Yanagida, Eur. Phys. J. **C73**, 2468 (2013), arXiv:1302.5346 [hep-ph].

[91] J. L. Evans, K. A. Olive, M. Ibe, and T. T. Yanagida, Eur. Phys. J. **C73**, 2611 (2013), arXiv:1305.7461 [hep-ph].

[92] *Measurement of the Higgs boson mass in the $H \to ZZ^* \to 4\ell$ and $H \to \gamma\gamma$ channels with $\sqrt{s}$=13TeV pp collisions using the ATLAS detector*, Tech. Rep. ATLAS-CONF-2017-046 (CERN, Geneva, 2017); A. M. Sirunyan *et al.* (CMS), JHEP **11**, 047 (2017), arXiv:1706.09936 [hep-ex].

[93] Y. Okada, M. Yamaguchi, and T. Yanagida, Prog. Theor. Phys. **85**, 1 (1991); Y. Okada, M. Yamaguchi, and T. Yanagida, Phys. Lett. **B262**, 54 (1991); H. E. Haber and R. Hempfling, Phys. Rev. Lett. **66**, 1815 (1991); J. R. Ellis, G. Ridolfi, and F. Zwirner, Phys. Lett. **B257**, 83 (1991).

[94] G. Degrassi, S. Di Vita, J. Elias-Miro, J. R. Espinosa, G. F. Giudice, G. Isidori, and A. Strumia, JHEP **08**, 098 (2012), arXiv:1205.6497 [hep-ph]; G. F. Giudice and A. Strumia, Nucl. Phys. **B858**, 63 (2012), arXiv:1108.6077 [hep-ph].

[95] H. E. Haber, R. Hempfling, and A. H. Hoang, Z. Phys. **C75**, 539 (1997), arXiv:hep-ph/9609331 [hep-ph].

[96] F. Gabbiani, E. Gabrielli, A. Masiero, and L. Silvestrini, Nucl. Phys. **B477**, 321 (1996), arXiv:hep-ph/9604387 [hep-ph].

[97] G. F. Giudice and A. Romanino, Phys. Lett. **B634**, 307 (2006), arXiv:hep-ph/0510197 [hep-ph].

[98] T. Moroi and M. Nagai, Phys. Lett. **B723**, 107 (2013), arXiv:1303.0668 [hep-ph].

[99] D. McKeen, M. Pospelov, and A. Ritz, Phys. Rev. **D87**, 113002 (2013), arXiv:1303.1172 [hep-ph].

[100] K. Fuyuto, J. Hisano, N. Nagata, and K. Tsumura, JHEP **12**, 010 (2013), arXiv:1308.6493 [hep-ph].

[101] R. Barbieri and L. J. Hall, Phys. Lett. **B338**, 212 (1994), arXiv:hep-ph/9408406 [hep-ph].

[102] A. M. Baldini *et al.* (MEG), Eur. Phys. J. **C76**, 434 (2016), arXiv:1605.05081 [hep-ex].

[103] J. R. Ellis, D. V. Nanopoulos, and S. Rudaz, Nucl. Phys. **B202**, 43 (1982).

[104] T. Goto and T. Nihei, Phys. Rev. **D59**, 115009 (1999), arXiv:hep-ph/9808255 [hep-ph].

[105] P. Nath, A. H. Chamseddine, and R. L. Arnowitt, Phys. Rev. **D32**, 2348 (1985).

[106] P. Nath and R. L. Arnowitt, Phys. Rev. **D38**, 1479 (1988).

[107] J. Hisano, H. Murayama, and T. Yanagida, Nucl. Phys. **B402**, 46 (1993), arXiv:hep-ph/9207279 [hep-ph].

[108] Y. Hayato *et al.* (Super-Kamiokande), Phys. Rev. Lett. **83**, 1529 (1999), arXiv:hep-ex/9904020 [hep-ex].

[109] H. Murayama and A. Pierce, Phys. Rev. **D65**, 055009 (2002), arXiv:hep-ph/0108104 [hep-ph].

[110] M. Liu and P. Nath, Phys. Rev. **D87**, 095012 (2013), arXiv:1303.7472 [hep-ph].

[111] J. Hisano, D. Kobayashi, T. Kuwahara, and N. Nagata, JHEP **07**, 038 (2013), arXiv:1304.3651 [hep-ph].

[112] M. Dine, P. Draper, and W. Shepherd, JHEP **02**, 027 (2014), arXiv:1308.0274 [hep-ph].

[113] N. Nagata and S. Shirai, JHEP **03**, 049 (2014), arXiv:1312.7854 [hep-ph].

[114] J. L. Evans, N. Nagata, and K. A. Olive, Phys. Rev. **D91**, 055027 (2015), arXiv:1502.00034 [hep-ph].

[115] T. Cohen, M. Lisanti, A. Pierce, and T. R. Slatyer, JCAP **1310**, 061 (2013), arXiv:1307.4082 [hep-ph].

[116] J. Hisano, S. Matsumoto, M. Nagai, O. Saito, and M. Senami, Phys. Lett. **B646**, 34 (2007), arXiv:hep-ph/0610249 [hep-ph].

[117] J. Fan and M. Reece, JHEP **10**, 124 (2013), arXiv:1307.4400 [hep-ph].

[118] N. Arkani-Hamed, A. Delgado, and G. F. Giudice, Nucl. Phys. **B741**, 108 (2006), arXiv:hep-ph/0601041 [hep-ph].

[119] L. Randall and R. Sundrum, Nucl. Phys. **B557**, 79 (1999), arXiv:hep-th/9810155 [hep-th].

[120] G. F. Giudice, M. A. Luty, H. Murayama, and R. Rattazzi, JHEP **12**, 027 (1998), arXiv:hep-ph/9810442 [hep-ph].

[121] T. Gherghetta, G. F. Giudice, and J. D. Wells, Nucl. Phys. **B559**, 27 (1999), arXiv:hep-ph/9904378 [hep-ph].

[122] S. Weinberg, Phys. Rev. Lett. **48**, 1303 (1982).

[123] K. Kohri, T. Moroi, and A. Yotsuyanagi, Phys. Rev. **D73**, 123511 (2006), arXiv:hep-ph/0507245 [hep-ph].

[124] M. Fukugita and T. Yanagida, Phys. Lett. **B174**, 45 (1986).

[125] W. Buchmuller, R. D. Peccei, and T. Yanagida, Ann. Rev. Nucl. Part. Sci. **55**, 311 (2005), arXiv:hep-ph/0502169 [hep-ph].

[126] W. Buchmuller, P. Di Bari, and M. Plumacher, Annals Phys. **315**, 305 (2005), arXiv:hep-ph/0401240 [hep-ph].

[127] G. F. Giudice, A. Notari, M. Raidal, A. Riotto, and A. Strumia, Nucl. Phys. **B685**, 89 (2004), arXiv:hep-ph/0310123 [hep-ph].

[128] H.-C. Cheng, B. A. Dobrescu, and K. T. Matchev, Nucl. Phys. **B543**, 47 (1999), arXiv:hep-ph/9811316 [hep-ph].

[129] M. Ibe, S. Matsumoto, and R. Sato, Phys. Lett. **B721**, 252 (2013), arXiv:1212.5989 [hep-ph].

[130] A. J. Barr, C. G. Lester, M. A. Parker, B. C. Allanach, and P. Richardson, JHEP **03**, 045 (2003), arXiv:hep-ph/0208214 [hep-ph].

[131] *Search for long-lived charginos based on a disappearing-track signature in pp collisions at* $\sqrt{s} = 13$ *TeV with the ATLAS detector*, Tech. Rep. ATLAS-CONF-2017-017 (CERN, Geneva, 2017).

[132] M. Low and L.-T. Wang, JHEP **08**, 161 (2014), arXiv:1404.0682 [hep-ph].

[133] C. Borschensky, M. Krämer, A. Kulesza, M. Mangano, S. Padhi, T. Plehn, and X. Portell, Eur. Phys. J. **C74**, 3174 (2014), arXiv:1407.5066 [hep-ph].

[134] P. M. Nadolsky, H.-L. Lai, Q.-H. Cao, J. Huston, J. Pumplin, D. Stump, W.-K. Tung, and C. P. Yuan, Phys. Rev. **D78**, 013004 (2008), arXiv:0802.0007 [hep-ph].

[135] G. Aad *et al.* (ATLAS, CMS), Phys. Rev. Lett. **114**, 191803 (2015), arXiv:1503.07589 [hep-ex].

[136] M. Aaboud *et al.* (ATLAS), (2017), arXiv:1712.02332 [hep-ex].

[137] M. Aaboud *et al.* (ATLAS), Phys. Rev. **D93**, 112015 (2016), arXiv:1604.04520 [hep-ex].

[138] M. Aaboud *et al.* (ATLAS), Phys. Lett. **B760**, 647 (2016), arXiv:1606.05129 [hep-ex].

[139] G. Aad *et al.* (ATLAS), Phys. Rev. **D88**, 112003 (2013), arXiv:1310.6584 [hep-ex].

[140] ATLAS, "*Summary Plots*," `https://twiki.cern.ch/twiki/bin/view/AtlasPublic/SupersymmetryPublicResults` (2017).

[141] A. Airapetian *et al.* (ATLAS), (1999).

[142] G. Aad *et al.* (ATLAS), JINST **3**, S08003 (2008).

[143] G. Aad *et al.* (ATLAS), (2009), arXiv:0901.0512 [hep-ex].

[144] M. S. Alam *et al.* (ATLAS), (1998).

[145] M. Aaboud *et al.* (ATLAS), Eur. Phys. J. **C77**, 466 (2017), arXiv:1703.10485 [hep-ex].

[146] *Limits on metastable gluinos from ATLAS SUSY searches at 8 TeV*, Tech. Rep. ATLAS-CONF-2014-037 (CERN, Geneva, 2014).

[147] G. Aad *et al.* (ATLAS), JHEP **09**, 176 (2014), arXiv:1405.7875 [hep-ex].

[148] G. Aad *et al.* (ATLAS), JHEP **10**, 130 (2013), [Erratum: JHEP01,109(2014)], arXiv:1308.1841 [hep-ex].

[149] *The Expected Performance of the ATLAS Inner Detector*, Tech. Rep. ATL-PHYS-PUB-2009-002. ATL-COM-PHYS-2008-105 (CERN, Geneva, 2008); *Track Reconstruction Performance of the ATLAS Inner Detector at* $\sqrt{s} = 13$ *TeV*, Tech. Rep. ATL-PHYS-PUB-2015-018 (CERN, Geneva, 2015).

[150] G. Aad *et al.* (ATLAS), Eur. Phys. J. **C75**, 407 (2015), arXiv:1506.05332 [hep-ex].

[151] G. Aad *et al.* (ATLAS), JHEP **01**, 068 (2015), arXiv:1411.6795 [hep-ex].

[152] M. Capeans, G. Darbo, K. Einsweiller, M. Elsing, T. Flick, M. Garcia-Sciveres, C. Gemme, H. Pernegger, O. Rohne, and R. Vuillermet (ATLAS Collaboration), *ATLAS Insertable B-Layer Technical Design Report*, Tech. Rep. CERN-LHCC-2010-013. ATLAS-TDR-19 (2010).

[153] *ATLAS Insertable B-Layer Technical Design Report Addendum*, Tech. Rep. CERN-LHCC-2012-009. ATLAS-TDR-19-ADD-1 (2012) addendum to CERN-LHCC-2010-013, ATLAS-TDR-019.

[154] *Vertex Reconstruction Performance of the ATLAS Detector at* $\sqrt{s} = 13$ *TeV*, Tech. Rep. ATL-PHYS-PUB-2015-026 (CERN, Geneva, 2015).

[155] *Performance of primary vertex reconstruction in proton-proton collisions at* $\sqrt{s} = 7$ *TeV in the ATLAS experiment*, Tech. Rep. ATLAS-CONF-2010-069 (CERN, Geneva, 2010); M. Aaboud *et al.* (ATLAS), (2016), arXiv:1611.10235 [physics.ins-det].

[156] S. Chatrchyan *et al.* (CMS), JINST **9**, P10009 (2014), arXiv:1405.6569 [physics.ins-det]; CMS (CMS Collaboration), *Primary vertex resolution in 2016*, Tech. Rep. CMS-DP-2016-041 (2016).

[157] ATLAS, "*Impact Parameter Resolution*," `https://atlas.web.cern.ch/Atlas/GROUPS/PHYSICS/PLOTS/IDTR-2015-007/` (2015).

[158] ATLAS, "*Impact Parameter Resolution Using 2016 MB Data*," `https://atlas.web.cern.ch/Atlas/GROUPS/PHYSICS/PLOTS/IDTR-2016-018/` (2016).

[159] R. Fruhwirth, W. Waltenberger, and P. Vanlaer, J. Phys. **G34**, N343 (2007).

[160] D. R. Bickel and R. Fruhwirth, Computational Statistics & Data Analysis **50**, 3500 (2006), arXiv:math/0505419 [math].

[161] T. Sjostrand, S. Mrenna, and P. Z. Skands, Comput. Phys. Commun. **178**, 852 (2008), arXiv:0710.3820 [hep-ph].

[162] J. Alwall, R. Frederix, S. Frixione, V. Hirschi, F. Maltoni, O. Mattelaer, H. S. Shao, T. Stelzer, P. Torrielli, and M. Zaro, JHEP **07**, 079 (2014), arXiv:1405.0301 [hep-ph].

[163] J. D. Bjorken, Phys. Rev. **D17**, 171 (1978).

[164] J. Alwall *et al.*, Eur. Phys. J. **C53**, 473 (2008), arXiv:0706.2569 [hep-ph].

[165] A. Avetisyan *et al.*, in *Proceedings, 2013 Community Summer Study on the Future of U.S. Particle Physics: Snowmass on the Mississippi (CSS2013): Minneapolis, MN, USA, July 29-August 6, 2013* (2013) arXiv:1308.1636 [hep-ex].

[166] J. de Favereau *et al.* (DELPHES 3), JHEP **1402**, 057 (2014), arXiv:1307.6346 [hep-ex].

[167] M. Cacciari, G. P. Salam, and G. Soyez, Eur. Phys. J. **C72**, 1896 (2012), arXiv:1111.6097 [hep-ph].

[168] J. D. Bjorken and S. J. Brodsky, Phys. Rev. **D1**, 1416 (1970).

[169] C. Chen, Phys. Rev. **D85**, 034007 (2012), arXiv:1112.2567 [hep-ph].

[170] G. Aad *et al.* (ATLAS), Phys. Rev. **D92**, 012010 (2015), arXiv:1504.03634 [hep-ex].

[171] ATLAS Collaboration, JINST **3**, S08003 (2008).

[172] A. Miucci, Journal of Instrumentation **9**, C02018 (2014).

[173] G. A. M. Aaboud *et al.*, Journal of Instrumentation **11**, P11020 (2016).

[174] A. L. Read, *Advanced Statistical Techniques in Particle Physics. Proceedings, Conference, Durham, UK, March 18-22, 2002*, J. Phys. **G28**, 2693 (2002); T. Junk, Nucl. Instrum. Meth. **A434**, 435 (1999), arXiv:hep-ex/9902006 [hep-ex].

[175] G. Cowan, K. Cranmer, E. Gross, and O. Vitells, Eur. Phys. J. **C71**, 1554 (2011), [Erratum: Eur. Phys. J.C73,2501(2013)], arXiv:1007.1727 [physics.data-an].

[176] *Further searches for squarks and gluinos in final states with jets and missing transverse momentum at $\sqrt{s}$ =13 TeV with the ATLAS detector*, Tech. Rep. ATLAS-CONF-2016-078 (CERN, Geneva, 2016).

[177] T. Cohen, T. Golling, M. Hance, A. Henrichs, K. Howe, J. Loyal, S. Padhi, and J. G. Wacker, JHEP **04**, 117 (2014), arXiv:1311.6480 [hep-ph].

[178] N. Arkani-Hamed, T. Han, M. Mangano, and L.-T. Wang, Phys. Rept. **652**, 1 (2016), arXiv:1511.06495 [hep-ph].

[179] R. Contino *et al.*, CERN Yellow Report , 255 (2017), arXiv:1606.09408 [hep-ph].